INVESTIGATION OF ULTRAVIOLET PHOTOIONIZATION SUSTAINED DISCHARGE FOR GAS LASERS

R.C. Lind

Hughes Research Laboratories
3011 Malibu Canyon Road
Malibu, CA 90265

September 1976

Final Technical Report
For Period 2 January 1973 Through 30 June 1976

The views and conclusions contained in this document are those of the authors and should not be interpreted as necessarily representing the official policies, either expressed or implied, of the Advanced Research Projects Agency or the U.S. Government.

Sponsored By
DEFENSE ADVANCED RESEARCH PROJECTS AGENCY
Arlington, VA 22209
DARPA Order No. 1807

Monitored By
OFFICE OF NAVAL RESEARCH
DEPARTMENT OF THE NAVY
Arlington, VA 22217

Final Technical Report
Contract N00014-73-C-0287
Reporting Period: 2 January 1973 through 30 June 1976

DARPA Order No. 1807
Program Code No. 5E20

Effective Date of Contract:	2 January 1973
Contract Expiration Date:	30 June 1976
Amount of Contract:	$546,170.00
Principal Investigator:	R.C. Lind (213) 456-6411
Scientific Officer:	Director, Physics Program Physical Sciences Division Office of Naval Research Department of the Navy 800 North Quincy Street Arlington, VA 22217

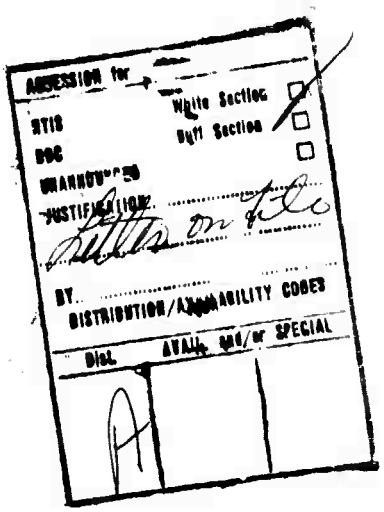

This research was supported by the Defense Advanced Research Projects Agency of the Department of Defense and was monitored by ONR under Contract N00014-73-C-0287.

UNCLASSIFIED

SECURITY CLASSIFICATION OF THIS PAGE (When Data Entered)

REPORT DOCUMENTATION PAGE	READ INSTRUCTIONS BEFORE COMPLETING FORM
1. REPORT NUMBER	2. GOVT ACCESSION NO. 3. RECIPIENT'S CATALOG NUMBER
4. TITLE (and Subtitle) INVESTIGATION OF ULTRAVIOLET PHOTOIONIZATION SUSTAINED DISCHARGE FOR GAS LASERS.	5. TYPE OF REPORT & PERIOD COVERED Final Technical Report. 2 Jan 1973 - 30 June 1976
	6. PERFORMING ORG. REPORT NUMBER
7. AUTHOR(s) R. C. Lind	8. CONTRACT OR GRANT NUMBER(s) N00014-73-C-0287, DARPA Order-1807
9. PERFORMING ORGANIZATION NAME AND ADDRESS Hughes Research Laboratories 3011 Malibu Canyon Road Malibu, California 90265	10. PROGRAM ELEMENT, PROJECT, TASK AREA & WORK UNIT NUMBERS DARPA Order No. 1807 Program Code No. 5E20
11. CONTROLLING OFFICE NAME AND ADDRESS Defense Advanced Research Projects Agency 1400 Wilson Boulevard Arlington, VA 22209	12. REPORT DATE Sept 1976 13. NUMBER OF PAGES 137
14. MONITORING AGENCY NAME & ADDRESS (if different from Contr. Illng Office) Office of Naval Research Department of the Navy Arlington, VA 22217	15. SECURITY CLASS. (of this report) UNCLASSIFIED 15a. DECLASSIFICATION DOWNGRADING SCHEDULE

16. DISTRIBUTION STATEMENT (of this Report)

DISTRIBUTION STATEMENT A
Approved for public release; Distribution Unlimited

17. DISTRIBUTION STATEMENT (of the abstract entered in Block 20, if different from Report)

18. SUPPLEMENTARY NOTES

19. KEY WORDS (Continue on reverse side if necessary and identify by block number)

CO_2 Laser
Discharge
Ultraviolet Radiation
Photoionization
Seed Gas

20. ABSTRACT (Continue on reverse side if necessary and identify by block number)

The primary objectives of this program were to establish whether a CO_2 laser plasma, suitable for high power energy extraction, could be generated by the UV sustained technique, and to determine the scalability limits of the technique. These objectives were met and laser pulses with energies greater than 400J were extracted from a UV-sustained CO_2 laser. A scaling model was developed which established that multikioljoule

DD FORM 1 JAN 73 1473 EDITION OF 1 NOV 65 IS OBSOLETE

UNCLASSIFIED

SECURITY CLASSIFICATION OF THIS PAGE (When Data Entered)

172 600

(Block 20, Continued)

outputs at efficiencies of >20% are possible if improvements in UV source brightness can be achieved.

The dynamics of the plasma generation in the UV sustained mode are similar to those of the electron beam controlled discharge; the voltage applied to the main discharge electrodes can be reduced below that required for a self-sustained avalanche mode. The principal advantage realized in this approach is complete control of the main discharge by the UV source at all times during operation. The attractive feature of UV-sustained as opposed to e-beam sustained operation is the simplicity of construction. Specifically, a foil is not required and the high voltages needed to give efficient electron penetration of the foil are not necessary.

The principal accomplishments of the program are as follows:

a. Understanding of the basic processes responsible for the plasma conditioning

b. Construction and testing of small, medium, and large scale devices to establish the operating and scalability parameters for the UV sustained technique.

c. Development of a scaling model.

Some specific results are:

- Energy extraction >400 J in an 8 x 20 x 100 cm^3 discharge volume in a 20 μsec pulse with ~12% overall efficiency using an unstable resonator
- Media quality better than λ/30 at 10.6 μm
- Small signal gain uniformity of 5% in electrode gap dimension and 25% in discharge width dimension
- Gain magnitude of ~0.85% cm typical
- Mean free path for UV photons of 8 cm typical.

Based on the results achieved on this program, it is believed that using present UV sources the UV sustained plasma conditioning technique is a viable alternative to e-beam sustained system for medium power applications. Furthermore, with improvements in UV source technology the UV sustained approach will be competitive for multikilojoule high power applications. In both cases the simplicity of the UV sustained approach is a significant advantage.

TABLE OF CONTENTS

Section			Page
I.	INTRODUCTION AND SUMMARY		1
II.	OVERVIEW OF THE PROGRAM		3
III.	BASIC PHOTOIONIZATION PROCESSES		7
	A.	Introduction	7
	B.	Single-Step Ionization Model	9
	C.	Two-Step Ionization Process	12
	D.	Photoabsorption in a CO_2 Laser Medium	16
	E.	Sample Calculation – NO Seeded Gas	19
	F.	Photoionization Yield Measurements	27
	G.	UV Emission Spectra	30
IV.	SMALL AND MEDIUM SCALE DEVICE MEASUREMENTS		35
	A.	Input Energy and Mean Free Path Determination	35
	B.	Small Signal Gain and Power Extraction – Medium Scale Device	42
V.	LARGE SCALE DEVICE		55
	A.	Device Configuration	55
	B.	Electrical Characteristics	60
	C.	Arc Sensor Circuit	66
VI.	LARGE SCALE DEVICE EXPERIMENTS		75
	A.	Input Energy Density	75
	B.	Small Signal Gain	77
	C.	Energy Extraction Results – Stable Cavity	83

TABLE OF CONTENTS (Continued)

Section			Page
	D.	Energy Extraction Results — Unstable Resonator	92
	E.	Medium Quality Studies	98
VII.		ULTRAVIOLET SUSTAINED LASER SCALABILITY	107
	A.	Scaling Model	107
	B.	Implications for Scaled UV Sustained Laser	119
VIII.		PRELIMINARY ULTRAVIOLET SOURCE STUDIES	123
	A.	Electron Density	123
	B.	Ultraviolet Source Circuit Discussion	124
	C.	Experimental Results	128
	D.	Spectral Match Considerations	129
		REFERENCES	131
APPENDIX A:		SCALING MODEL	133

LIST OF ILLUSTRATIONS

FIGURE		PAGE
III-1	Configuration used for photoionization analysis	10
III-2	Two-step photoionization processes in a seeded gas	13
III-3	Photo absorption cross section of CO_2	17
III-4	Absorption spectrum of carbon dioxide	18
III-5	Energy diagram of nitric oxide, NO	21
III-6	The absorption spectrum of nitric oxide, NO	22
III-7	Absorption spectrum of nitric oxide, NO	23
III-8	Simplified emission model used for analysis	26
III-9	Summary of photoionization in NO seeded CO_2 mixture	28
III-10	Photoionization yield test chamber	29
III-11	Relative photoionization contribution from various wavelength regions for tri-n-propylamine	29
III-12	Relative emission spectra of a He spark discharge for three current levels	31
III-13	Relative emission spectra of N_2 and He at 300 A	31
III-14	Relative emission spectra of two $CO_2/N_2/$ He laser mixtures at 300 A	33
III-15	Sustainer energy measurements obtained using different emission gases	33

FIGURE		PAGE
IV-1	Experimental UV sustained discharge device	36
IV-2	Calculated electron number density	37
IV-3	Sustainer energy as a function of UV current	39
IV-4	Maximum input sustainer energy in J/l-atm as a function of UV current in amps	40
IV-5	Ultraviolet photon mean free path through CO_2 at 0.02 atm	41
IV-6	Cascaded arc discharge system	43
IV-7	Sustainer current and cascaded arc discharge current waveforms	45
IV-8	Small signal gain waveform at position one	46
IV-9	Continuous wave probe laser positions	47
IV-10	Small signal gain as a function of bias voltage for five positions	49
IV-11	Small signal gain as a function of position for various bias voltages	50
IV-12	Small signal gain at position five for two bias voltages	51
IV-13	Laser pulse shape	52
IV-14	Near-field burn pattern	54
IV-15	Laser output as a function of E/N	54
V-1	Device and associated equipment	56
V-2	Upper electrode	57
V-3	Ultraviolet source capacitor bank assembly	58
V-4	Ultraviolet source boards	59
V-5	End view of assembled device	61

FIGURE		PAGE
V-6	Electrical feedthrough design	62
V-7	Electrical layout	64
V-8	Operation diagram	65
V-9	Timing diagram of fault detector signals	68
V-10	Fault detector block diagram	69
V-11	Arc sensor circuit	73
VI-1	Input energy density as a function of sustainer voltage	76
VI-2	Continuous wave probe laser positions	78
VI-3	Small signal gain as a function of sustainer voltage	78
VI-4	Small signal gain waveforms	79
VI-5	Small signal gain waveform, comparison of theory and experiment	81
VI-6	Small signal gain as a function of electrode gap spacing	82
VI-7	Small signal gain as a function of discharge width	84
VI-8	Optical arrangement for present energy extraction measurements	85
VI-9	Laser output as a function of sustainer voltage	86
VI-10	Near-field burn pattern	87
VI-11	(a) Sustainer and UV arc current waveforms	89
	(b) Laser pulse shape	89
VI-12	Laser pulse shape	90
VI-13	Output energy density as a function of sustainer voltage	91

FIGURE		PAGE
VI-14	Laser turn-on time as a function of sustainer voltage for 4 and 16% loss	93
VI-15	Optical arrangement for unstable resonator extraction measurements	94
VI-16	Output energy as a function of gap height	95
VI-17	Near-field burn pattern	96
VI-18	Output energy as a function of sustainer voltage for stable and unstable resonator	97
VI-19	Output energy as a function of E/N for unstable resonator	99
VI-20	Holographic experimental setup	100
VI-21	Reference hologram	102
VI-22	Media holograms	103
VI-23	Media hologram, edge of discharge at 30 μs	104
VI-24	Media hologram, center of discharge at 20 μs	106
VII-1	Model geometry	108
VII-2	Ultraviolet intensity as a function of position (z)	110
VII-3	Electric field and current density as a function of gap height	111
VII-4	Input energy density as a function of gap height	112
VII-5	Output energy as a function of gap height	114
VII-6	Relative UV intensity required as a function of gap height	116
VII-7	Overall efficiency as a function of gap height	117
VII-8	Output energy density as a function of output coupling	120

I. INTRODUCTION AND SUMMARY

The primary objectives of this program were to establish whether a CO_2 laser plasma, suitable for high power energy extraction, could be generated by the UV sustained technique, and to determine the scalability limits of the technique. These objectives were met and laser pulses with energies greater than 400J were extracted from a UV-sustained CO_2 laser. A scaling model was developed which established that multikilojoule outputs at efficiencies of >20% are possible if improvements in UV source brightness can be achieved.

The dynamics of the plasma generation in the UV sustained mode are similar to those of the electron beam controlled discharge; the voltage applied to the main discharge electrodes can be reduced below that required for a self-sustained avalanche mode. The principal advantage realized in this approach is complete control of the main discharge by the UV source at all times during operation. The attractive feature of UV-sustained as opposed to e-beam-sustained operation is the simplicity of construction. Specifically, a foil is not required and the high voltages needed to give efficient electron penetration of the foil are not necessary.

The principal accomplishments of the program are as follows:

a. Understanding of the basic processes responsible for the plasma conditioning

b. Construction and testing of small, medium, and large scale devices to establish the operating and scalability parameters for the UV sustained technique

c. Development of a scaling model.

Some specific results are:

- Energy extraction >400 J in an 8 x 20 x 100 cm^3 discharge volume in a 20 μsec pulse with ~12% overall efficiency using an unstable resonator

- Media quality better than $\lambda/30$ at 10.6 μm

- Small signal gain uniformity of 5% in electrode gap dimension and 25% in discharge width dimension
- Gain magnitude of ~0.85%/cm typical
- Mean free path for UV photons of 8 cm typical.

Based on the results achieved on this program, it is believed that using present UV sources the UV sustained plasma conditioning technique is a viable alternative to e-beam sustained systems for medium power applications. Furthermore, with improvements in UV source technology the UV sustained approach will be competitive for multikilojoule high power applications. In both cases the simplicity of the UV sustained approach is a significant advantage.

II. OVERVIEW OF THE PROGRAM

The research effort described here was carried out during the period from January 1973 to July 1976.

The objectives of this program were to investigate ultraviolet (UV) photoionizati plasma conditioning techniques and to demonstrate UV sustained electrical discharge atmospheric pressure CO_2 laser performance.

The crucial questions that needed to be answered through the research conducted during this program were (1) whether an electron density sufficient to sustain the discharge in a CO_2 laser mixture can be produced by a UV photoionization technique; specifically, plasma densities of greater than 10^{12} electrons/cm^3 over pulse lengths of 20 μsec or longer must be attained, and (2) what the scalability parameters were for such a technique.

The first year program to investigate these questions consisted basically of the following three tasks:

1. Determination of the emission spectrum of UV spark sources operated in CO_2 laser mixture, and other gas additives

2. Development of seeding techniques which will improve the photoionization efficiency of the laser medium

3. Evaluation of UV photoionization sustained CO_2 laser gas discharge characteristics and laser performance by means of small signal gain and laser power output measurements.

During the first reporting period[1] results were obtained on tasks one and two. The principal results, plasma densities required ($n_e = 10^{12}$ electrons/cm^3 for >20 μsec), were demonstrated, emission spectra of spark discharges were obtained, and a mixture mean-free path of 8 cm was conjectured for an appropriate mixture of CO_2, N_2, He and seed gas. Based on these results, baseline operating conditions for laser gas mixtures, seed gas concentrations, and UV intensities were established. These were then used as a guideline for laser measurements

(Task 3) reported during the second reporting period.[2] The principal results obtained during the second reporting period were the demonstration of laser output energy up to 50 J/l atm, in a 37 μsec (total) pulse length in a 2.5 x 15 x 50 cm^3 device in a completely UV sustained mode of operation.

With the successful demonstration of extraction energies .. 50 J/l atm in a long pulse, the objective of the next phase of the program was directed toward an understanding and demonstration of the scalability limits of the UV sustained scheme. This was accomplished by the testing of a large-scale (20 x 20 x 100 cm^3) discharge device.

During the third[3] and fourth[4] reporting period measurements of input loading, spatially and temporally resolved small signal gain, and power extraction using a stable cavity were performed on the large-scale device. An extraction energy of 200 J was obtained using a stable cavity in a configuration for which the electrode gap spacing was adjusted to 6 cm. Based on the measured mode volume, this represents an extraction energy density of 28 J/l atm. Numerous comparisons of the experimental results with an established CO_2 kinetic code were made. Gain measurements taken in both the discharge width and electrode gap spacing dimension indicated good uniformity and led to expectations of continued scalability.

During the fifth[5] reporting period, detailed measurements of media quality were made. In addition, preliminary power extraction data using an unstable resonator was made. An extraction energy of nearly 300 J was obtained with the 6 cm gap spacing. The media quality, inferred from holograms taken, indicated better than $\lambda/30$ at 10.6 μm for regions unaffected by UV and cathode waves and $\lambda/8$ including such waves.

In addition, during this reporting period, a scaling model for the UV-sustained laser was developed. This model used the results of the large-scale experiments as benchmarks for scaling. Using the model, we predicted the characteristics of a high average power UV-sustained laser.

The two principal results from the model were:

1. Using the present UV source configuration (those employed on the large scale device) scalability to 8 cm with energy densities of ~50 J/l can be achieved for 5-m gain path devices.

2. Improving the source brightness by approximately a a factor of two allows scalability to gap heights >20 cm with energy densities of >50 J/l and overall efficiencies of >20% for 5 m gain path.

During the last two reporting periods (including the present report) work focused on demonstrating maximum energy extraction with the large scale device and on preliminary experiments at attempting to achieve improvements in the UV source performance. At the completion of the contract an output energy of greater than 400 J has been demonstrated with an overall efficiency of nearly 12%* — results competitive with e-beam sustained devices, and consistent with the scaling model predictions (to be discussed).

The remainder of this final report is divided into six sections followed by one Appendix. In Section III, the basic photoionization processes relevant to the UV-sustained CO_2 laser are described using simplified models. Section IV discusses the small and medium scale device experiments aimed at establishing input energy loadings possible with the UV sustained scheme. Section V describes the design of the large-scale device and Section VI gives the results obtained from the device. In Section VII the scalability model for a UV-sustained laser is described. Finally, in Section VIII some preliminary results at attempts to improve the UV source performance are described. In Appendix A a description of the equations used in the scalability model described in Section VII is given. All of the major results, previously reported in references 1 through 6, are included in the following sections.

*The efficiency in this device was low because of limited gain: scaling the present device in length (along the optical axis) would increase the efficiency to ~20%.

BLANK PAGES
IN THIS
DOCUMENT
WERE NOT
FILMED

III. BASIC PHOTOIONIZATION PROCESS

A. Introduction

In this section, we discuss the basic photoionization processes involved and requirements associated with the production of UV photoionization sustained discharges in high pressure CO_2 lasers. Ultraviolet radiation from an efficient source propagates into the laser discharge volume and photoionizes a fixed number of neutral CO_2 laser gases and low ionization potential seed gas molecules in this region. The resulting ionization background of electrons serves to condition, both spatially and temporally, the main discharge plasma.

Once a uniform electron density has been established, plasma conditioning in the main discharge is maintained by the application of a voltage below that required to produce avalanche condition. The dynamics of the plasma in this mode are then similar to that of the electron-beam controlled sustainer discharge. In this configuration, the high energy electron beam is replaced by a low energy photon preionization source. The principal advantage realized in this mode of nonavalanche operation is the complete control of the main discharge by the UV source at all times during this discharge sequence.

One of the primary goals of the work has been to understand the scaling limits of the UV sustained conditioning scheme. To achieve this goal required an understanding of the basic processes responsible for the plasma conditioning in this new UV sustained discharge mode. This has been carried out during this contract. In particular, UV photoionization mechanisms, plasma discharge properties, and CO_2 laser processes have been studied. That work is discussed in this section.

First, a description of the two possible photoionization mechanisms – single-step and multi-step mechanisms is presented. A simple point source description of the UV source is used to facilitate understanding. A numerical example of single- and two-step processes in a system seeded with nitric oxide (NO) is then discussed. From

these studies we find that the key parameters for the photoionization are

- Single-step or multi-step processes
- Emission spectra of source
- Absorption spectra of gas
- Mean free path of laser gas mixture
- Wavelength range responsible for the photoionization.

Experiments were performed to establish these parameters. Two of these — photoionization yield and emission measurements are presented next. From these experiments it has been established that

- Single-step photoionization of the added seed gas is the dominant mechanism
- The mean free path is approximately 8 cm for useful laser mixtures
- Because of absorption by CO_2, the emission spectra of the source, and the ionization potential of the seed gas — 1200 to 1700 Å is the useful wavelength region
- Emission spectra using N_2 gas provides the best spectral match to the seed gas.

Having established these mechanisms the photoionization model can then be coupled with the discharge and laser processes to develop a scaling model. However, to develop a consistent scaling model requires certain experimental measurements to be used as check points for the model. Extensive measurements using small to large scale devices have been completed and are discussed in Sections IV and VI. The development and discussion of the scaling model will be presented in Section VII after a discussion of these pertinent results.

B. Single Step Ionization Model

The most elementary photon preionization laser configuration considered for analysis is shown in Figure III-1. We assume a point source of photons radiating a total spectral power $P(\nu, t)$. The actual source configuration may be synthesized by a superposition of such point source solutions. Later the solutions will also be generalized to cylindrical and planar sources.

The photon flux Φ with frequency ν that reaches position z is given by

$$\Phi(\nu, z, t) = \frac{P(\nu, t)}{4\pi h\nu} \frac{e^{-\mu(z)z}}{z^2} \tag{1}$$

where $\mu(z)$ is the photon attenuation per unit of length in the gas. The number of electrons $S_i(\nu, z, t)$ produced per second by direct single step photoionization in an elemental volume located at z is then

$$S_i(\nu, z, t) = \sigma_i(\nu)\, n_o\, \Phi(\nu, z, t) \tag{2}$$

where $\sigma_i(\nu)$ is the cross section for photoionization, and n_o is the gas density. It will also be useful to introduce the concept of a photon mean free path $\ell_p(\nu)$ through the relation

$$\frac{1}{\ell_p(\nu)} \equiv \sigma_i(\nu)\, n_o = \mu(\nu) \quad . \tag{3}$$

The total electron generation rate is given by the sum of all spectral contributions from the source

$$S_i(z, t) = \int_o^\infty S_i(\nu, z, t)\, d\nu \tag{4}$$

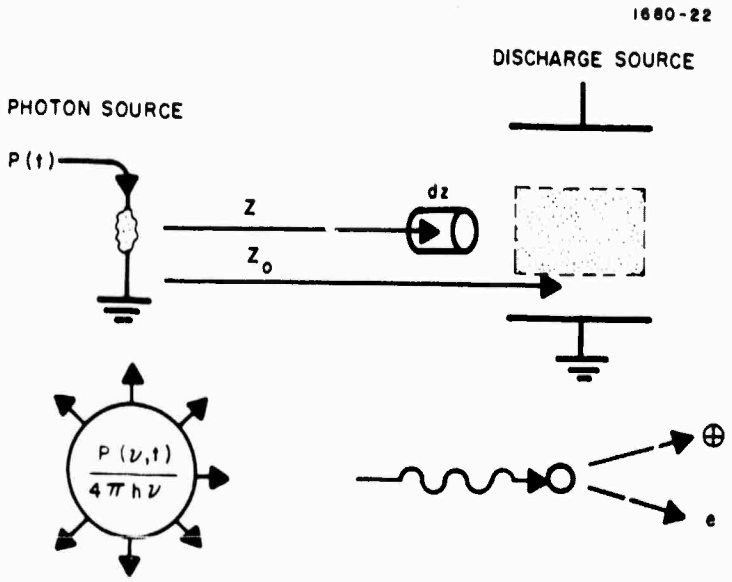

Figure III-1. Configuration used for photoinization analysis.

The quantity of prime interest is the photoelectron density $n_e(z, t)$ generated by the preionizer source. This quantity is obtained by solving

$$\frac{\partial n_e}{\partial t}(z,t) = S_i(z,t) - \alpha n_e^2 - \beta n_e + D\nabla^2 n_e \quad . \qquad (5)$$

The dominant loss mechanisms for electrons are due to recombination (αn_e^2) and attachment (βn_e). Diffusion effects ($D\nabla^2 n_e$) can be neglected at high gas pressures. Partial solutions for this differential equation are given in Table III-1.

TABLE III-1

Photoelectron Density Relationship in Recombination and Attachment Dominated Cases

	Recombination Dominated Case	Attachment Dominated Case
Electron density $\left[n_e(z,t)\right]$	$n_e(\max) \tanh \frac{t}{t_r}$	$n_e(\max)\left(1 - e^{-\frac{t}{t_r}}\right)$
Max. electron density $\left[n_e(\max)\right]$	$\left(\frac{Si}{\alpha}\right)^{1/2}$	$\left(\frac{Si}{\beta}\right)$
Rise time (t_r)	$\frac{1}{(\alpha Si)}^{1/2}$	$\left(\frac{1}{\beta}\right)$
Decay time (t_D)	$\frac{1}{\alpha n_e(z,t)} = t_\alpha$	$\left(\frac{1}{\beta}\right) = t_\beta$

$\alpha \equiv$ Recombination coefficient

$\beta \equiv$ Attachment coefficient

$Si \equiv$ Photoionization Rate

T1984

C. Two-Step Ionization Process

In the multi-step process, the first step is a photoinduced transition to an intermediate excited state in the molecule and the second or third step being a photoinduced transition from the excited state to the ionization continuum. Consider a two-state system where N_0 and N_1 are the population density in the ground and excited states respectively. Let ϕ_0 and ϕ_1 be the photon flux densities at frequencies ν_0 and ν_1 that pump the excited level and the ionization continuum as shown in Figure III-2. If the cross-sections for photoexcitation and ionization are σ_0 and σ_1, respectively, the equation governing N_1 and the photoelectron density n_e are

$$\frac{dN_1}{dt} = N_0 \sigma_0 \phi_0 - \frac{N_1}{\tau_1} - N_1 \sigma_1 \phi_1 \tag{8}$$

$$\frac{dn_e}{dt} = N_1 \sigma_1 \phi_1 - \alpha n_e^2 - \beta n_e \tag{9}$$

where τ is the lifetime of the intermediate excited states, α is the electron-ion recombination coefficient and β is the attachment coefficient. Here again like in the single step process, the terms N_1, n_e, ϕ_0 and ϕ_1 are functions of the spatial coordinates. The term $N_1 \sigma_1 \phi_1$ in eq. (8) takes into account the loss of molecules in the excited state due to photoionization.

If we assume ϕ_0 and ϕ_1 are applied at $t = 0$ and are slowly varying functions in time, the solution of eq. (8) becomes

$$N_1 = \frac{N_0 \sigma_0 \phi_0 \tau_1}{(1 + \sigma_1 \phi_1 \tau_1)} \left[1 - e^{- \frac{(1+\sigma_1 \phi_1 \tau_1)t}{\tau_1}} \right] . \tag{10}$$

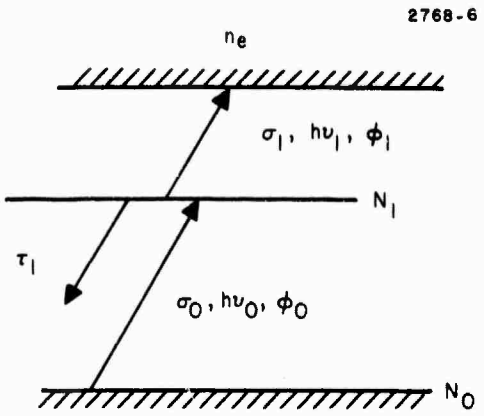

Figure III-2. Two-step photoinization processes in a seeded gas.

For $t \gg \tau_1$, the maximum steady state density of the excited level is given by

$$N_{1(max)} = \frac{N_0 \sigma_0 \phi_0 \tau_1}{(1 + \sigma_1 \phi_1 \tau_1)} \quad . \tag{11}$$

Note that as $\phi_1 \sigma_1$ becomes greater than $1/\tau_1$, the value of $N_{1(max)}$ decreases. This condition requires a relatively large UV photon flux density (ϕ_1). For a case with $\sigma_1 \simeq 10^{-17}$ cm^2 and $\tau_1 \simeq 10^{-6}$ sec, the crossover point occurs when $\phi_1 \simeq 1/\sigma_1 \tau_1 \simeq 10^{-24}$ photons/cm^2, or 1 MW/cm^2 of photons in the 2000 Å wavelength range. If the relaxation time τ_1 is larger, the crossover point would occur at a correspondingly smaller ϕ_1 value.

1. Partial Solutions for $(1/\tau_1) \ll \sigma_1 \phi_1$

In the limit where $(1/\tau_1) \ll \sigma_1 \phi_1$, the intermediate excited state simply becomes

$$N_{1(max)} = N_0 \cdot \frac{\sigma_0 \phi_0}{\sigma_1 \phi_1} \quad . \tag{12}$$

Substituting this equation into eq. (9), we obtain two solutions:

Recombination Dominated Case:

$$n_e(t) = n_e(max)_\alpha \tanh\left(\frac{t}{t_\alpha}\right) \tag{13}$$

where

$$\left.\begin{aligned} n_e(max)_\alpha &= \left(\frac{\tau_1 N_0 \sigma_0 \sigma_1 \phi_0 \phi_1}{\alpha}\right)^{1/2} \\ t_\alpha &= \frac{1}{\alpha n_e(max)_\alpha} \end{aligned}\right\} \tag{14}$$

Attachment Dominated Case:

$$n_e(t) = n_e(\max)_\beta \left[1 - \exp\left(\frac{-t}{t_\beta}\right)\right] \tag{15}$$

where

$$\left.\begin{aligned} n_e(\max)_\beta &= \frac{\tau_1 N_0 \sigma_0 \sigma_1 \phi_0 \phi_1}{\beta} \\ t_\beta &= \frac{1}{\beta} \end{aligned}\right\} \tag{16}$$

These expressions reduce to the same form as those solutions of single step ionization process discussed before.

2. Partial Solutions for $(1/\tau_1) \gg \sigma_1 \phi_1$

In the opposite limit $(1/\tau_1 \gg \sigma_1 \phi_1)$, the solution takes on a simpler form:

Recombination Dominated Case:

$$n_e(t) = n_e(\max)_\alpha \tanh\left(\frac{t}{t_\alpha}\right)$$

where

$$\left.\begin{aligned} n_e(\max)_\alpha &= \left(\frac{N_0 \sigma_0 \phi_0}{\alpha}\right)^{1/2} \\ t_\alpha &= \frac{1}{\alpha\, n_e(\max)_\alpha} \end{aligned}\right\} \tag{17}$$

and

Attachment Dominated Case:

$$\left.\begin{aligned} n_e(t) &= n_e(\max)_\beta \left[1 - \exp\left(\frac{-t}{t_\beta}\right)\right] \\ n_e(\max)_\beta &= \frac{N_0 \sigma_0 \phi_0}{\beta} \\ t_\beta &= \frac{1}{\beta} \end{aligned}\right\} \quad (18)$$

In the last two equations, the terms related to photoionization of the excited state do not appear. This results from the fact that the excited state is efficiently pumped to ionization continuum by an intense UV radiation. The net photoionization rate is simply controlled in this case by the generation rate of the intermediate state.

D. Photoabsorption in a CO_2 Laser Medium

A summary plot of the photoabsorption cross sections of the principal gas constituent (CO_2), is shown in Figure III-3 over the spectral range extending from 200 to 2000 Å. For wavelengths shorter than 900 Å, the absorption in CO_2 results mainly from the photoionization process. In this region the photon mean free path (ℓp) is extremely short. At 1 atm, $\ell p < 10^{-2}$ cm. Even if the gas number density of CO_2 is reduced by an order of magnitude to 0.1 atm (which is the approximate CO_2 concentration in a typical laser gas mixture), the mfp does not extend beyond a few millimeters.

In the wavelength range $\lambda > 900$ Å, the CO_2 absorption becomes a dominant factor. The absorption due to He is totally negligible, while the N_2 exhibits relatively low absorption spectra up to the 1000 to 1100 Å range, becoming totally negligible beyond this range. Summarized in Figure III-4 are the expanded absorption spectrum of CO_2 taken with a

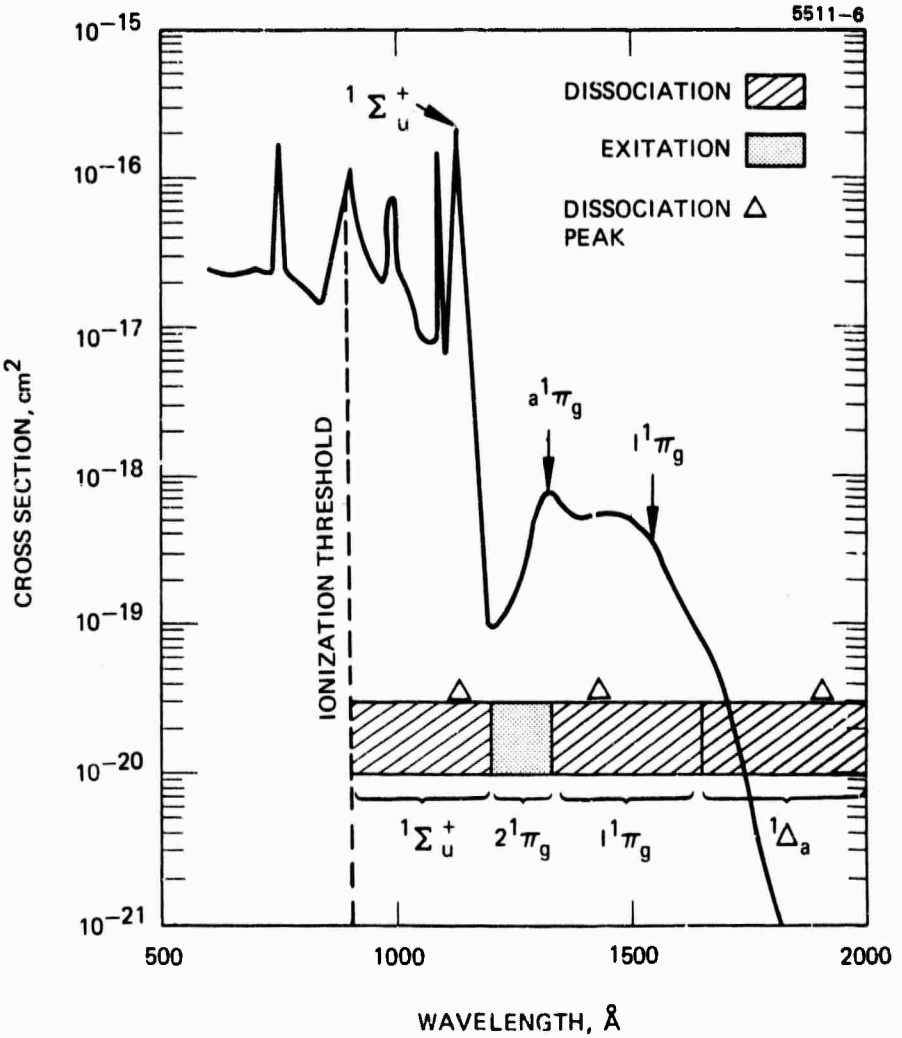

Figure III-3. Photo absorption cross section of CO_2.

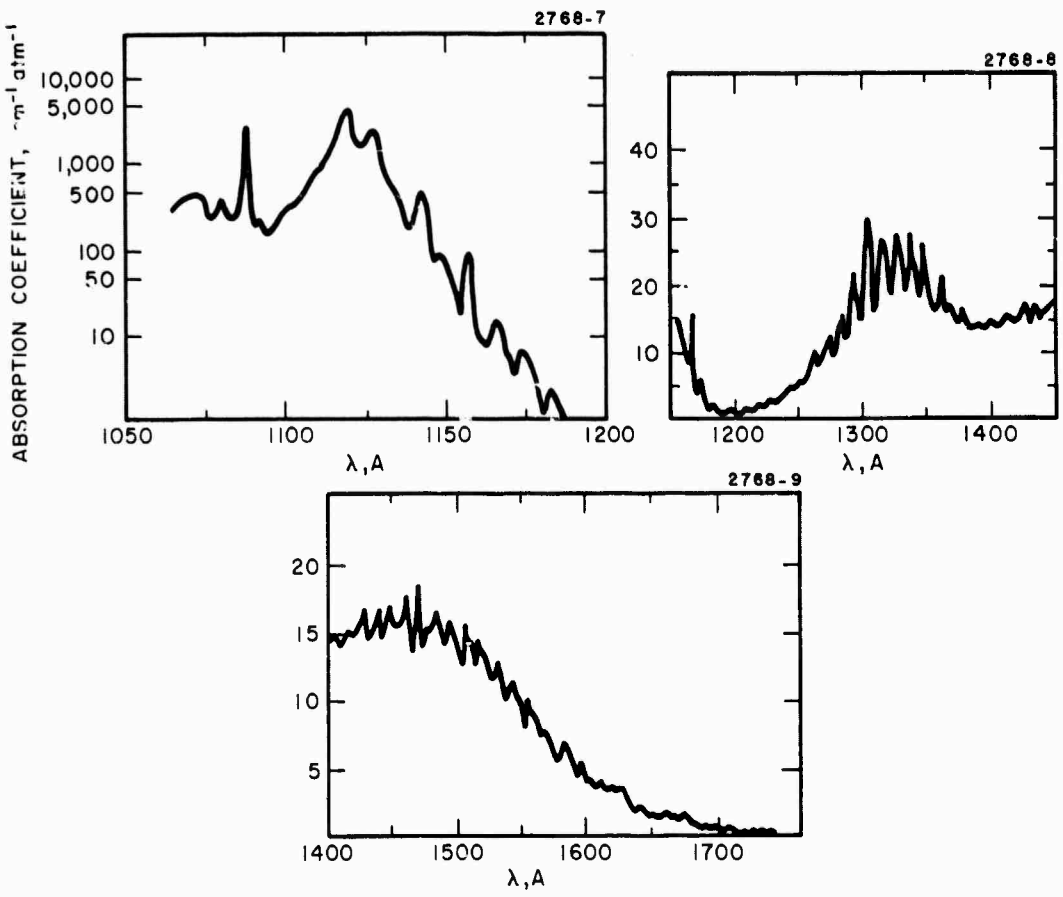

Figure III-4. Absorption spectrum of carbon dioxide. From Inn, Watanable, and Zelicoff. J. Chem. Phys., 21, 1648 (1953).

high resolution (quoted resolution of <0.2 Å) instrument. This CO_2 spectrum is characterized by a broad continuum with the transmission windows occurring at $\lambda \simeq 1200$ Å and $\lambda > 1600$ Å. The short wavelength windows at 1200 Å is relatively narrow, the 1/10 power points occurring at 1160 Å and 1275 Å. The corresponding peak mfp of this window is 1 cm at 1 atm gas pressure. This mfp scales to 20 to 30 cm for the approximate CO_2 concentration of a few percent in a typical CO_2 mixture. The window at $\lambda > 1600$ Å is much broader. The corresponding mfp is about 10 cm in a CO_2 laser mixture at 1600 Å and monotonically increasing at longer wavelengths.

In the spectral region outside these two windows, the photons cannot propagate any more than a small fraction of a cm distance from the source. The photons in these opaque regions of 1100 Å and 1300 to 1600 Å cannot be used in a sizeable CO_2 laser system with cross-sectional dimensions exceeding tens of centimeters. Furthermore, the absorption spectra in these regions result from the photodissociative transitions (as identified in Figure III-3). From the practical viewpoint, it is desirable to avoid wavelengths that give rise to photodissociative reactions for many regions: (a) dissociation of the CO_2 is undesirable since the dissociation product of atomic oxygen recombine to form molecular oxygen and produces a large increase in the electron attachment coefficient in the electrical discharge; (b) since these dissociation states do not contribute to the photoionization processes, the photon source output should be concentrated in other useful portions of the spectrum to increase the electrical to photon conversion efficiency of the source. In the discussion to follow, we shall focus upon the two ($\lambda \simeq 1200$ Å and $\lambda > 1600$ Å) windows where the mfp's of the photons larger than 10 cm are feasible.

E. Sample Calculation - NO Seeded Gas

A number of low ionization organic seed gases have been used successfully for the generation of a dense plasma ($\simeq 10^{12}$ electrons/cm^3) in a CO_2 laser mixture. A quantitative analysis of the photoionization

processes involved in many of these seeded systems has been made difficult due to the lack of pertinent data. The required lifetime information of excited states in organic molecules is simply not available. In order to circumvent this, we have sought and found NO, a low ionization gas whose physical properties are well known.

The nitric oxide molecule has been investigated extensively for the past several years, owing to its importance in the upper atmosphere study. The detailed molecular energy diagram and the measured absorption spectrum of the NO molecules are shown in Figures III-5 and III-6. The ionization threshold value for this molecule is 9.25 eV (or $\simeq$1340 Å) whereas the lowest excited state occurs in γ band ($A^2\Sigma^+ \rightarrow x^2\pi$) at 5.5 eV ($\simeq$2270 Å). The photodissociation threshold occurs at 6.48 eV ($\simeq$1930 Å). Many of the measured absorption peaks in the 1700 to 2300 Å spectral range as shown in Figure III-7 have been identified as those resulting primarily from the four (β, γ, δ and ϵ) bands. Typical mfp dimensions of these peaks at the assumed seed gas concentration are larger than 20 cm. Some of these transitions overlap with each other and thus they are not separable. The published absorption data and the radiative decay time inferred from the oscillator strength of respective transitions are summarized in Table III-2. In these we have sufficient information to compute the photoionization electron density in a seeded CO_2 laser mixture resulting from the single step and the two-step processes.

Before we discuss the computational results, a brief mention should be made of the basic equations governing multiple excitation transitions. The two-step processes resulting from a finite number of intermediate excited states can be written in the form analogous to eq. (8) and (9):

$$\frac{d(N_1)i}{dt} = (\sigma_0 N_0 \phi_0)_i - (\sigma_1 N_1 \phi_1)_i - \left(\frac{N_1}{\tau}\right)_i \quad ; \quad i \leq N \qquad (19)$$

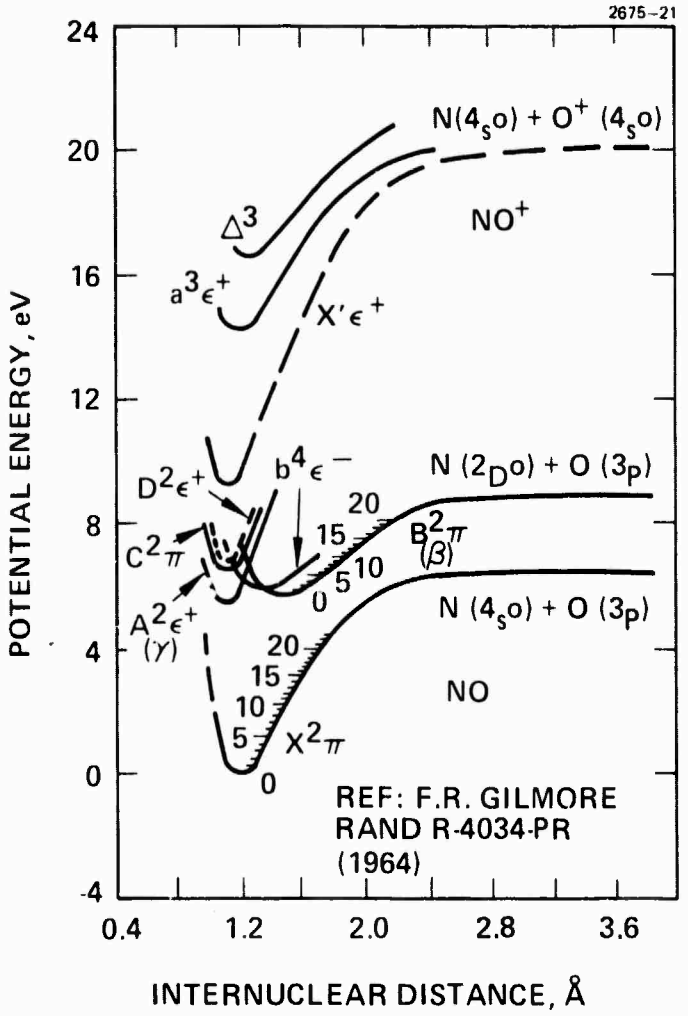

Figure III-5. Energy diagram of nitric oxide, NO.

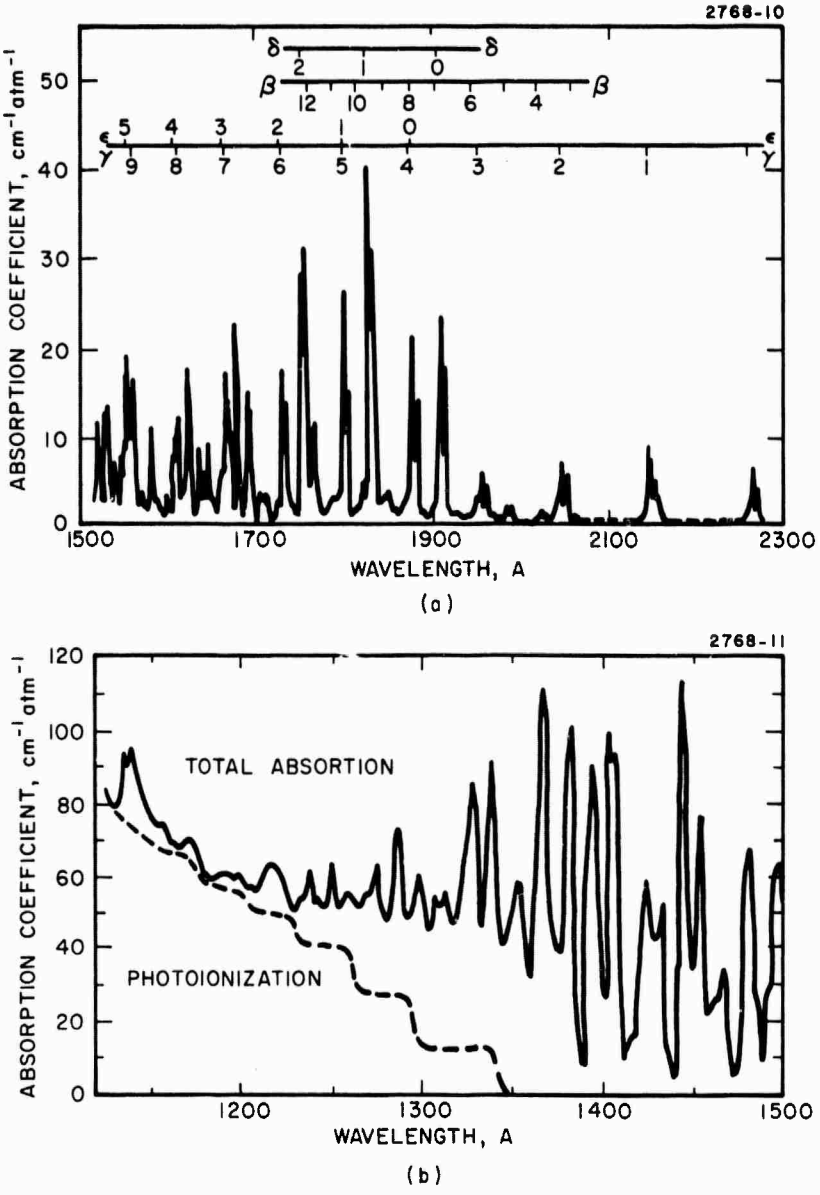

Figure III-6. The absorption spectrum of nitric oxide, NO. From K. Watanabe, J. Chem. Phys. 22, 1564 (1954).

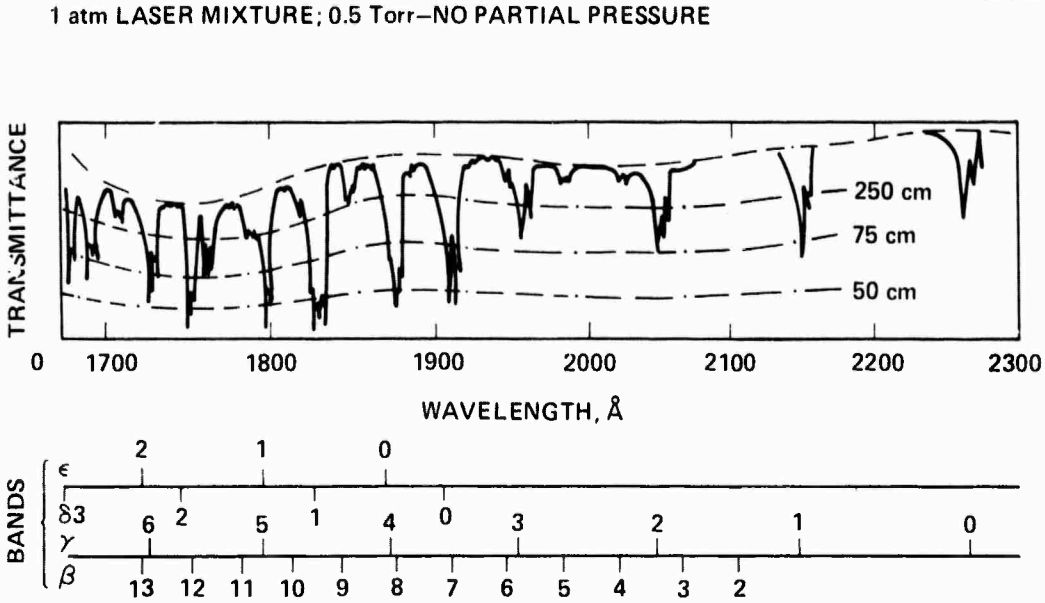

Figure III-7. Absorption spectrum of nitric oxide, NO. From F.F. Marmo, J. Opt. Soc. Am., 43, 1186 (1953).

TABLE III-2

Integrated Absorption Coefficient (K_o) and Approximate Lifetime (τ) of NO (1700 to 2300 Å)

Band (1700 to 2300 Å)	K_o* Integrated Absorption Coefficient (10^3 cm^{-2} atm^{-1})	τ* Radiative Decay Time, μsec
β(2, 0)	0.037	284
β(3, 0)	0.109	91
β(4, 0)	0.328	30
β(5, 0)	0.628	15
β(6, 0)	1.10	13
β(9, 0)	8.53	1.5
β(11, 0)	8.62	1.3
β(12, 0)	54.9	0.2
β(14, 0)	4.77	2.3
(0, 0)	9.49	1.9
(1, 0)	18.7	0.9
(2, 0)	16.0	0.9
(3, 0)	8.57	1.6
ϵ(0, 0) + (4, 0) +β (8, 0)	60.4	0.2
ϵ(1, 0) + (5, 0)	109	0.11
δ(0, 0) +β (7, 0)	59.2	0.22
δ(1, 0) +β (10, 0)	137	0.09
δ(2, 0)	65.2	0.017

*Bethke, J. Chem. Phy. 31, 663 (1959)

T1112

$$\frac{dn_e}{dt} = \sum_{i=1}^{N} (\sigma_1 N_1 \phi_1)_i - \alpha n_e^2 - \beta n_e \qquad (20)$$

where the subscript i refers to the i^{th} excited state. The finite total of N excited states is assumed. The first term appearing in the right-hand side of eq. (20) represents the combined production rate of photoelectrons through N separate excitation channels. The absorption data summarized in Table III-2 are given in terms of the integrated absorption coefficient K_{oi} which is defined through an expression

$$(\sigma_0 N_0 \phi_0)_i = \int_{\Delta\epsilon} \alpha(\epsilon)_i \frac{\Delta\phi(\epsilon)}{\Delta\epsilon} d\epsilon = p_o K_{oi} \frac{\Delta\phi(\epsilon)}{\Delta\epsilon} \qquad (21)$$

where

$\alpha(\epsilon)_i$ = absorption coefficient of i^{th} state

p_o = partial pressure of absorbing gas

$\frac{\Delta\phi(\epsilon)}{\Delta\epsilon}$ = photo flux density per unit increment of photon energy.

For the present illustration, we shall assume a simple UV incident spectrum as shown in Figure III-8. The shaded area represents the CO_2 absorption band. The long wavelength emission spectrum ($\lambda > 1600$ Å) approximates the part of flashlamp output from a high quality UV transmitting tube (i.e., suprasil). The spark UV source immersed in the CO_2 mixture basically shows the similar characteristics with a broad continuum extending from 1600 Å to at least 3000 Å. The spark source used without a window material gives rise to an additional spectrum in 1200 Å passband with its amplitude much lower than that of the long wavelength region. The reduction factor δI_0 is introduced in order to account for this difference; typically this value is found to be 0.1 to 0.3.

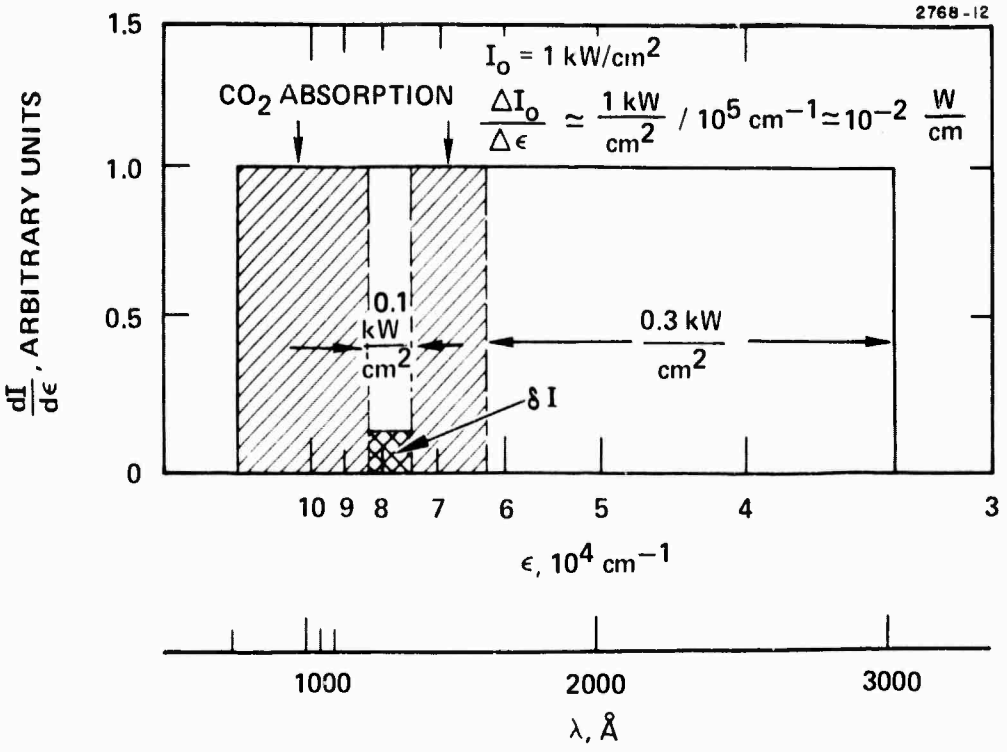

Figure III-8. Simplified emission model used for analysis.

The computed photoelectron densities (n_e) as a function of the incident UV intensity (I_0) are plotted in Figure III-9 for both the single and two step processes. The functional dependence of the attachment and recombination dominated regions as discussed in Section II-B are exhibited in this figure. At low UV intensity single step photoionization is more efficient. At the $n_e \simeq 10^{12}$ electrons/cm^3 level, two step process requires the intensity to be more than one order of magnitude larger. As the level of n_e is increased, the difference in the required UV intensities becomes smaller. At $n_e \geq 10^{13}$ electrons/cm^3, the two processes will require about the same level of excitation.

F. Photoionization Yield Measurements

Having established that dense plasmas could be achieved in seeded CO_2 mixtures (see Section IV and VI), an effort to characterize the wavelengths responsible for the observed photoionization of the added seed gases was undertaken. A small photoionization chamber in which the combined seed gas and laser mixture could be separated from the spark emission chamber (see Figure III-10) was employed. The experiment was conducted by inserting several UV-wavelength cutoff windows into the chamber and measuring the current drawn, using the Faraday cage, for the various wavelength bands obtained.

The relative photoionization yield for the wavelength bands determined by these windows was measured for Tri-n-propylamine (ionization potential of 1720 Å) added to a $CO_2/N_2/He$ mixture with the results given in Figure III-11. These results display the fact that the photoionization which yields the observed sustainer currents (see Section IV) is due to radiation with wavelengths between approximately 1200 and 1700 Å.* One then concludes that apparently single-step photoionization is the responsible mechanism for these experiments.

*The relative percent breakdown between the wavelength regions shown is subject to as much as a 20% error due to the poor cutoff characteristics of sapphire.

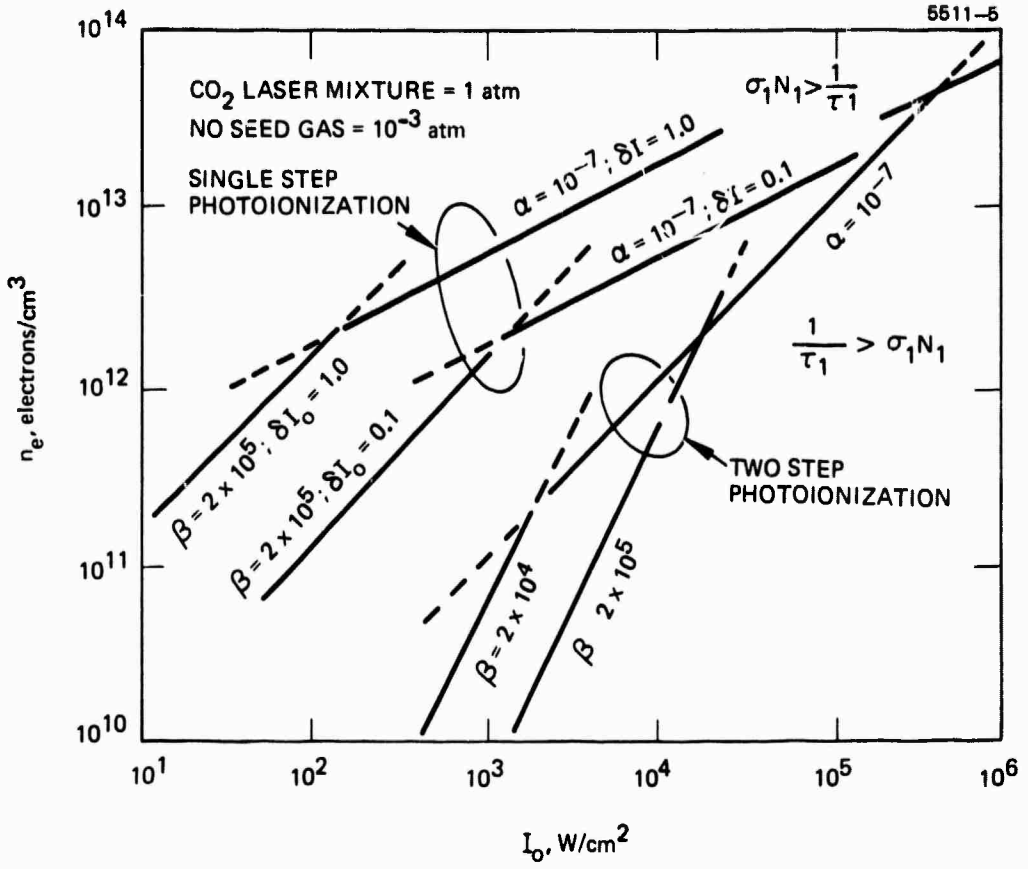

Figure III-9. Summary of photoionization in NO seeded CO_2 mixture.

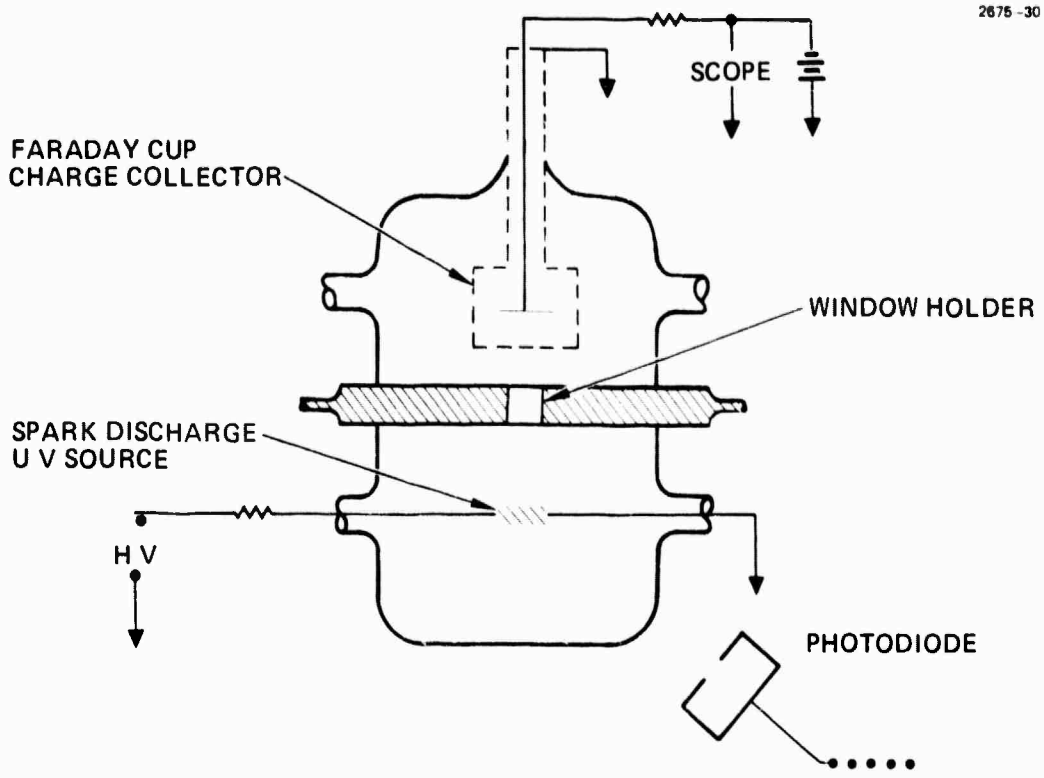

Figure III-10. Photoionization yield test chamber.

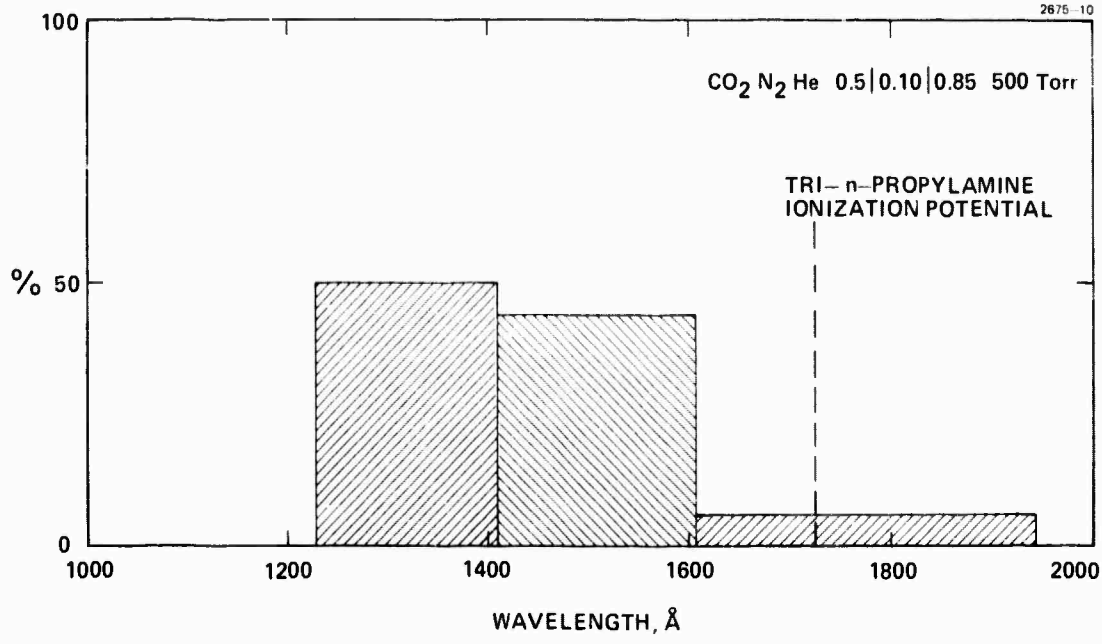

Figure III-11. Relative photoionization contribution from various wavelength regions for tri-n-propylamine.

The scalability of this single-step ionization process is determined basically by the UV photon mean free path of CO_2 and Tri-n-propylamine in the CO_2/N_2/He mixture. From absorption coefficient measurements[1] the mean free path for CO_2 at 0.02 atm and Tri-n-propylamine at 0.3 Torr in the wavelength range of interest give about an 8 cm mean free path as a realistic value that one atmosphere CO_2 lasers can achieve (see Section III).

G. UV Emission Spectra

In conjunction with absorption measurements and photoionization yield measurements a knowledge of the emission spectra of the spark sources is needed. The experimental configuration consisted of a spark source placed in close proximity to a McPherson spectrometer entrance slit.(approximately 2-3 cm). Based on the results of the previous section, which indicated that the wavelength region of interest spans the range from 1200 Å and longer, a LiF window (cutoff at 1050 Å) was used to isolate the spark source from the spectrometer.

Figure III-12 displays the effect of varying the UV current through the spark for a He discharge. Three currents of 300, 400 and 550 A are shown. (Due to experimental limitations 550 A was the peak current that could be achieved.) It is apparent that increased current leads to increased emission with no apparent change in the relative spectra.

In Figure III-13 the emission spectra of N_2 at a current level of 300 A is shown. The comparable He spectra is also given. Note that the N_2 and He spectra are similar but the N_2 intensity is substantially increased. The similarity is due to the fact that most of the lines observed in the He data arise from the small level of N_2 impurity in the He. Many of these observed lines can be attributed to atomic nitrogen spectra.

Several electrode materials were investigated with no appreciable difference in their spectra. Since the current levels are below that expected to yield metal vapor spectra, this is not unexpected.

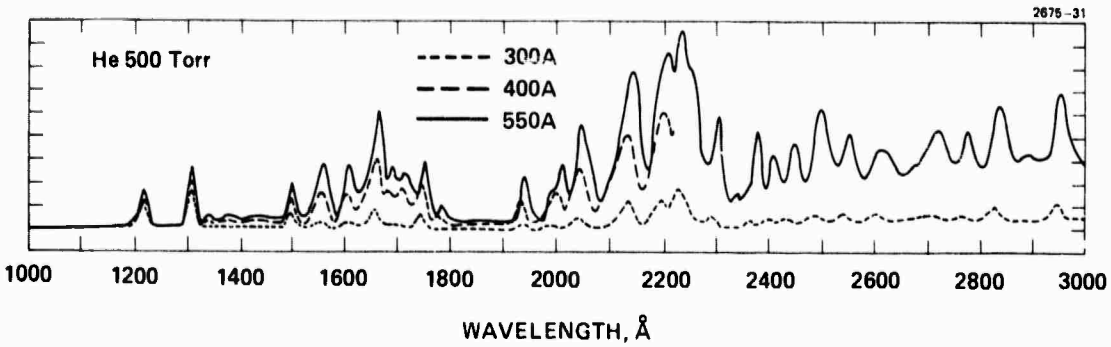

Figure III-12. Relative emission spectra of a He spark discharge for three current levels.

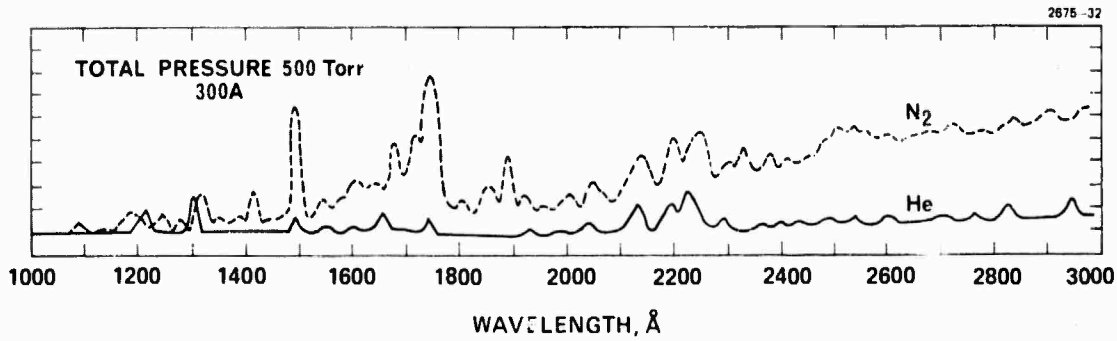

Figure III-13. Relative emission spectra of N_2 and He at 300 A.

A final spectra measured was that of the laser gas mixture. Two mixtures were studied with concentration of $CO_2/N_2/He$ of 0.5/0.10/0.85 and 0.025/0.3/0.675. The emission spectra, which of course, in this case is combined emission-abosrption spectra, for these mixtures is given in Figure III-14. It is apparent from these spectra, at these current levels, little radiation below 1600 Å passes through the gas as would be expected based on the mean free path data for CO_2.

To qualitatively demonstrate what affect the change in spectra observed in the above figures would have on the photoionization of Tri-n-propylamine photoionization yield measurements were made. For these tests the emission chamber was isolated from the photoionization chamber by a LiF window (see Figure III-10). The emission chamber was filled with either He, N_2, or a 0.5/0.10/0.85. $CO_2/N_2/He$ mix with the photoionization chamber filled with a 0.5/0.10/0.85 mix and Tri-n-propylamine. The sustainer energy results, shown in Figure III-15, illustrate the expected increase using N_2 as the emission gas. They do not however show an increase with He as might be expected based on the emission spectra.

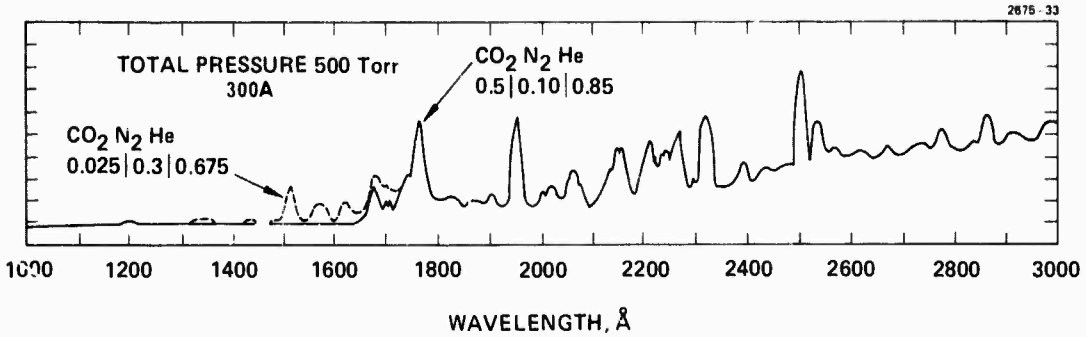

Figure III-14. Relative emission spectra of two $CO_2/N_2/He$ laser mixtures at 300 A.

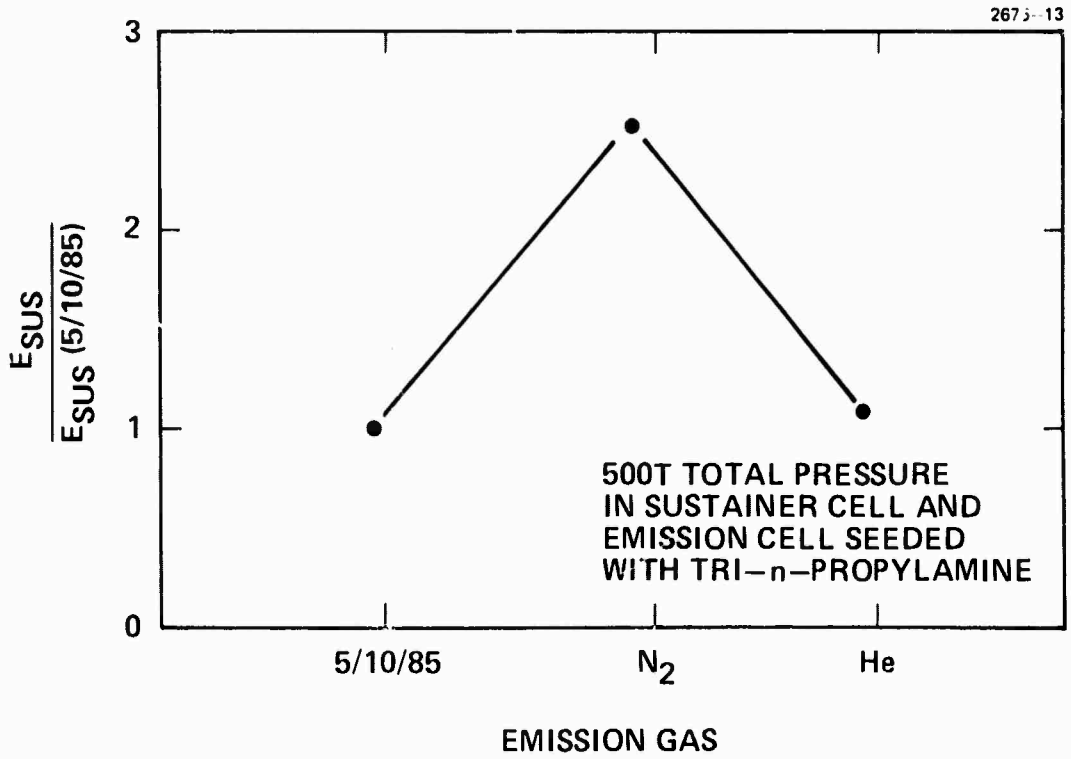

Figure III-15. Sustainer energy measurements obtained using different emission gases.

IV. SMALL AND MEDIUM SCALE DEVICE MEASUREMENTS

After demonstrating the basic processes occurring in UV sustained discharges (Section III) extensive measurements were undertaken on two phases of the UV sustained plasma conditioning scheme. The first was a parametric investigation to determine achievable levels of discharge input energy. Second, as a direct result of the demonstration of the capability to obtain input discharge energy densities that would efficiently excite CO_2 laser mixtures, small signal gain distribution, and power extraction measurements were performed on a medium scale device. These results are discussed in this section.

A. Input Energy and Mean Free Path Determination

The input energy measurements were performed on a small device which employed UV arc discharges located adjacent to the main discharge electrodes (see Figure IV-1). Both the UV source and main discharge electrodes were mounted in a high vacuum glass enclosure to permit accurate control of the discharge environment. All internal supporting components were selected from those materials with low vapor pressure and outgassing properties and with high resistance to seed gas additives. Various mixture ratios of CO_2, N_2, He, seed gas concentrations, total pressures, and UV spark energies were studied to allow a complete mapping of obtainable sustainer energy densities.

Before presenting the results of these experiments, and in order to provide a theoretical basis for the assessment of these data, we will first discuss a simplified calculation of the UV produced electron number density expected for such a system based on the processes described in Section III. In Figure IV-2, the computed-sustainer energy densities as a function of UV current are summarized for a wide range of gas mixtures. This calculation assumes single-step photoinization of the added seed gas (in this example, tri-n-propylamine is used) and a recombination limited plasma. From this figure, we see two important effects. First, there is a minimum CO_2 concentration below which no further increase in sustainer energy results. As the CO_2 concentration

2768-1

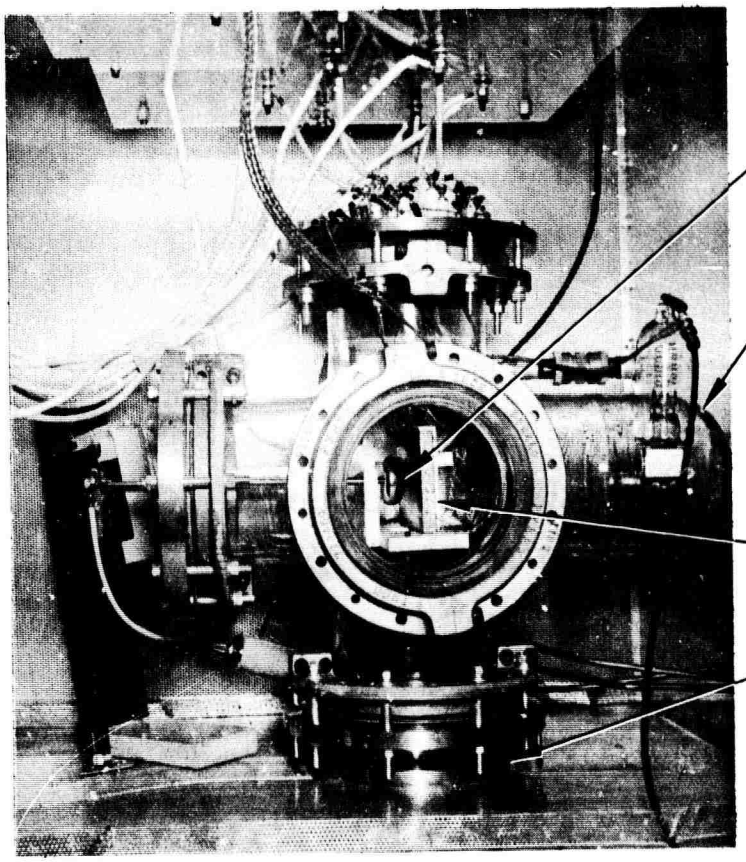

2768-2

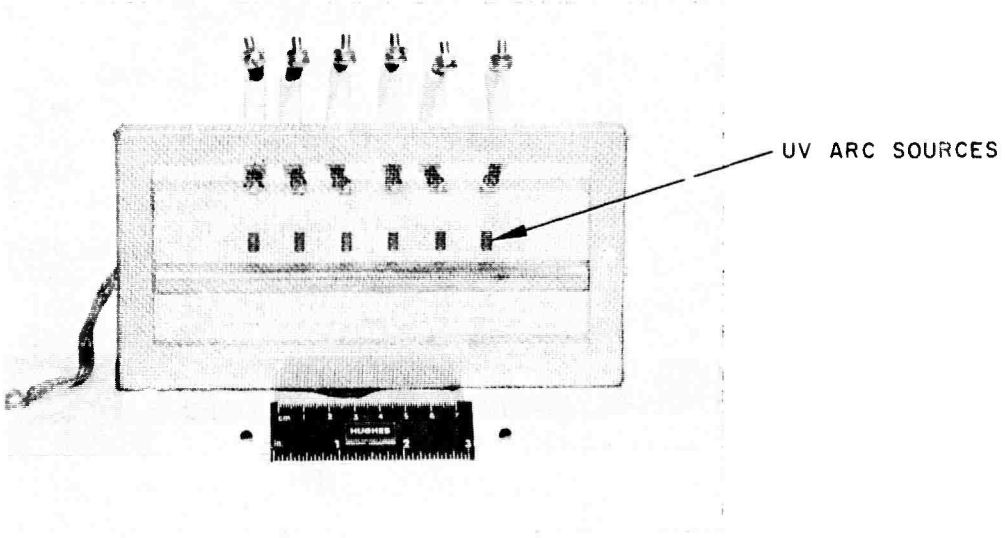

Figure IV-1. Experimental UV sustained discharge device.

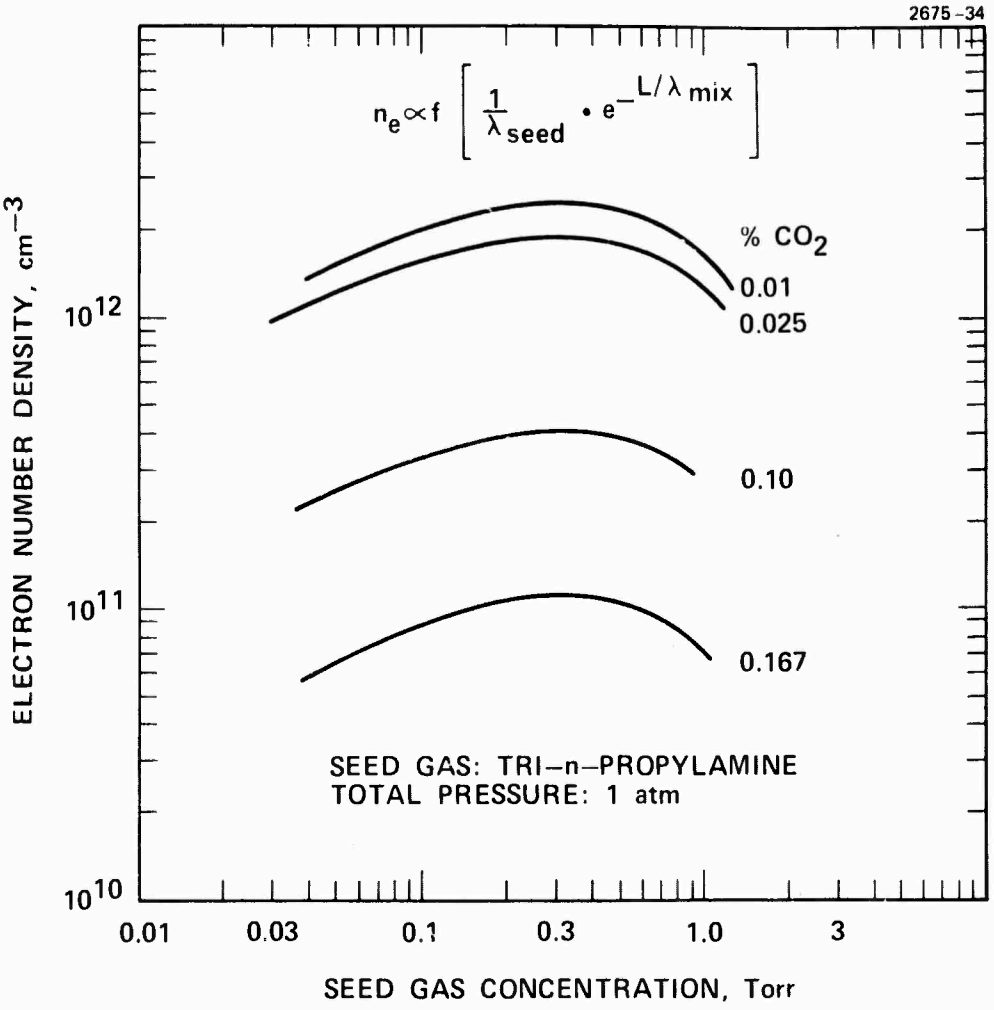

Figure IV-2. Calculated electron number density.

decreases, the effective mixture mean free path is determined by the seed gas concentration. Second, there is a broad optimum in sustainer energy for a large (order of magnitude) change in seed gas concentration which produces only a small variation in the sustainer energy because at low seed gas concentrations the UV absorption characteristic is dictated by CO_2 molecules, and only when the seed gas concentration is increased does the seed gas absorption play a dominant role. Both of these effects are critical to the determination of the limiting mean free path and hence the limit of scalability.

Two of the results of the experimental study are shown in Figures IV-3(a) and IV-3(b). First, in Figure IV-3(a), the normalized sustainer energy obtained as a function of the normalized UV spark current is plotted for four mixture ratios and fixed seed gas concentrations while in Figure IV-3(b), similar plots are for three seed gas concentrations with a fixed mixture ratio. We see that the results of these experiments follow the trends predicted above.

Figure IV-4 gives the absolute sustainer energies obtained for the mixture producing the largest relative energy density results shown in the previous figures. With a UV spark current of 3 kA a value of 300 J/liter-atm has been obtained. The pulse lengths corresponding to these energies depend solely on the pulse length of the UV source; for the present case, this corresponds to an underdamped ringing arc circuit of approximately 50 μs in duration.

The effective mean free paths of the CO_2 and seed gas molecules have been evaluated and are summarized in Table IV-1. For a typical CO_2 mixture of 0.015 atm of CO_2 and 0.3 Torr of seed gas, the effective mean free paths are 11 cm and 20 cm, respectively, whereas the corresponding overall mixture mean free path is approximately 8 cm. Further conformation for this projected mean free path comes from the demonstrated result that the dense plasma was produced by radiation with wavelengths between approximately 1200 and 1700 Å with more than 60% between 1500 to 1700 Å. This result can be explained by examination of the mean free path through CO_2 shown in Figure IV-5. Because the ionization potential of tri-n-propylamine is 1720 Å, we conclude that

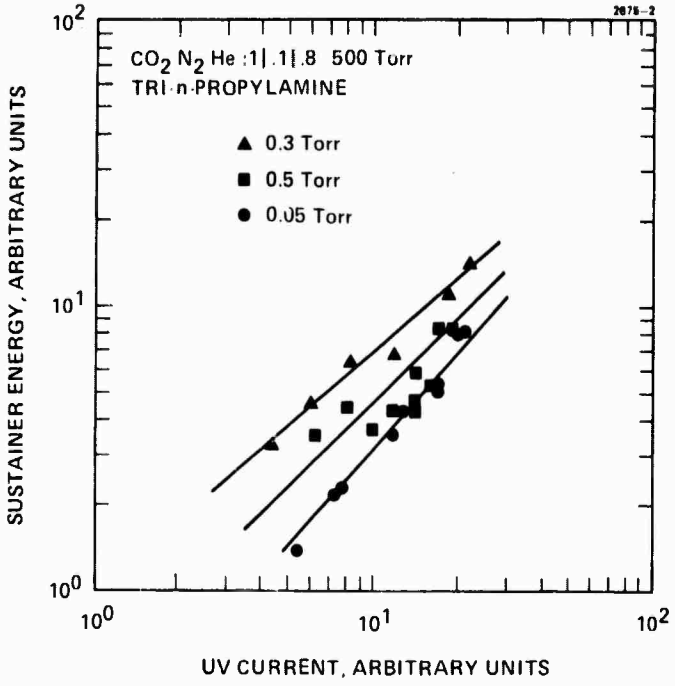

a. For various laser mixtures.

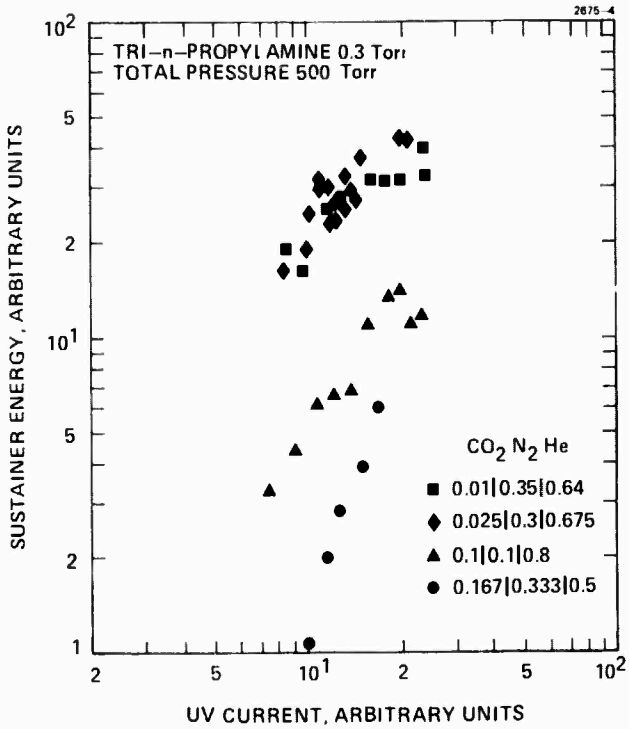

b. For various concentrations of tri-n-propylamine.

Figure IV-3. Sustainer energy as a function of UV current.

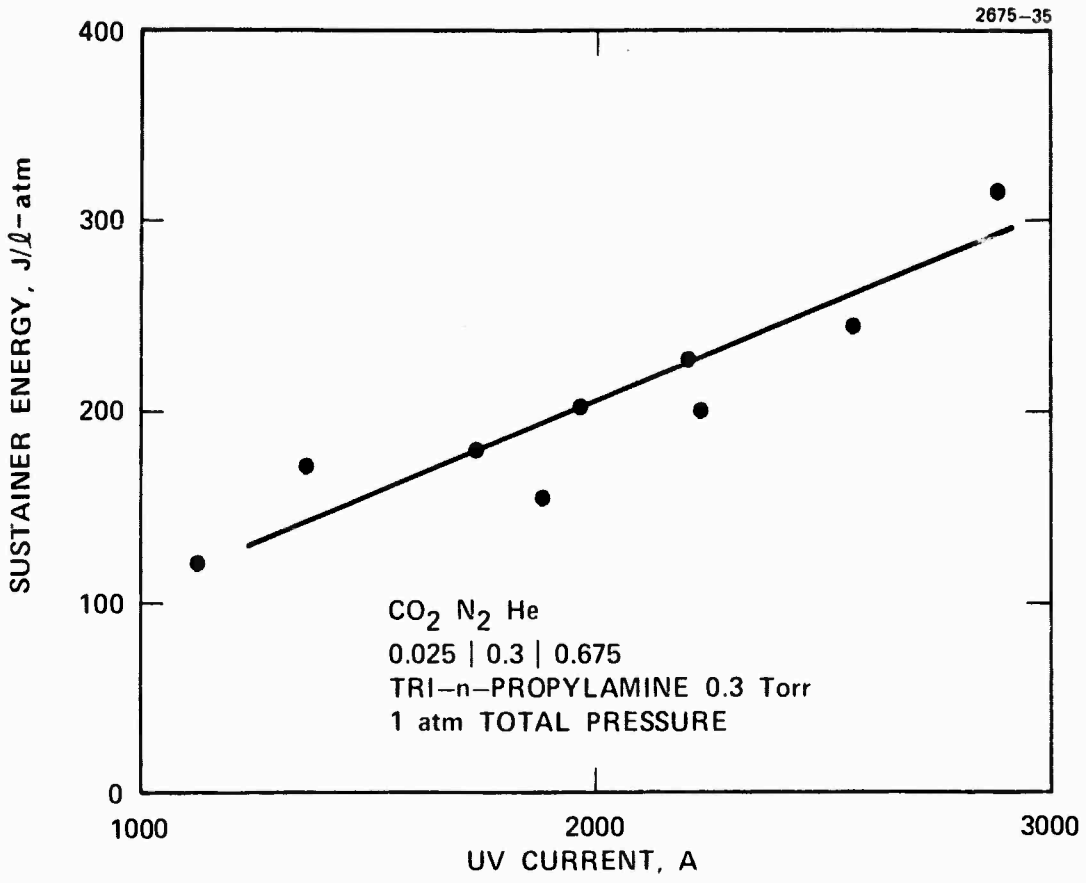

Figure IV-4. Maximum input sustainer energy in J/l-atm as a function of UV current in amps.

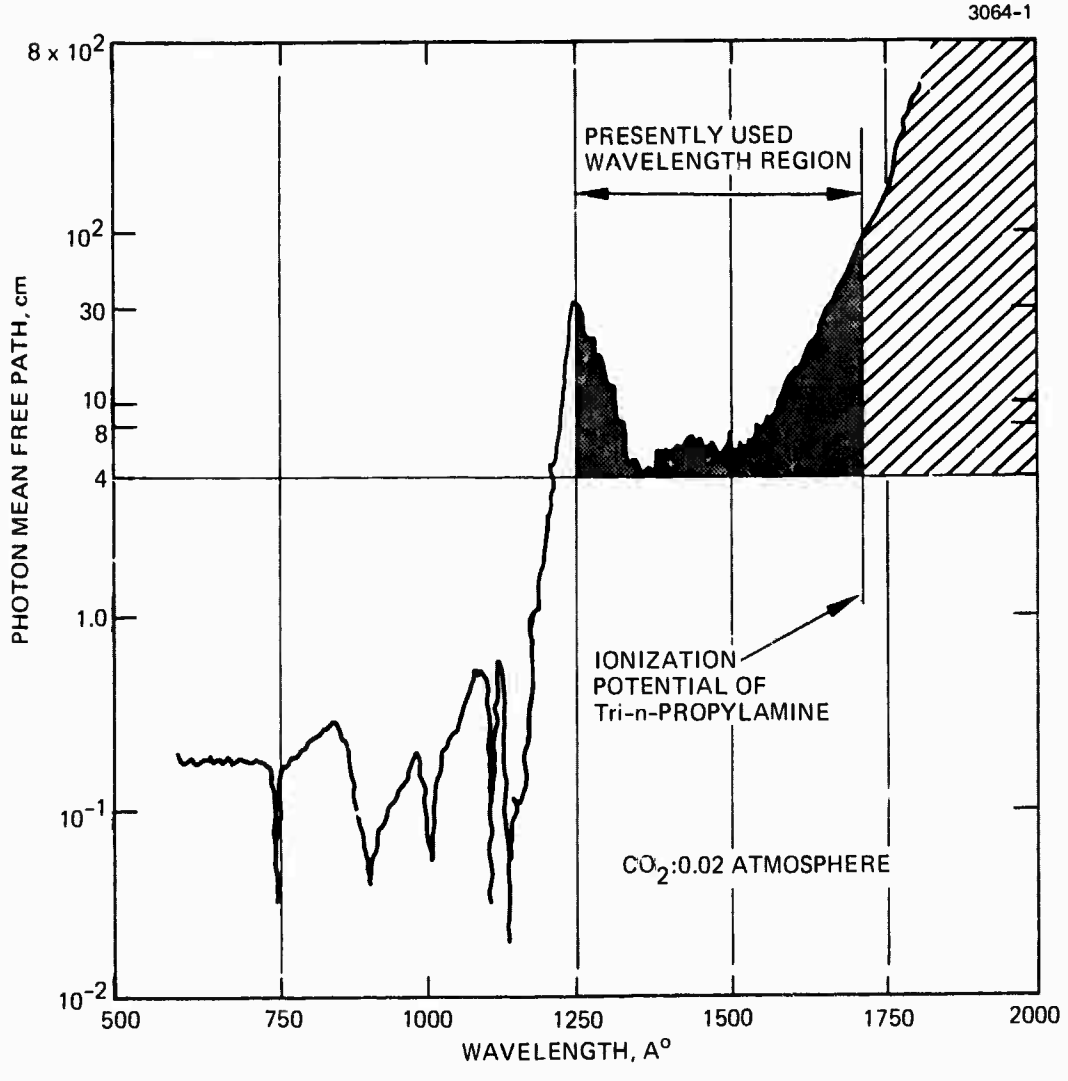

Figure IV-5. Ultraviolet photon mean free path through CO_2 at 0.02 atm.

TABLE IV-1

Measured Effective Mean Free Paths of CO_2 and Seed (tri-n-propylamine) Gas

Molecules	Effective Mean Free Path[a] cm-Atm
CO_2	0.16
Tri-n-propylamine	8×10^{-3}

[a]Typical mixture of 1 atm: CO_2:N_2:He:seed gas 0.02: 0.3:0.7:0.004.

T1195

single step photoionization is the production mechanism for the plasma. It is clear from the mean free path shown that below 1200 Å no radiation is transmitted through any reasonable size device that uses CO_2; thus we arrive at the limiting wavelengths obtained experimentally.

B. Small Signal Gain and Power Extraction – Medium Scale Device

The gain and power extraction measurements were performed on a larger discharge device employing an improved source for the UV radiation. The source consists of small copper squares located on an alumina dielectric surface with a low inductance copper ground plane below the alumina surface (Figure IV-6). Such a scheme produces a two-dimensional array of cascaded arc discharges across the dielectric substrate. Each row is energized by its own low inductance capacitor. The principal factor in the operation of this scheme is the small but finite capacitance to ground from each arc to the ground plane. This capacitance reduces the voltage drop required across the complete series of arcs to that required for self-breakdown of one only. Thus, the voltage remains at a high value and, therefore, the energy transfer is more efficient.

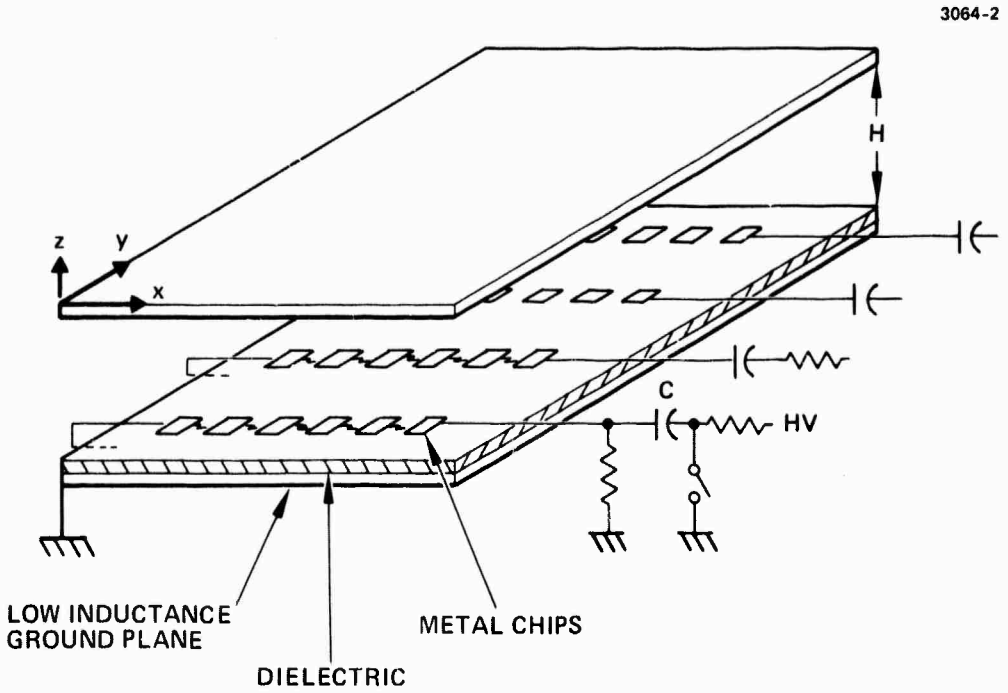

Figure IV-6. Cascaded arc discharge system.

To test the feasibility of this cascaded arc discharge source to UV sustained plasma conditioning, a medium volume (2.5 x 15 x 50 cm^3) test device was constructed from an existing laser testbed. This device had a Bruce profiled cathode located 2.5 cm from a flat mesh anode. Brewster angle windows were employed for use with external laser optics which consisted of a 4.5 m total reflector and a 20% transmitting dielectric coated output mirror.

Figure IV-7 gives typical current traces for the cascaded arc circuit and the sustainer plasma discharge obtained in a UV sustained mode. Figure IV-7(a) was obtained at an E/N = 1.7×10^{-16} V-cm^2 and Figure IV-7(b) at an E/N = 1.85×10^{-16} V-cm^2. For the higher E/N the discharge is terminated by an arc occurring at approximately 22 μs into the pulse. Also, for the arc circuit, ringing occurs indicating that even though this UV source is more efficient there is a certain degree of impedance mismatch because of unavoidable circuit inductance.

The energy input to the discharge was calculated by integrating the area under sustainer current curves such as these and then multiplying by the dc bias voltage. For the results of Figure IV-7 this corresponds to about 350 J input which was the maximum value obtained for all cases run. By operating at higher bias voltages arcing occurred much earlier in the pulse and hence led to the attainment of smaller input energies. The calculation of energy density depends on the discharge volume (which at this time has not been determined with a high degree of accuracy). However, taking the physical size of the electrode of 15 cm by 50 cm as the discharge area we find that an input energy density of 200 J/liter-atm has been obtained for the above case.

The small signal gain was also measured for various mixtures, bias voltages (E/N), and position. A typical gain waveform is shown in Figure IV-8. This trace was obtained at a point of 3.5 mm from the mesh anode, position 1 (see Figure IV-9 for orientation), which corresponds to a location approximately 2.5 cm from the cascaded arc discharge UV source. From this trace the arrival of the acoustic disturbance from the UV source to the point where the probe laser is located is evident. The gain is observed to rise continuously throughout the pulse.

3064-3

CO_2 N_2 He 0.028 | 0.472 | 0.50
Tri-n-PROPYLAMINE 0.3 Torr
P_{TOTAL} = 700 Torr

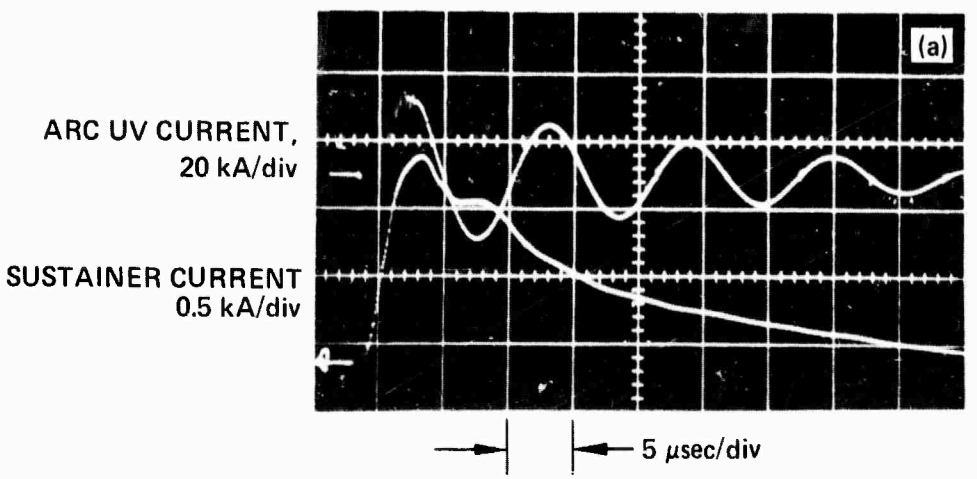

3064-4

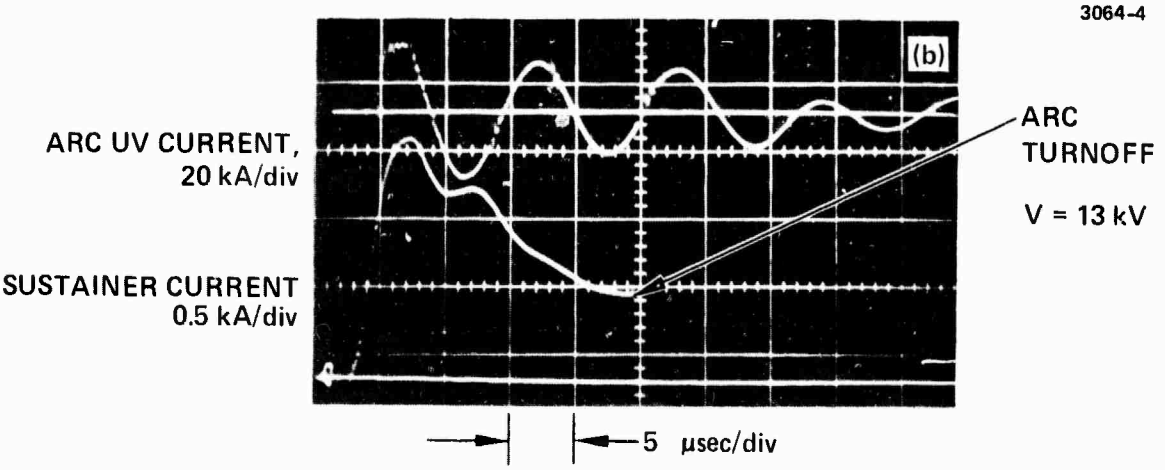

Figure IV-7. Sustainer current and cascaded arc discharge current waveforms.

3064-5

CO_2 N_2 He 0.028 | 0.327 | 0.645
Tri-n-PROPYLAMINE 0.3 Torr
P_{TOTAL} = 700 Torr

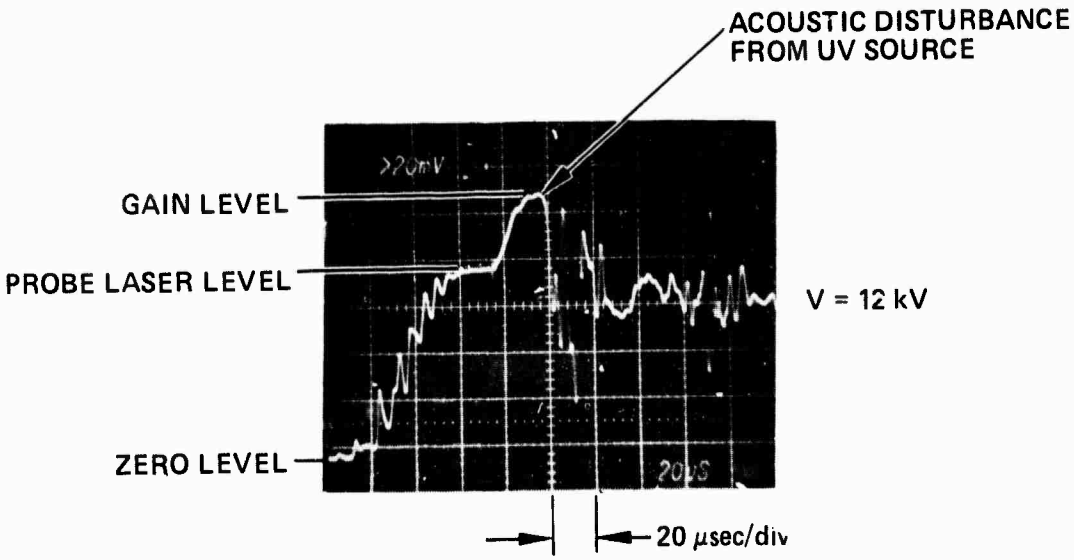

Figure IV-8. Small signal gain waveform at position 1.

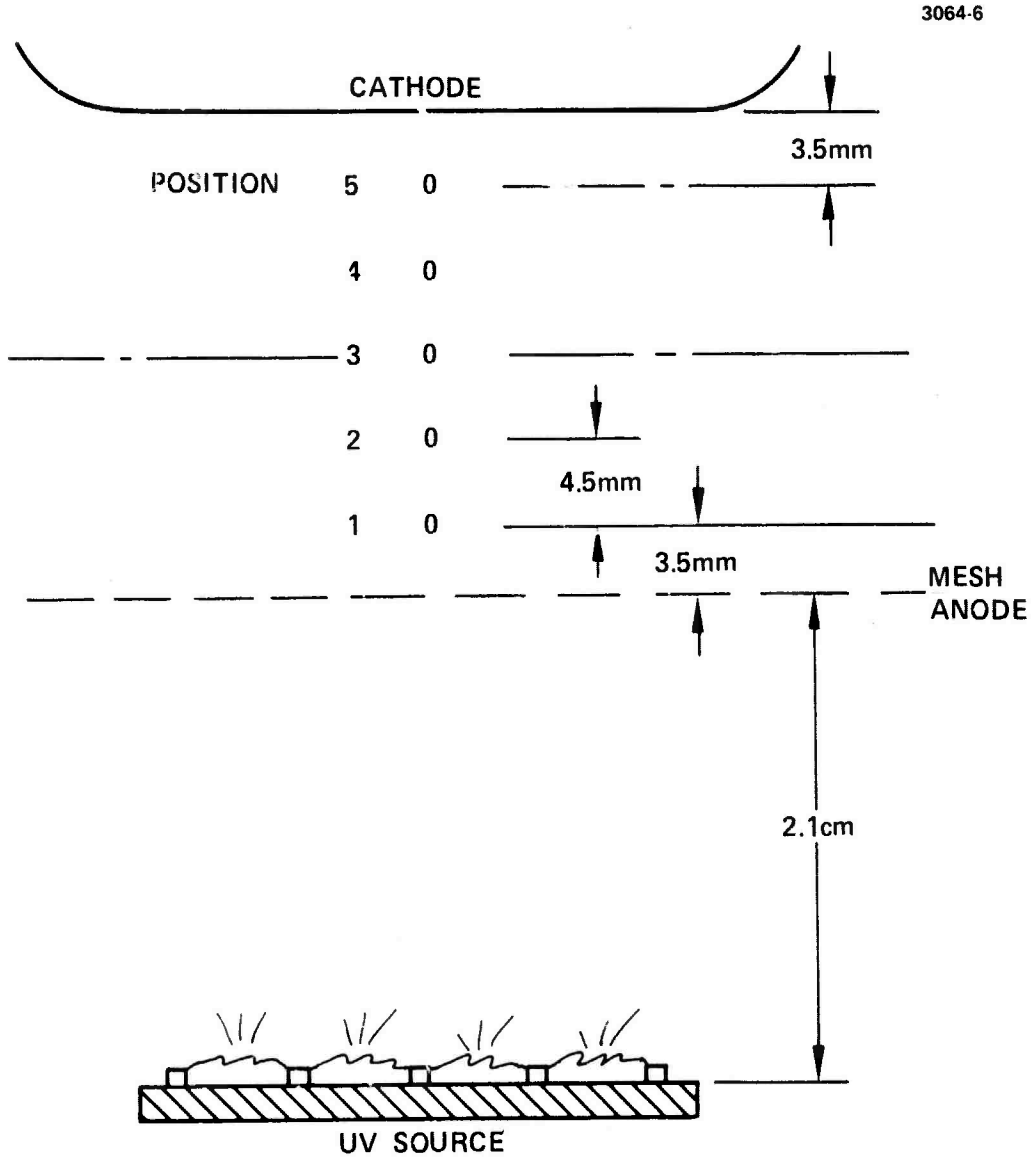

Figure IV-9. Continuous wave pr ›e laser positions.

The gain distribution across the gap spacing was measured for various bias voltages. The results for a CO_2, N_2, He 0.028/0.472/0.50, 0.3 Torr tri-n-propylamine mixture are shown in Figures IV-10 and IV-11. In Figure IV-10 the gain as a function of bias voltage for the five probe positions is given. The gain varies in a nearly linear manner except for the position nearest the cathode where the gain begins to level off with increased voltage as observed in e-beam pumped systems. In Figure IV-11 the gain as a function of position for three bias voltages is given. We see here that the gain increases, as opposed to decreasing, as the distance from the UV source increases. These results are indicative of the field strength increasing to maintain constant current, as n_e decreases moving away from the UV source, and thus rising to a value where possibly some local avalanching by the seed gas is occurring. In addition, the much higher gain near the cathode is a typical result seen for gain behavior in the cathode sheath region. To indicate the very different nature of the gain waveforms near the cathode, the results obtained at position 5 are given in Figure IV-12. Figure IV-12(a) is for 12 kV bias voltage and shows maximum pumping at the beginning of the pulse, because of the much higher n_e levels than obtained at position 1, and subsequent heating of the lower laser level during the remainder of the pulse (see Figure IV-8). Figure IV-12(b) is for 8 kV bias voltage, and thus, much lower n_e levels, and shows pumping throughout the pulse duration but at a rate much lower than the case shown in Figure IV-8 which was for 12 kV bias voltage.

Extensive measurements of laser output were made using a stable cavity arrangement and a Hadron Model 117 calorimeter. The measurements consisted of keeping the UV source energy fixed and varying the bias voltage (E/N) of the discharge and varying the gas mixture. Typical laser pulse shapes are shown in Figure IV-13. The laser output shown in Figure IV-13(a) and IV-13(b) corresponds to the cases discussed previously and shown in Figure IV-7(a) and IV-7(b), respectively. Figure IV-13(a) gives a pulse with a multimode energy of 9.6 J and a pulse length of 37 μs. Figure IV-13(b) gives a pulse with a multimode energy of 12 J with a pulse that is terminated by an arc which occurs 22 μs into the pulse.

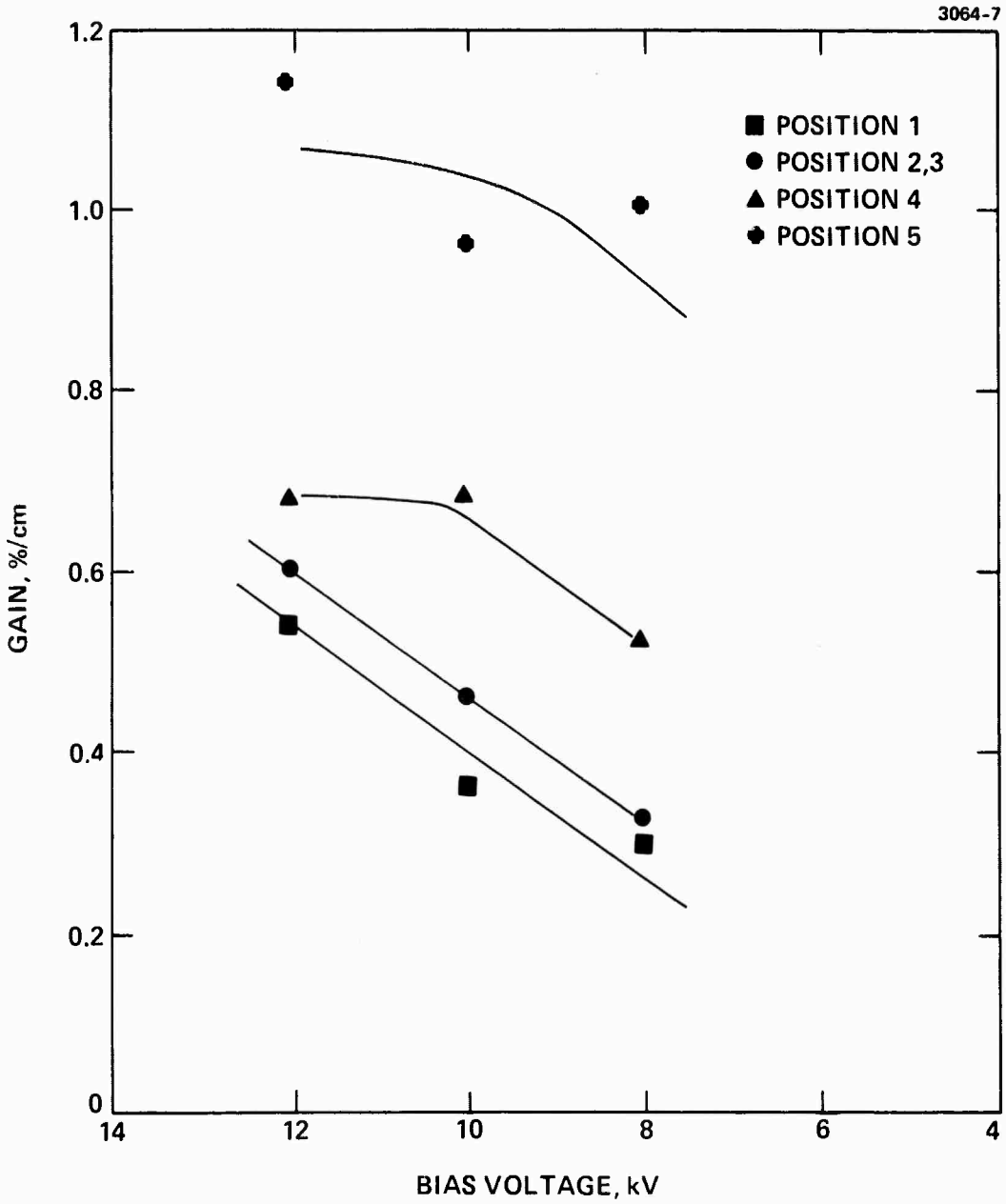

Figure IV-10. Small signal gain as a function of bias voltage for five positions.

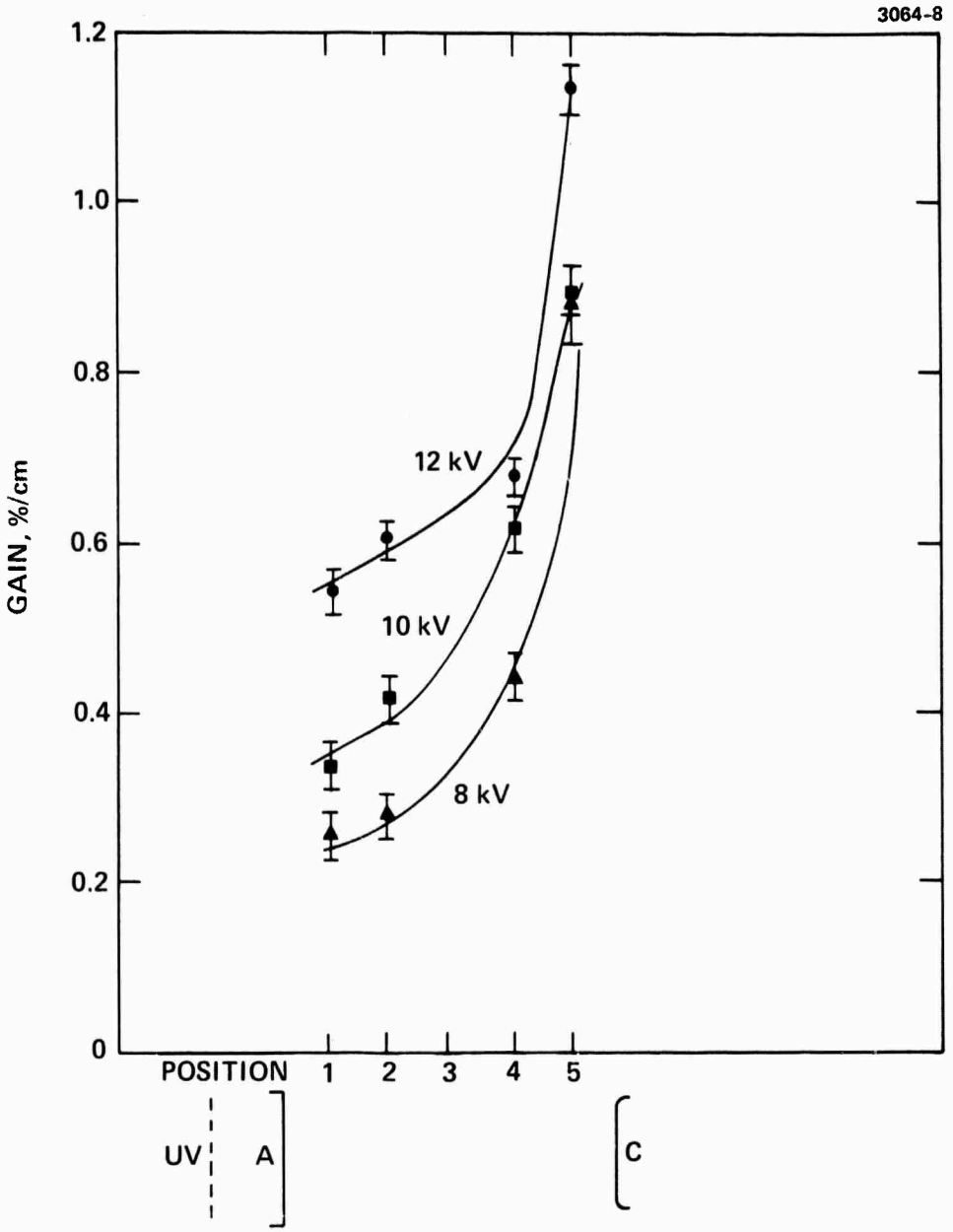

Figure IV-11. Small signal gain as a function of position for various bias voltages.

3064-9

CO_2 N_2 He 0.028|0.472|0.50

Tri-n-PROPYLAMINE 0.3 Torr

P_{TOTAL} = 700 Torr

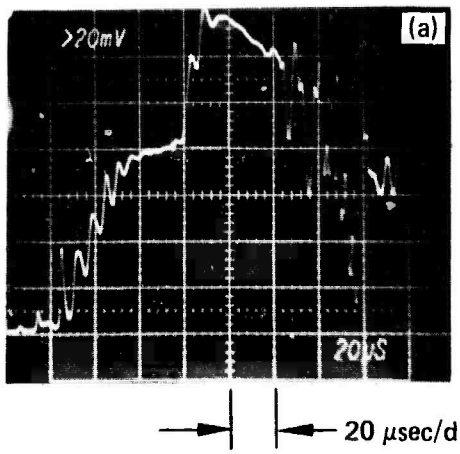

V = 12 kV

20 μsec/div

3064-10

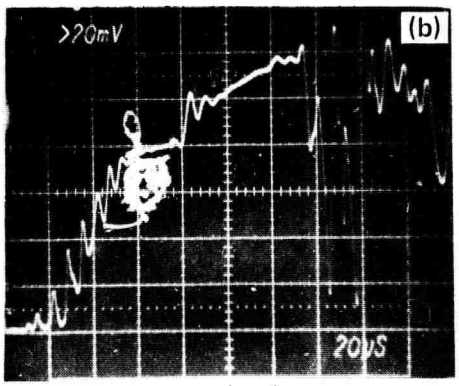

V = 8 kV

20 μsec/div

Figure IV-12. Small signal gain at position 5 for two bias voltages.

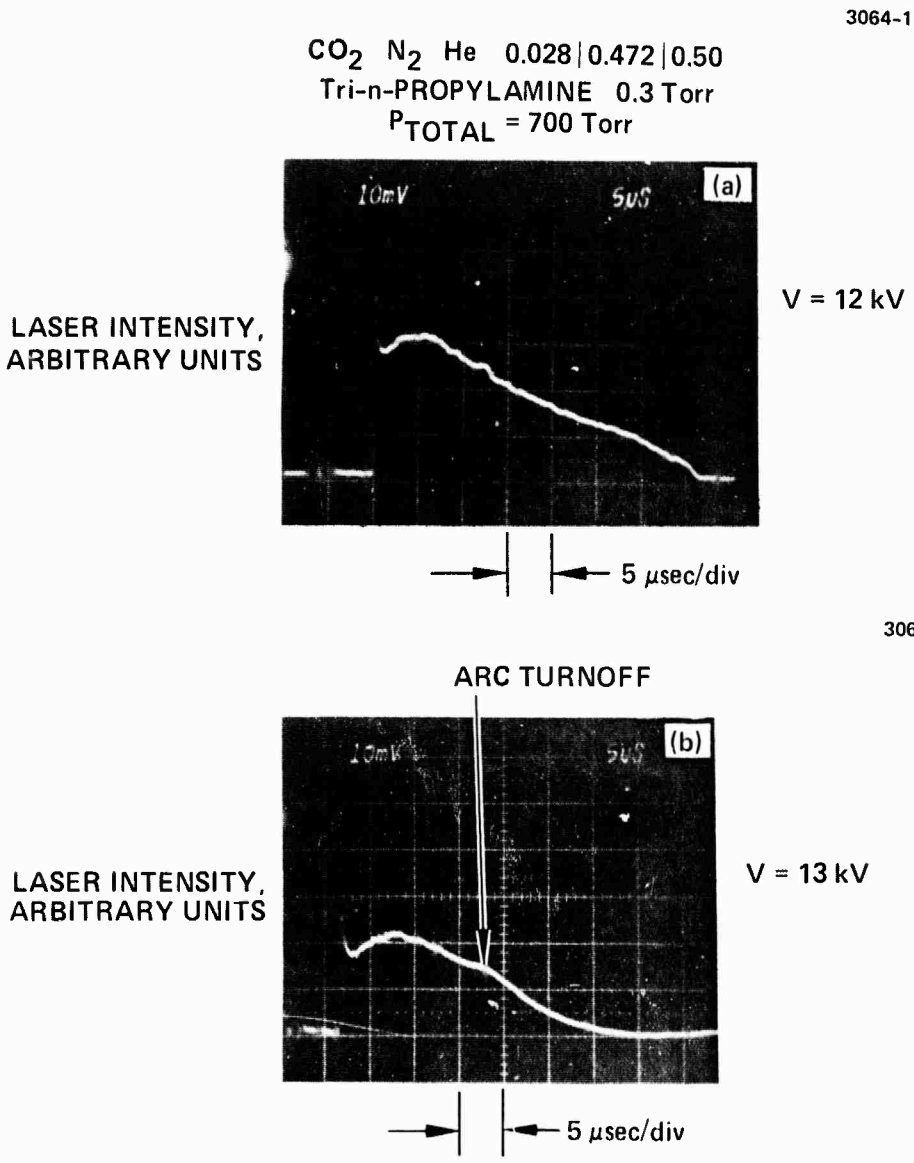

Figure IV-13. Laser pulse shape.

The nearfield burn pattern for the laser output is shown in Figure IV-14. This pattern was obtained by using thermal chart recording paper. However, to determine the mode area more accurately, exposed photographic paper was used. This gave a slightly larger area than that shown. With the mode volume established in this manner the laser output energy density can be determined. For the 37 μs pulse of Figure IV-13(a), 47 J/liter-atm was obtained, and for the shorter pulse (≈29 μs) of Figure IV-13(b), 61 J/liter-atm was obtained.

To indicate a typical variation in output with E/N, Figure IV-15 gives such results for three CO_2N_2He, tri-n-propylamine mixtures. The fact that the output is lower at the largest E/N for the higher CO_2 concentration case results from an arc which occurred early in the pulse and lowered the obtainable input energy.

To calculate the electrical-to-optical conversion efficiency the input energy density is required. Using the estimated 200 J/liter-atm value discussed previously we find that an efficiency of about 20 to 25% is obtained. (This efficiency calculation does not include the UV source energy.)

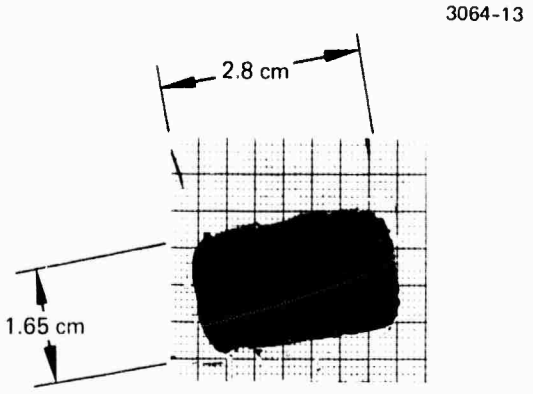

Figure IV-14. Near-field burn pattern.

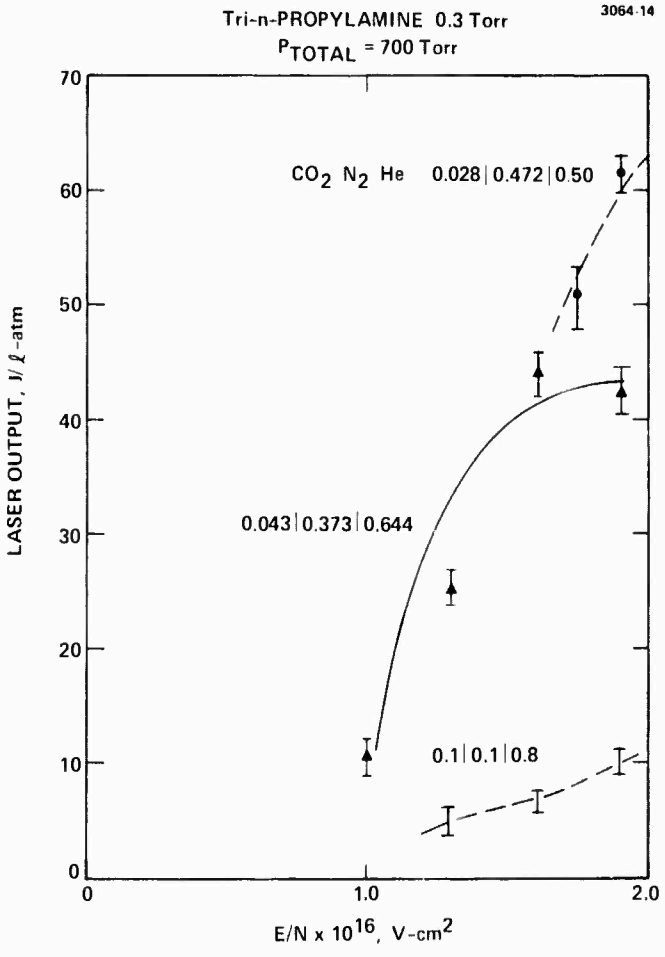

Figure IV-15. Laser output as a function of E/N.

V. LARGE SCALE DEVICE

A major portion of the contract has dealt with design, construction and testing of a large scale UV sustained laser testbed. In this section a description of the mechanical and electrical properties of the device, together with a description of an arc sensor circuit is given. This is followed, in Section VI, by a detailed discussion of the extensive measurements performed with the device.

A. Device Configuration

The general concept of the device is that of a large vacuum chamber in which Bruce contoured electrodes are housed. A high energy (up to 50 kJ), 80 kV, dc storage bank is used to provide the necessary bias voltage to the electrodes. The UV source, which is the crucial element in the device, is located behind each electrode and irradiates the discharge volume through mesh screens that are wrapped around the electrodes.

The general layout of the laboratory in which the large scale device is located, is shown in Figure V-1. In this photograph we see the large vacuum chamber which houses the electrodes, the gas handling system, and the control console. Figure V-2 shows one electrode installed in the vacuum chamber viewed from a direction looking toward the mesh screen. The screen is an approximately 50% transmitting stainless steel mesh through which the UV radiation passes. The next photograph (Figure V-3) shows the mounting of the UV source energy storage bank in relation to the electrode and UV cascaded arc discharge source (one bank for each electrode). The UV source energy bank is located in this manner to minimize wire lengths and hence loop inductance, in order to maximize delivery of the stored energy to the UV arcs. The UV source itself is shown in Figure V-4. The source consists of cascaded arc discharge boards with approximately 40 rows of arcs, each row having copper chips 3 mm x 3 mm along the 100 cm discharge length. Each row is energized by a separate 0.1 μF, 25 kV low inductance capacitor (shown installed in the previous figure).

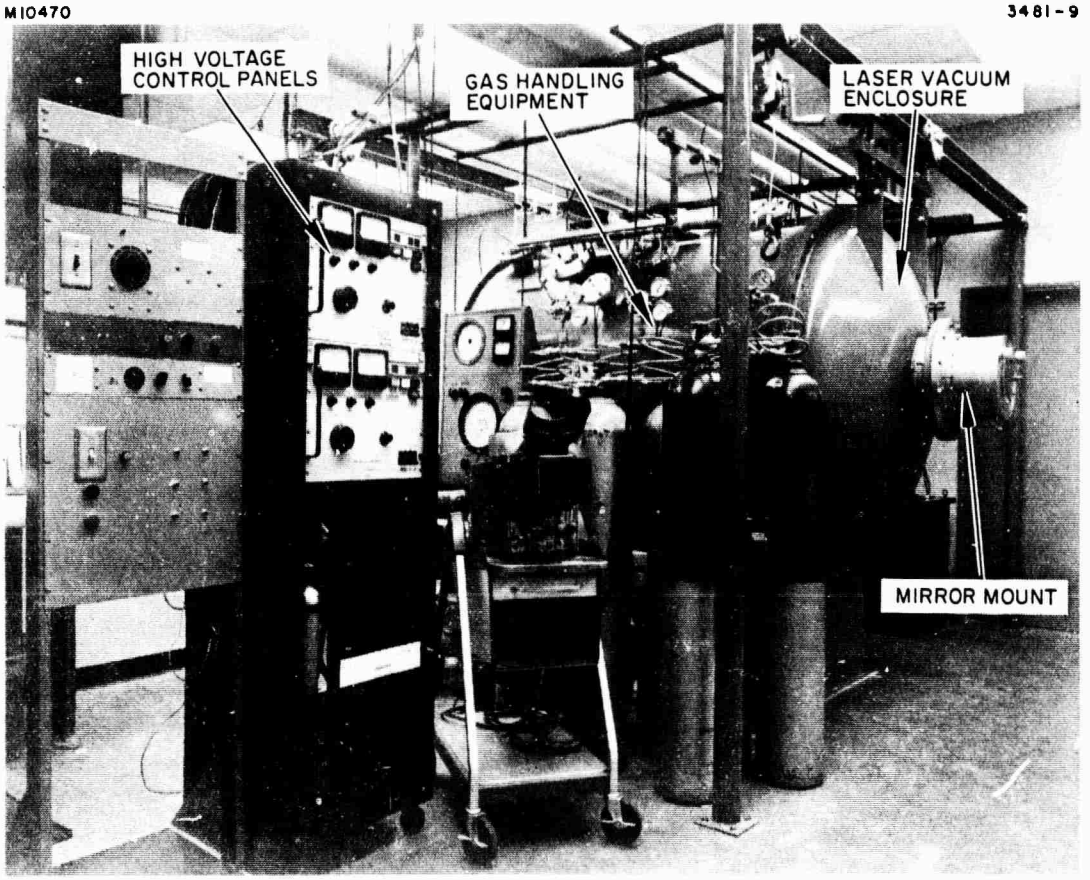

Figure V-1. Device and associated equipment.

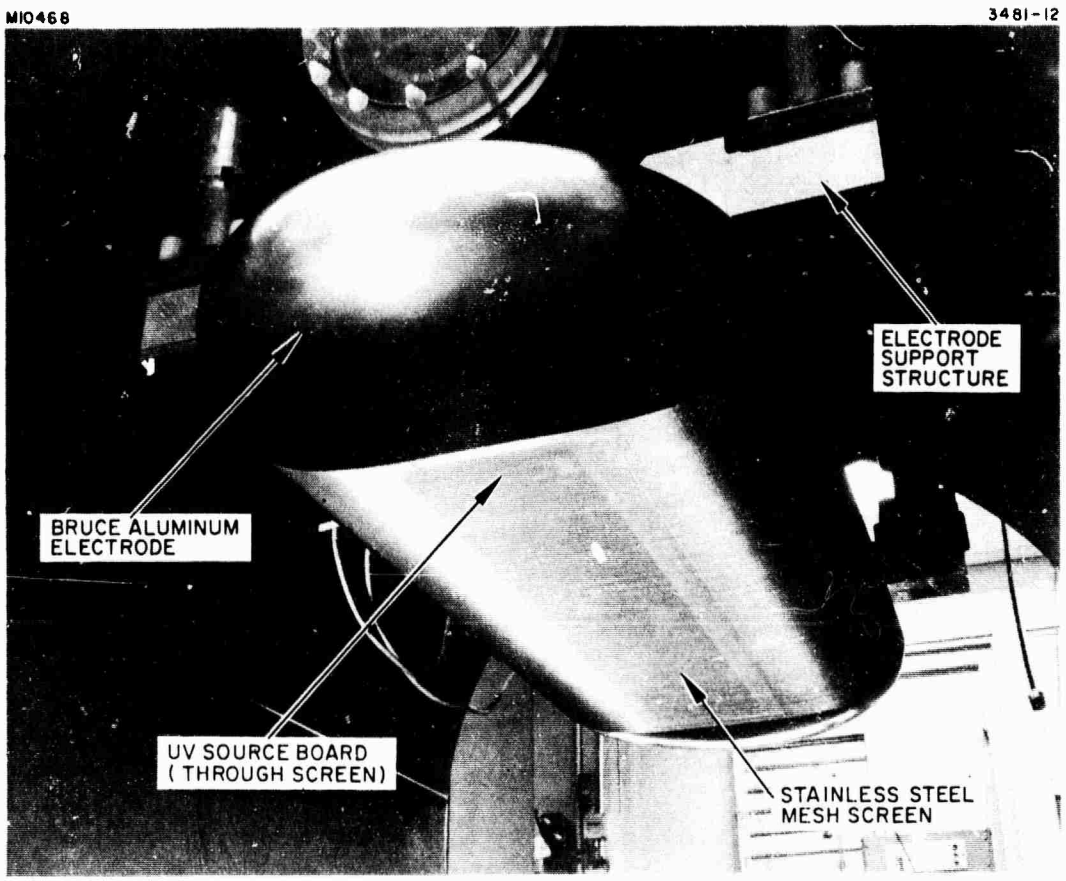

Figure V-2. Upper electrode.

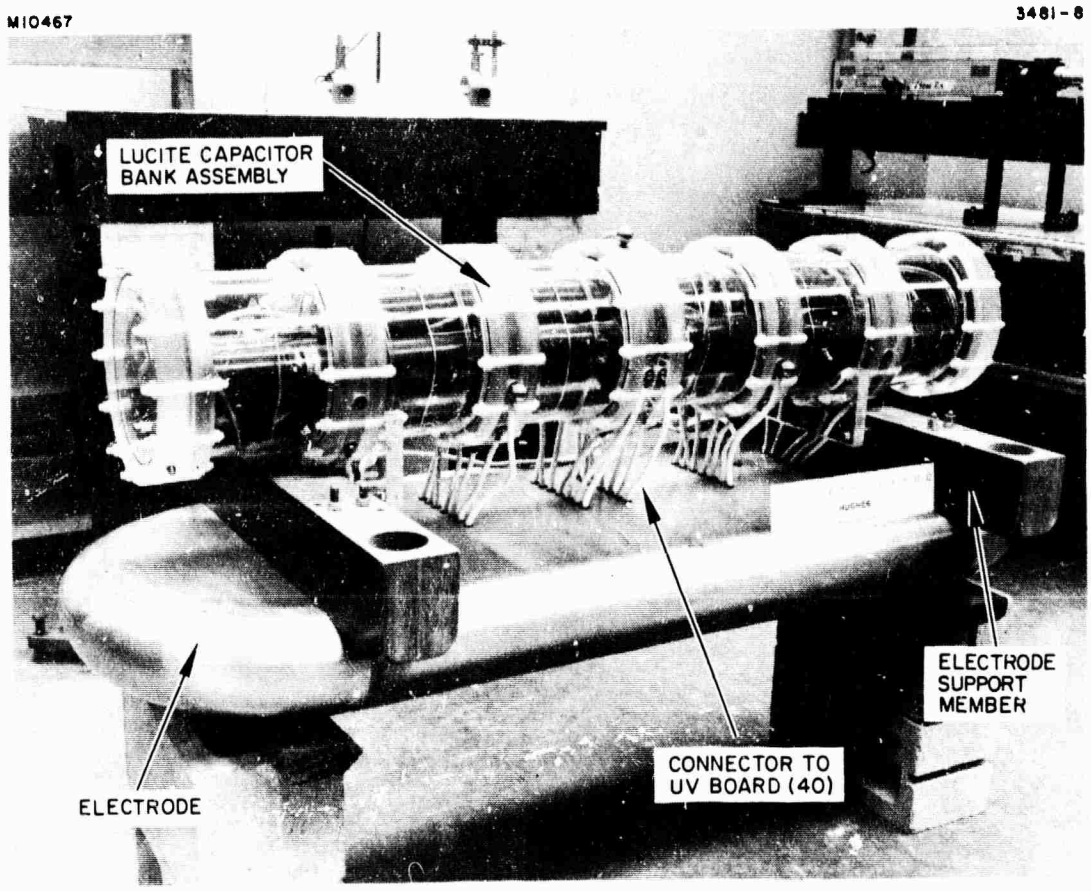

Figure V-3. Ultraviolet source capacitor bank assembly.

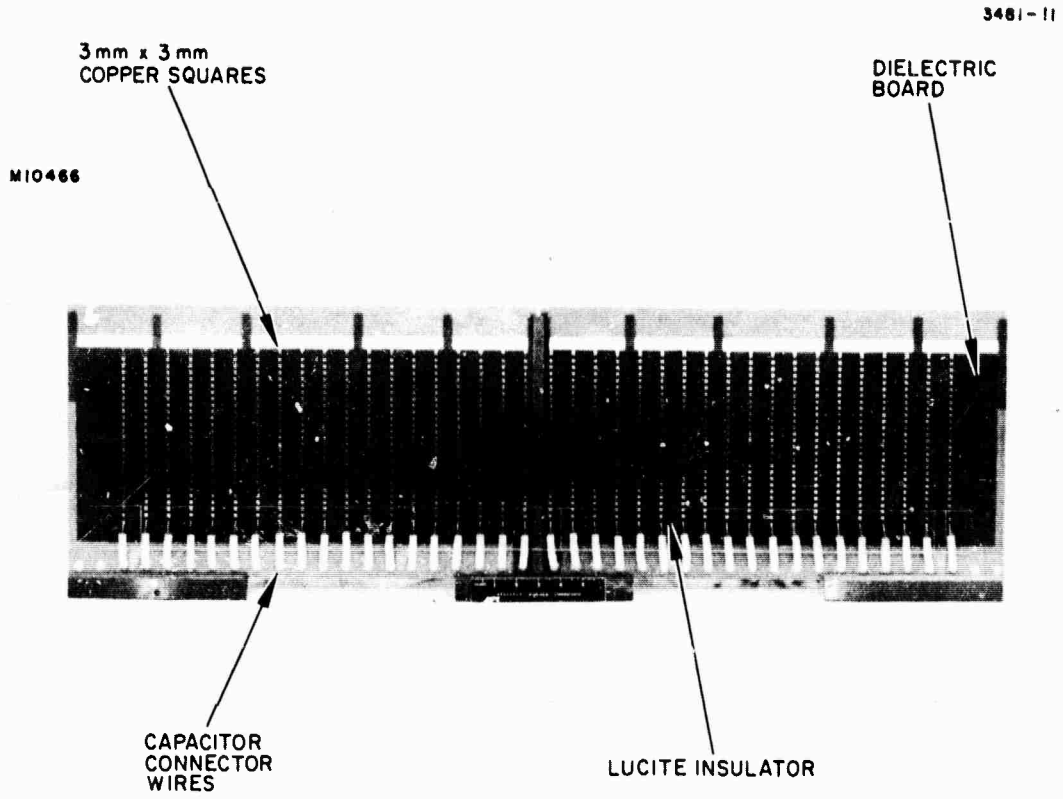

Figure V-4. Ultraviolet source boards.

Figure V-5 depicts the assembled discharge device. Shown are the N_2 spark gaps that fire the UV source capacitor banks, the spray bars that ensure proper gas mixing, and the electrode support columns and spacers which in the present configuration give a 6 cm electrode spacing.

To ensure proper mixing of the organic seed gas molecules (tri-n-propylamine) in this large volume device (2800 liters) an arrangement different than that used on the previous small and medium scale experiments is employed. Here the seed molecule is injected into a flowing gas stream of N_2 immediately downstream of a sonic orifice ensuring complete breakup of the liquid into tiny droplets, vaporizing, and mixing as the stream enters the discharge chamber.

B. Electrical Characteristics

The short-term power requirements for the UV sustained laser are relatively large, and this energy is more easily stored in capacitors for delivery upon demand.

A schematic of the laser chamber, showing in cross section the discharge electrodes, is presented in Figure V-6. Immediately in back of each electrode are indicated circular arrays of the 0.1 μF, 25 kV energy storage capacitors mentioned before which deliver energy to the arrays of spark gaps. These are interior to the large chamber. Energy to the main electrodes is delivered from an external storage bank through the chamber wall by means of feedthroughs which are also shown in Figure V-6. A single triaxial cable from the external energy storage bank (ESB) is used. The center conductor is at the highest potential (to -70 kV) and is carried through to the lower main discharge electrode. The cable has two outer shields separated by 0.080 in. of PVC. The innermost of these shields, which is at ground potential, is carried through the chamber wall to the upper discharge electrode and conducts the return current from the discharge back to the ESB. The outermost shield is at instrumentation ground and serves to minimize unwanted pickup in the data retrieval instrumentation. A current transformer surrounds the shielded return cable to measure the discharge current.

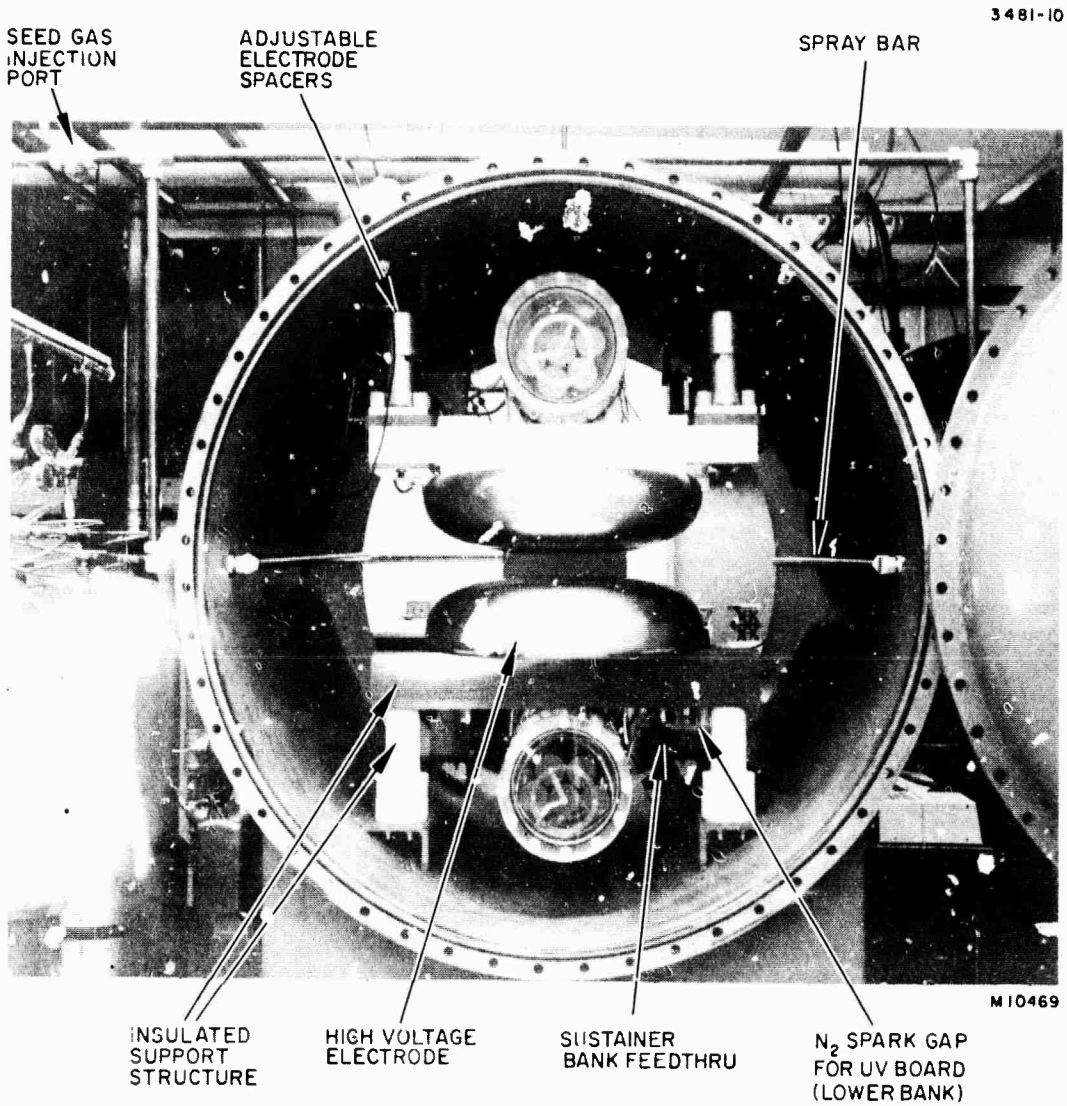

Figure V-5. End view of assembled device.

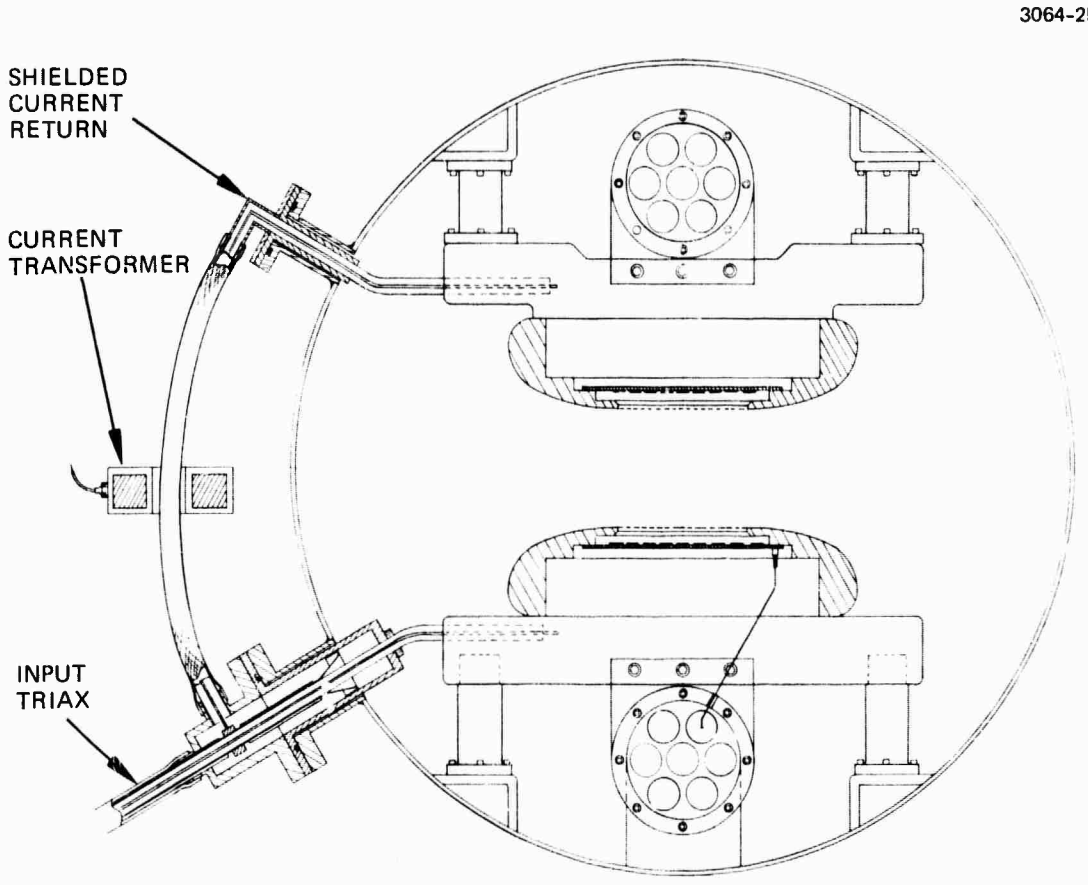

Figure V-6. Electrical feedthrough design.

Figure V-7 shows a more detailed layout of the electrical system. The main ESB consists of 64 capacitors, each rated at 1 μF, 40 kV, charged through a resistor from a high voltage supply. A diverter (crowbar) circuit is provided to dump the bank energy either on demand or upon a system malfunction such as an arc. The diverter consists of a triggerable spark gap in series with two paralleled 4 Ω electrolytic resistors. The ESB and the diverter are packaged in a single oil-filled steel tank and the output is the triaxial cable described previously. The capacitors in the main ESB can be connected in five basic configurations corresponding to the needed range of voltage and energy requirements.

Also shown in Figure V-7 are the two energy storage banks which feed the UV gap arrays. There is a total of 84 capacitors, 42 for each electrode, mounted in arrays of seven. One capacitor is dedicated to each individual row of gaps. Two triggerable spark gaps are used at each electrode, each of which dumps 21 capacitors when fired. The upper electrode UV capacitor bank is isolated to float with the electrode potential. Each electrode system of 42 capacitors is contained in a cylindrical air-filled plastic tube. Throughout the entire electrical system the usual protective devices such as discharge bleed resistors, automatic shorting circuitry, and overvoltage protection are utilized.

Typical operation of the system is indicated by the schematic of Figure V-8. The main ESB and the UV storage banks are charged manually at the control panel. At initiation, all 60 Hz power connections are disabled, after which the four UV bank spark gaps are simultaneously fired. The delay between line power disable and the UV gap firing is on the order of milliseconds. The laser then operates for a preset time period variable between 2 to 100 μs at the end of which the diverter is activated, dumping the remaining charge in the ESB. In the event that an arc is sensed, the 2 to 100 μs delay is overridden and the ESB is automatically crowbarred (see below for a detailed discussion of the arc sensing unit). There is also a manual override so that the ESB energy may be diverted at any time according to the operator's discretion.

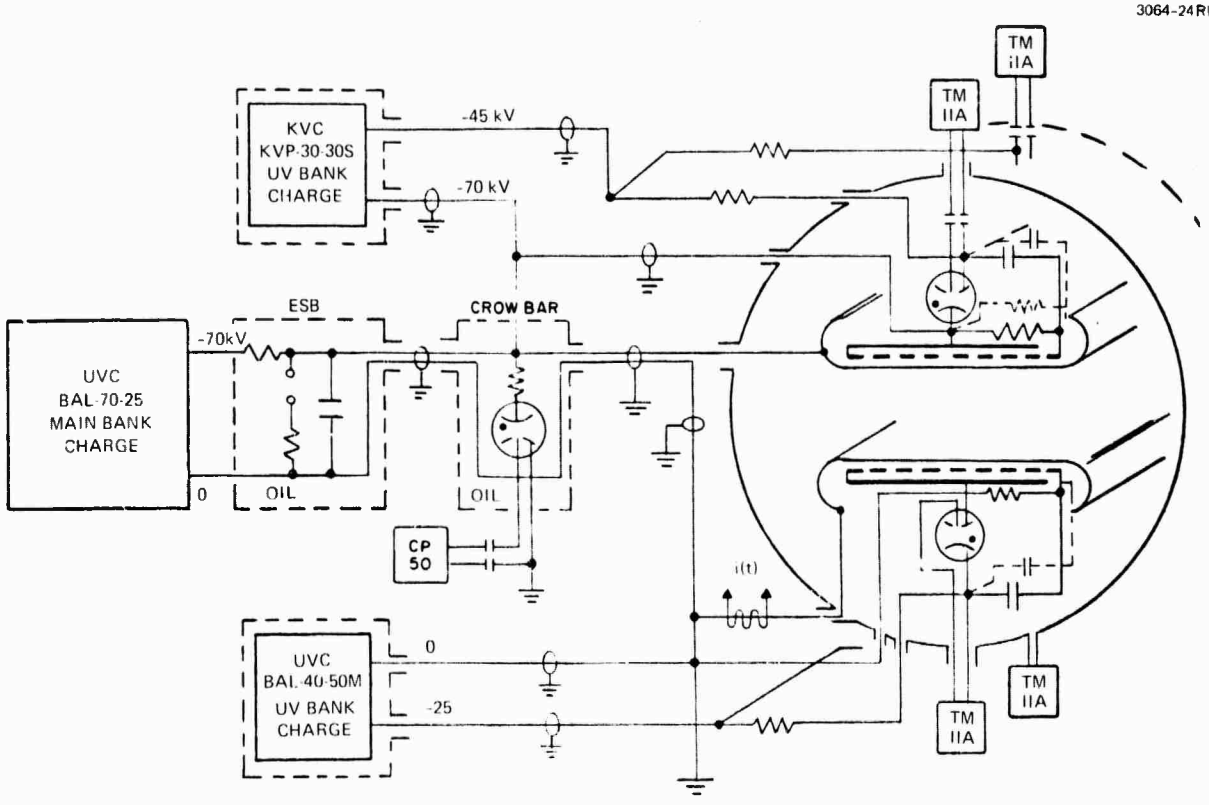

Figure V-7. Electrical layout.

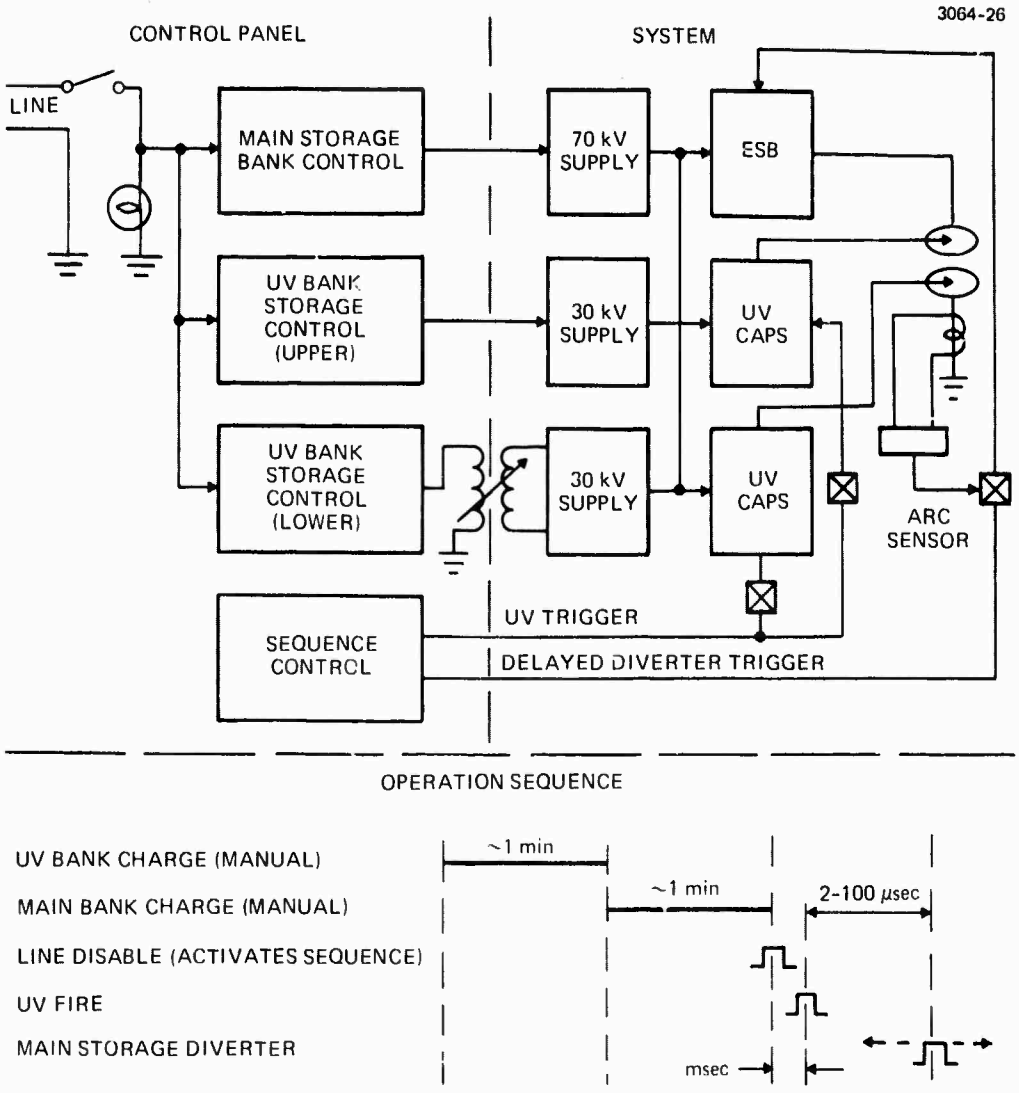

Figure 8. Operation diagram.

C. Arc Sensor Circuit

In this section the arc sensor circuit required to discharge the large energy storage bank on the LSD is described.

1. Objective

Three arc regimes for the UV-sustained laser exist. First, the well known post-arc phenomenon common to e-beam sustained lasers exists. This arc regime is due to the heated gas in the discharge center expanding out and lowering the density. Since the energy storage bank is essentially operating as a large dc battery, the voltage is still applied to the electrodes and hence the local E/N is higher leading to a post-arc (arc after the laser pulse is over). This arc regime does not affect the laser performance but presents a system operational problem (see below). Second, if an operational failure occurs with switching of the UV sources, a premature arc can be caused. Finally, attempts to load too much energy into the discharge regime can cause a glow-to-arc transition (GAT). All three regimes lead to arcs which cause serious damage to the fragile mesh screens that are wrapped around the Bruce electrodes. It must be remembered that since the energy storage bank is designed to provide essentially constant voltage throughout the pulse length it is of very large capacity. Approximately, only a 10% decrease in the energy of the bank occurs during a normal run. However, when an arc occurs the entire bank dumps with sufficient energy to damage the screens each time. Therefore, it is important to incorporate an arc-sensing circuit into the firing sequence to dump the bank before it can discharge into the screens.

The basic block diagram of the electrical layout involved is shown in Figure V-7. (The arc-sensing circuit will be described in detail later.) The crowbar is shown together with the CP50 Marx bank which fires the crowbar. The key problem of the arc-sensing circuit is to provide a signal to the CP50. This signal is generated by sensing an arc in the device using a small capacitor connected to the high voltage electrode. This capacitor is charged when the bank is normally charged. If an arc occurs during a run, the voltage immediately drops on the

electrode producing a small current through the capacitor proportional to dV/dt. This current is then sensed, processed to give the correct characteristics to fire the CP50 Marx bank, and then sent to the CP50 which fires the crowbar. This complete process takes about 500 nsec.

This is the basic arc sensing sequence. However, severe problems arise in this system because of the high EMI noise environment of the experiment. The primary problem is caused by the signals generated in the arc-sensing circuit by the UV circuits firing. This is a real signal, but represents an unwanted noise to the arc-sensing circuit. This type of problem required modular construction, light pipe connections, and blocking-out signals before successful operation was possible. A detailed description follows.

2. Fault-Detector Electronics

Two objectives of the fault-detection electronics are (1) it must detect current faults in the laser, and (2) it must provide a high voltage pulse to the laser supply crowbar circuitry to shut down the experiment and prevent mechanical damage to the laser. Because of the high noise environment associated with the experiment and the large currents flowing in the laser, the following guidelines were established for the electrical and mechanical construction of the electronics package:

- Unit must be battery operated
- All input signals must be optically coupled
- Mechanical construction must use standard EMI-RFI restraints. (The mechanical aspects will not be discussed in this report.)

3. Operation

The fault-detection electronics is comprised of a number of different independent sections. By following the signal timing diagram (Figure V-9) and referring to the system block diagram (Figure V-10) the unit can be explained as follows.

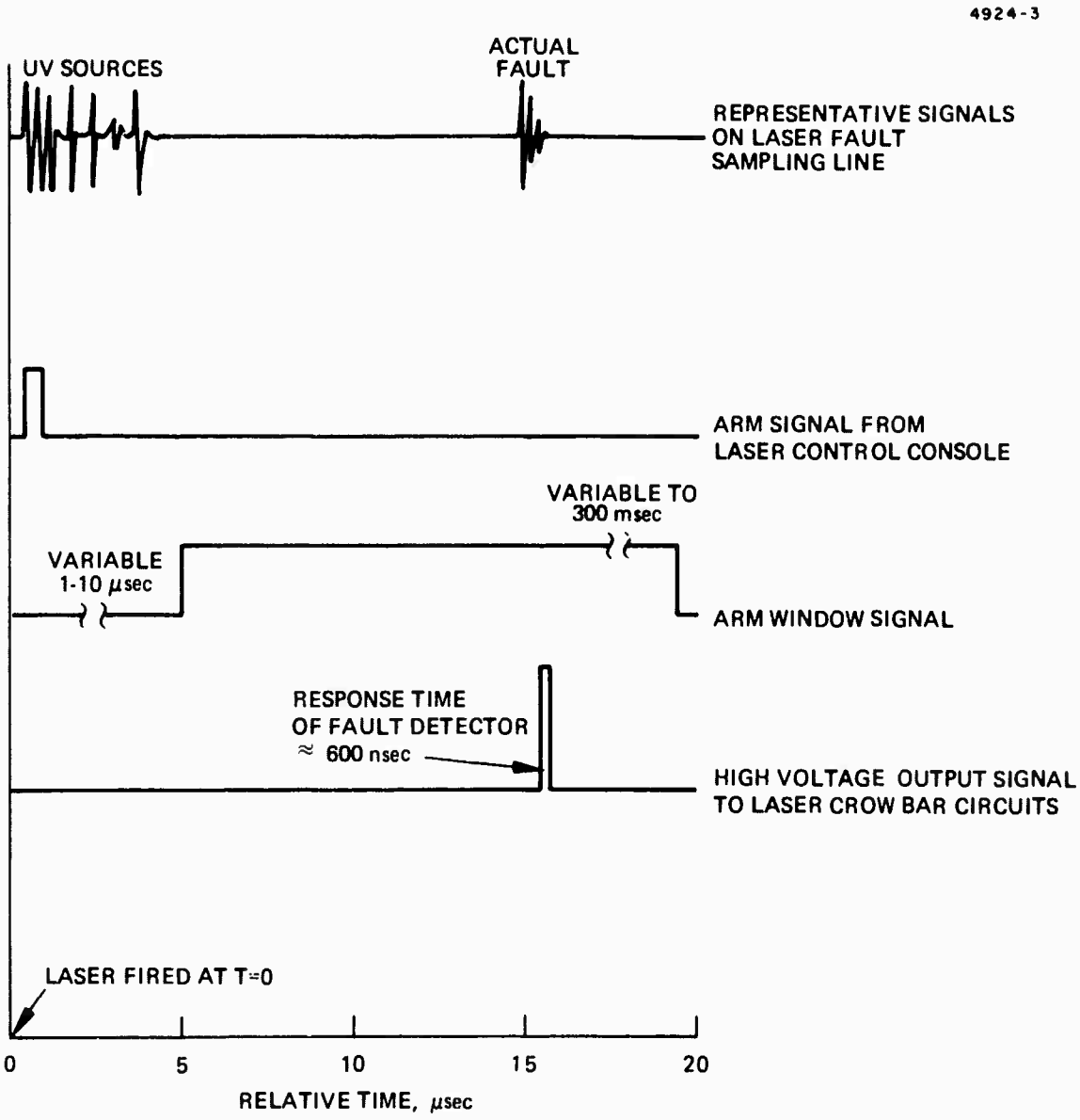

Figure V-9. Timing diagram of fault detector signals.

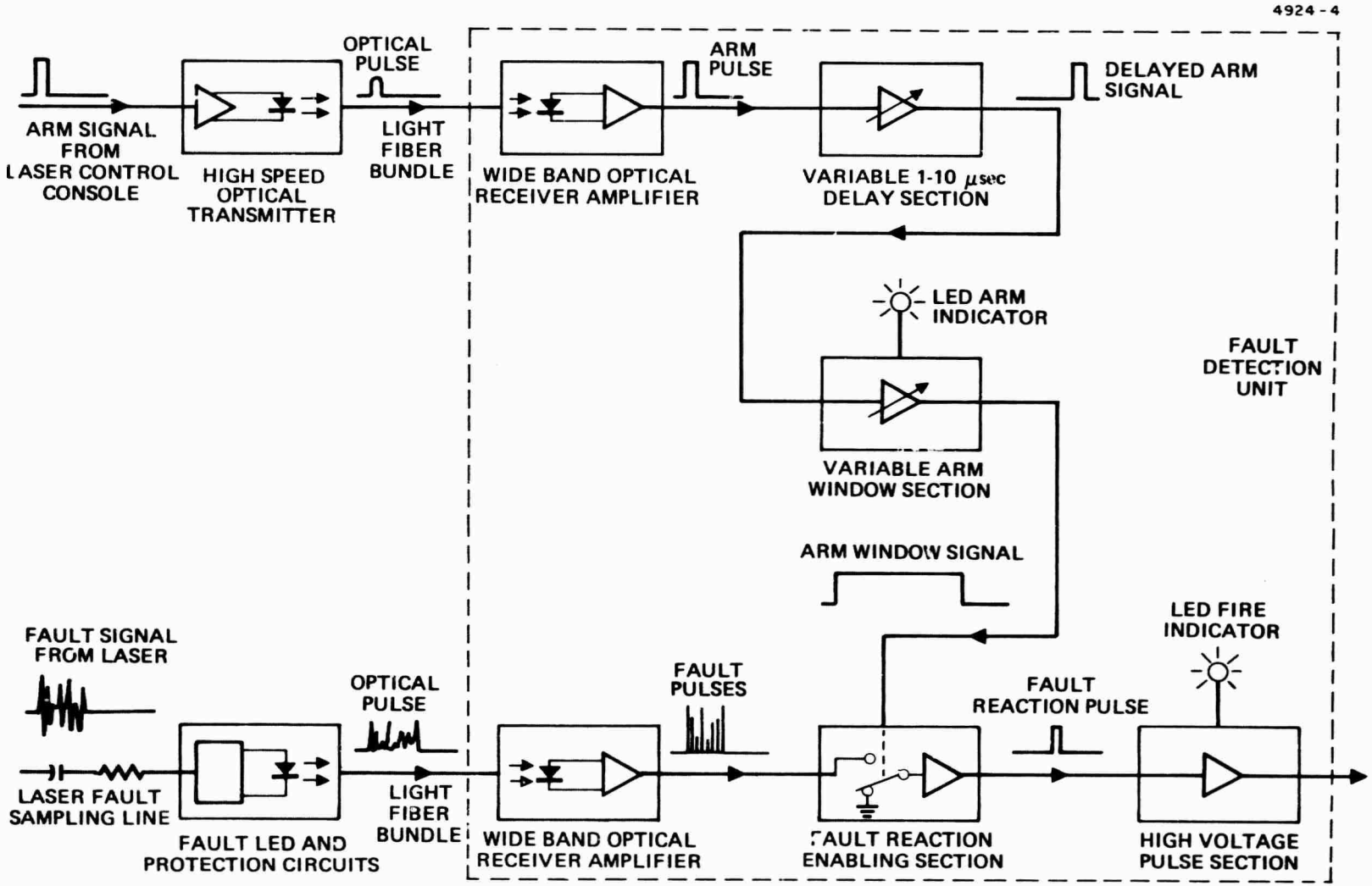

Figure V-10. Fault detector block diagram.

There are two signal inputs to the unit. One is from the laser control console and is designated "Arm Signal"; the other is from the laser fault sampling line (see Figure V-10)and is designated "Fault Signal." When the laser is fired an arm signal, coincident with the fire signal, is sent through an optical light coupler to the fault detector. Because the speed of operation of the fault detector is critical, this coupler uses a very fast SCR and an LED (typically 10 ns) for the transmitter and a silicon photodetector coupled to an FET input wide band amplifier for the receiver. This configuration yields a fast signal response time and very high electrical noise isolation between the experiment and the fault detector.

As seen in Figure V-9, at the same time the arm pulse is sent, signals are appearing on the fault-detection sampling line. These signals are identical, in both shape and amplitude, with a real fault signal. These, however, are not fault signals but are signals generated when the UV sources are fired.

With this in mind, the arm signal out of the wide band amplifier is fed to the variable delay section. Here the arm signal can be delayed for 1 to 10 μs, and the amount of delay is controlled by the laser operator. The proper delay setting is just after the noise generated by the UV sources has decayed (~3 to 5 μs).

Once delayed, the arm signal is fed to the arm window section. Here the pulse is used to generate a time window that is controllable by the operator. Once this window is generated the fault detector will not only detect faults in the laser but will react to them as well. When the arm window is generated, a panel-mounted LED is lit to indicate to the operator that the unit is armed.

The fault signals to be detected originate in the fault detection sampling line, where the key component of the fault detector is. It is simply a high speed, high current LED with some associated protection circuitry. By using an LED as the signal source we again have high electrical noise isolation plus fast response time and good signal sensitivity. The optical fault signal is fed through 30 ft of low-loss optical fiber to the fault detector where it is received and amplified by an amplifier identical to the arm pulse receiver.

When the arm window is present and a fault signal is received it is amplified and fed to the high voltage pulse section. It is used to ignite a gas filled discharge tube connected to a high voltage supply. This generates a high voltage pulse which is transformer coupled to the laser supply crowbar circuitry thus ending the laser current. A panel-mounted LED is provided to inform the operator that a fault was detected and a crowbar output signal was sent.

The response time of the fault detection unit is ~500 nsec. Although this figure could be reduced by 50%, the noise immunity of the electronics would be greatly reduced and unreliable operation would result.

A detailed circuit diagram is shown in Figure V-11.

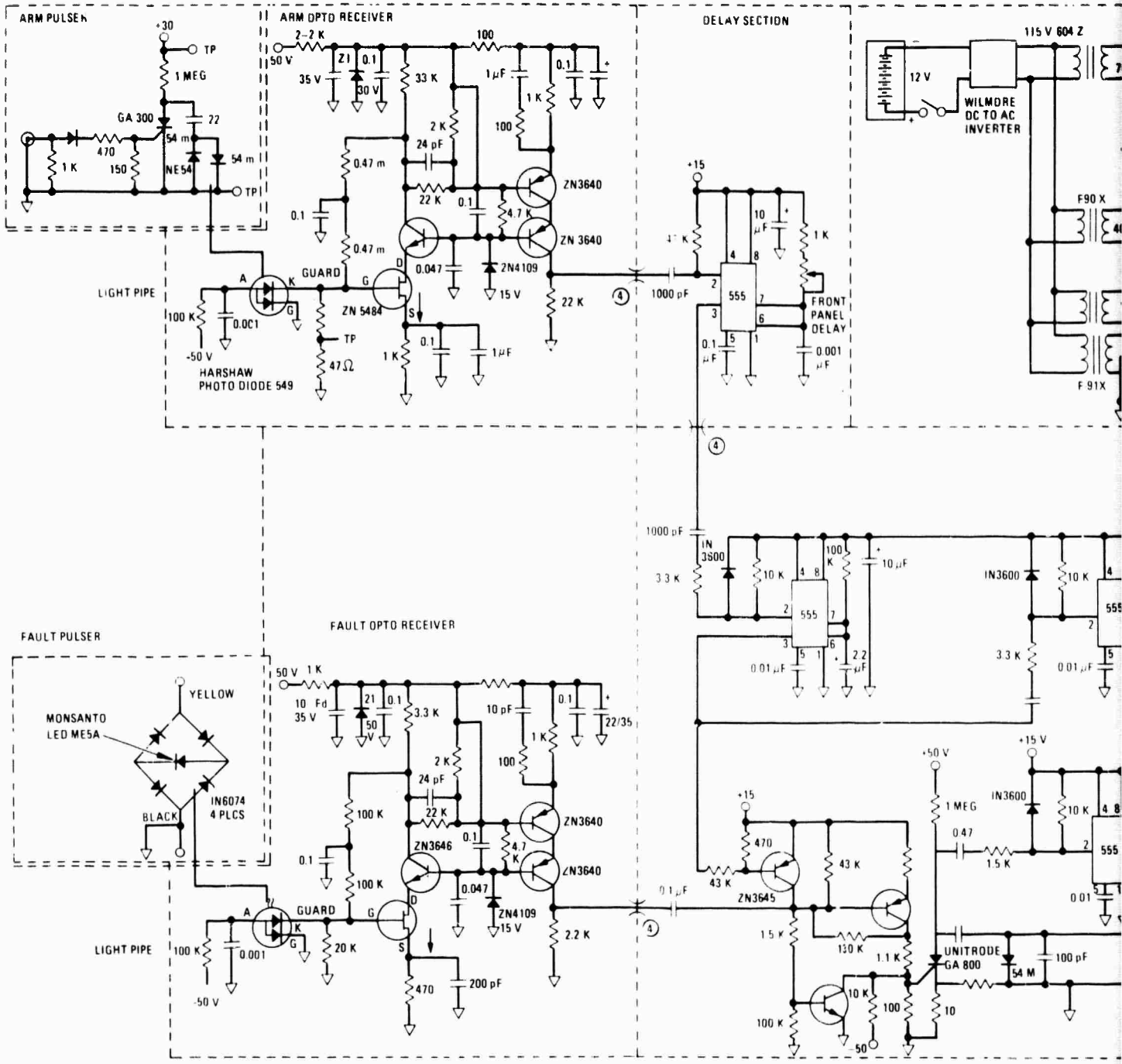

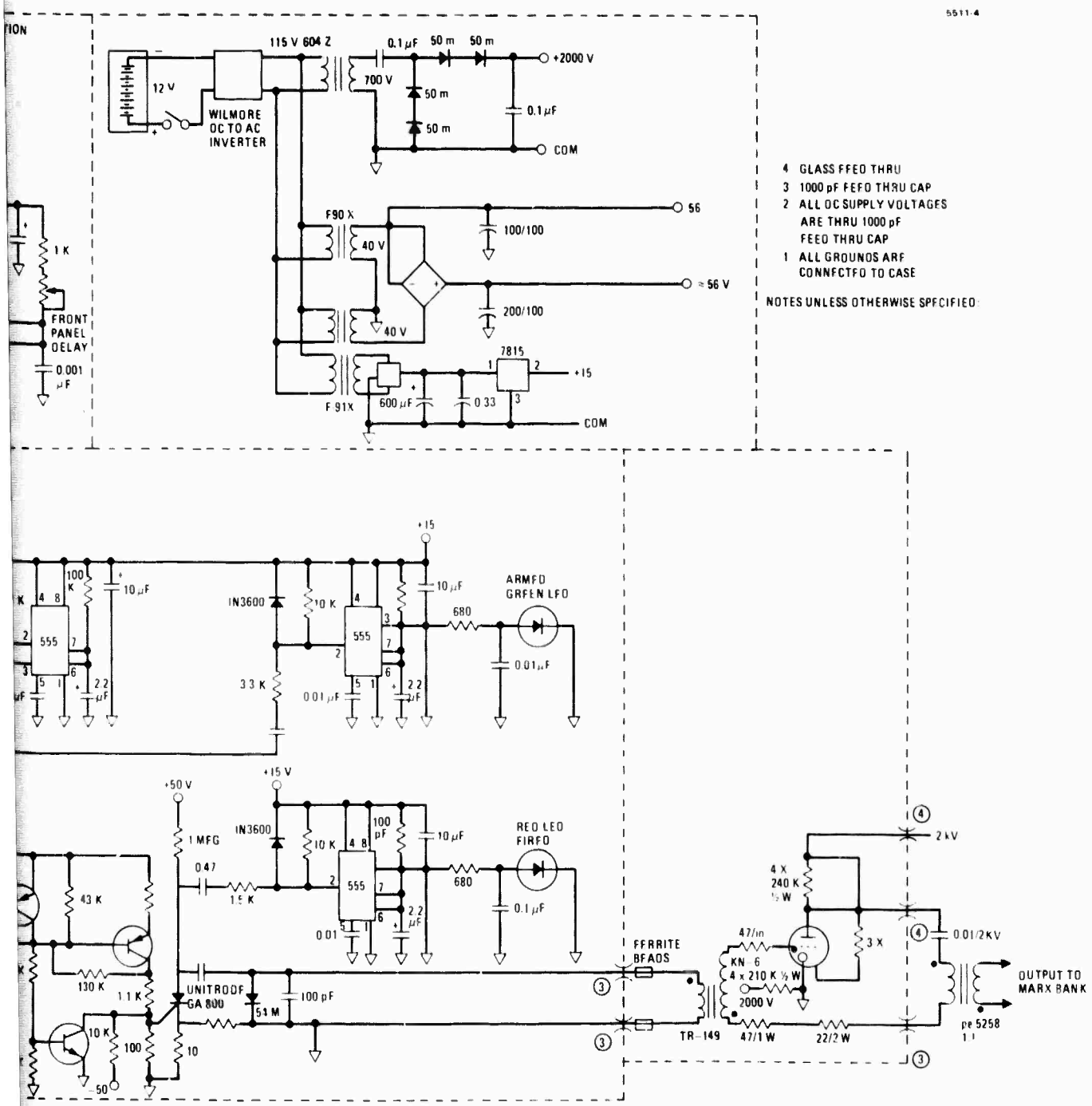

Figure V-11. Arc sensor circuit.

VI. LARGE SCALE DEVICE EXPERIMENTS

In this section the measurements performed on the large scale device are described. These measurements included the following: input energy loading; laser output energy incorporating both stable hole-coupled optics and unstable resonator optics; spatially and temporally resolved small signal gain; and double exposure pulsed holographic interferograms for media quality.

Based on these measurements a complete understanding of the operation of a large scale UV-sustained laser has been achieved. A significant power extraction in excess of 400 J has been demonstrated. This represents an energy density of ~35 J/l-atm in agreement with model predictions. The overall efficiency of the system (including the UV source) is about 12%* competitive with e-beam systems. Media quality and small signal gain spatial measurements indicate that a near diffraction limited beam will be achieved in the far field.

In addition, the output energy measurements are consistent with the scaling model to be discussed in Section VII. Thus, the guidelines for building multikilojoule UV sustained lasers are established.

All the results to be described, with the exception of the unstable resonator extraction measurements, are confined to a 6 cm gap height configuration.

A. Input Energy Density

Input energy density measurements were made for several mixtures and the results are given in Figure VI-1. The energy input was calculated by integrating the area under the sustainer current

*The efficiency in this device was low because of limited gain: scaling the present device in length (along the optical axis) would increase the efficiency to ~20%.

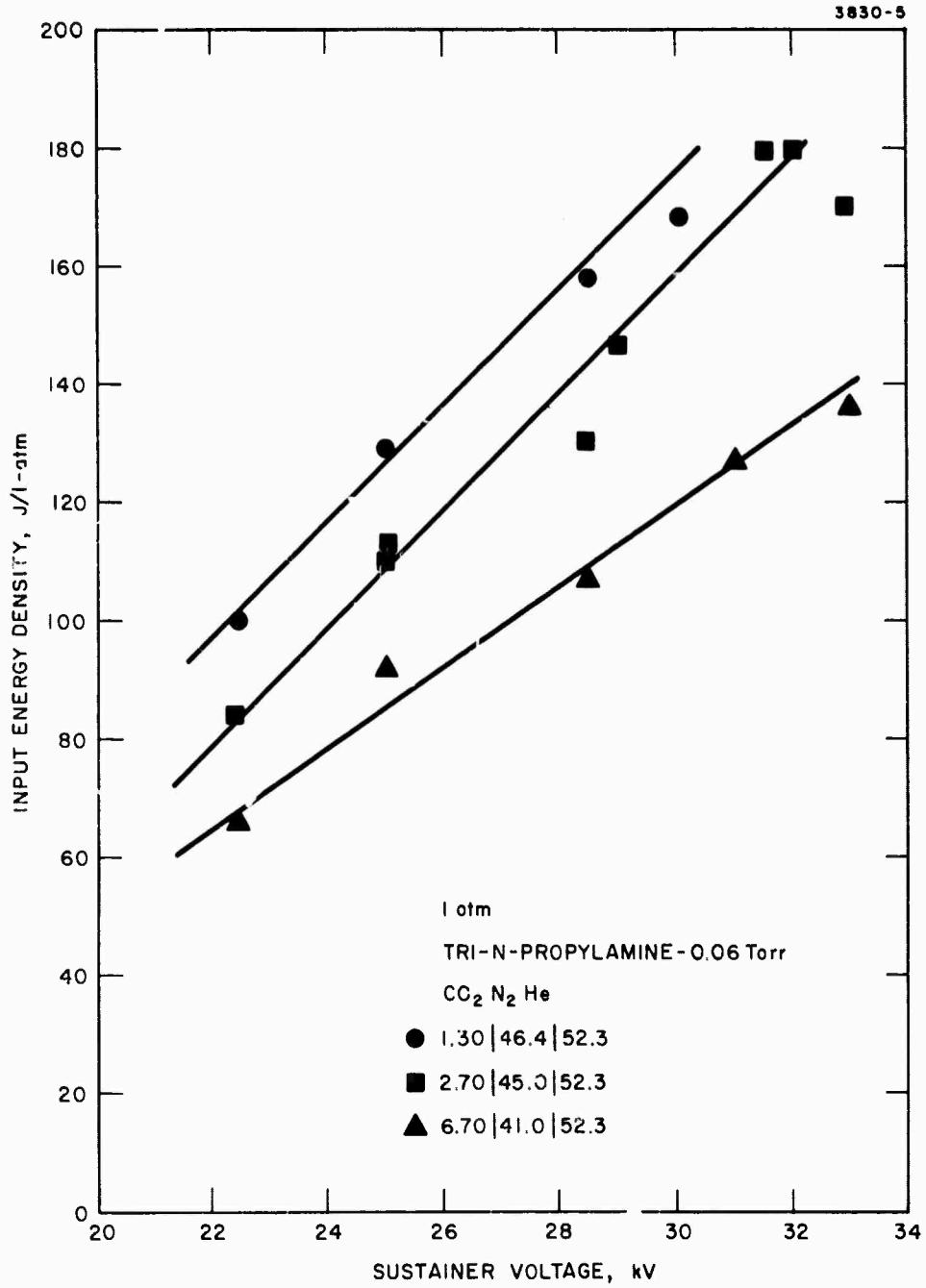

Figure VI-1. Input energy density as a function of sustainer voltage.

waveform (see Figure VI-11(a) for a typical pulse shape) and then multiplying by an adjusted value of the dc bias voltage. The adjustment was made to account for the voltage droop on the capacitor bank that occurs during a shot. This adjustment was typically 10 to 15%. To determine the discharge volume, Teflon masks were inserted in the electrode gap region (see Figure VI-2). These masks confine the discharge in the width dimensions with some spillage of the discharge outside the end regions allowed. Thus the energy density calculated using this volume can be somewhat higher (5 to 15%) than achieved. We see from these results that energy densities up to 180 J/l-atm have been achieved. These results are comparable to those achieved on the medium size device.

B. Small Signal Gain

The small signal gain was measured for various mixtures, sustainer voltages, and spatial position. Figure VI-3 gives the magnitude of the gain as a function of sustained voltage for the mixture shown to give maximum laser output (see Figure VI-9). We see that the maximum gain for the UV-sustained laser is about 0.85%/cm, which is consistent with that expected for the low CO_2 concentration mixtures employed. Also shown on this figure are calculated values for the gain. These values were determined using the HRL four-temperature CO_2-N_2-He kinetic model with the crucial electron pumping rates determined from the HRL electron Boltzmann equation code. The purpose for making such comparisons is to establish that consistent predictions of the performance of the large-scale device can be made. The program can then be used as an aid in determining the expected performance of other such devices and in particular can determine the optimum output coupling for a UV sustained laser. This information was used to design the unstable resonator built for optimum full scale energy extraction studies.

Typical gain waveforms are shown in Figure VI-4. The trace shown in Figure VI-4(a) was obtained at the center of the discharge and Figure VI-4(b) was obtained at a point 5 mm from the cathode (see Figure VI-2 for orientation). Both traces indicate the arrival of the acoustic

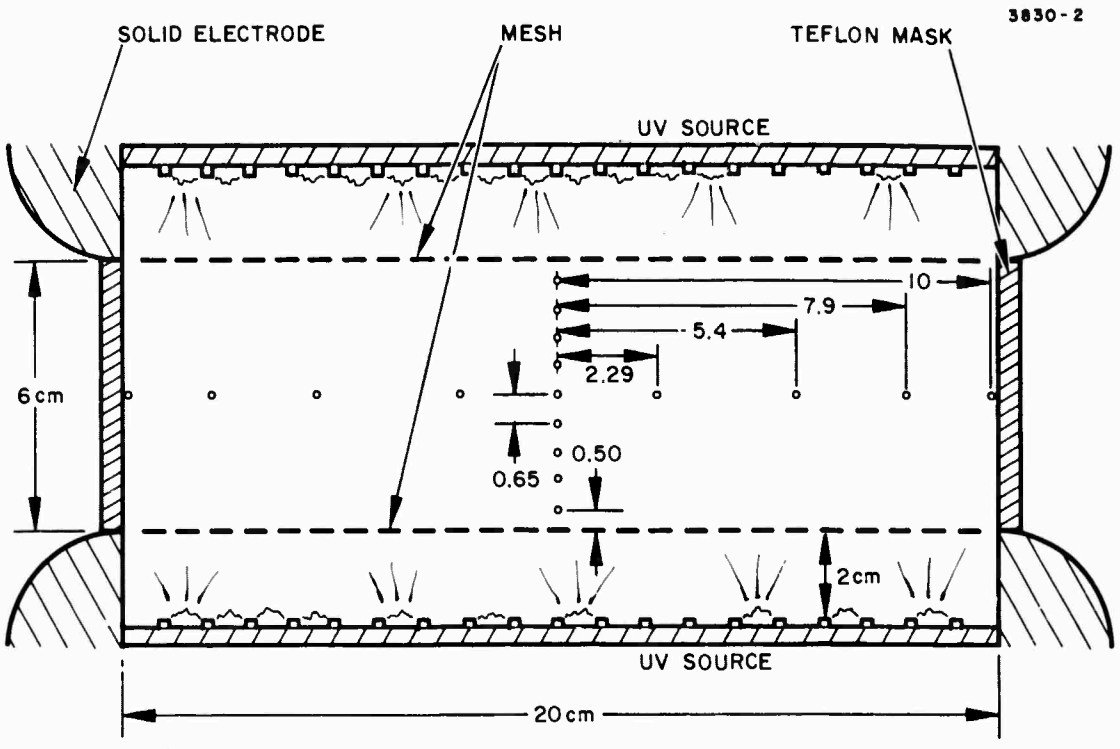

Figure VI-2. Continuous wave probe laser positions.

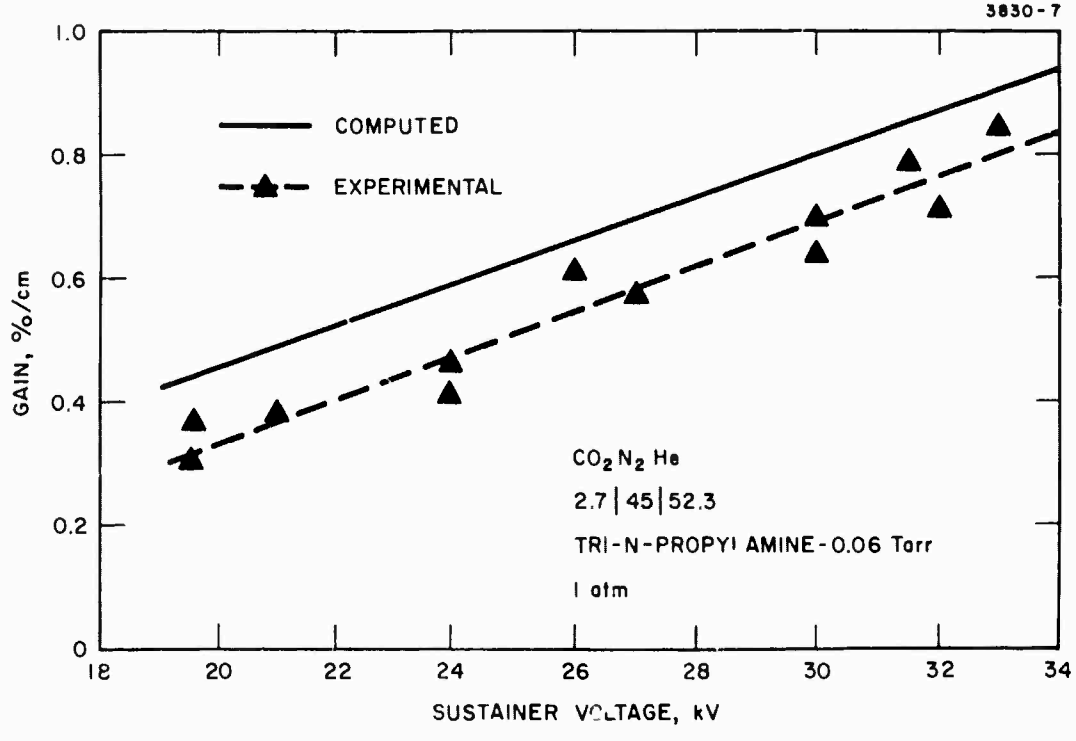

Figure VI-3. Small signal gain as a function of sustainer voltage.

CO_2N_2He 3830-4
2.7|45|52.3
TRI-N-PROPYLAMINE - 0.06 Torr
1otm V_{SUS}=29kV

CENTER OF DISCHARGE

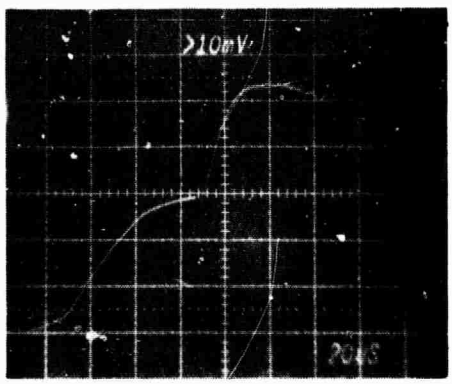

a

5mm FROM CATHODE

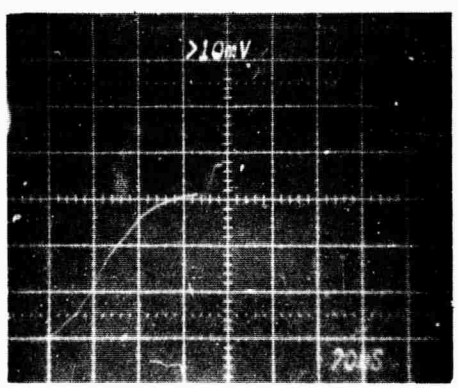

b

Figure VI-4. Small signal gain waveforms.

disturbance from the UV source. At the center of the discharge (Figure VI-4(a)) the disturbance appearing emanates from both UV sources and arrives at a time later than the disturbance emanating from the cathode alone, shown in Figure VI-4(b). An additional effect shown in Figure VI-4(b) is the large modulation of the gain near the cathode. This is similar to the result obtained previously and hence is not surprising (see explanation below). The predicted gain waveform was calculated for a specific experimental case (similar to that shown in Figure VI-4(a)) with the comparison given in Figure VI-5. We see that the agreement is excellent.

Spatially resolved gain measurements were performed with both the electrode gap spacing and the discharge width traversed by the measurements. The cw probe laser positions used are given in Figure VI-2. The gain distribution across the 6 cm electrode gap dimension is shown in Figure VI-6. The magnitude of the gain is seen to be uniform to within ±10% across the entire gap. These data were taken with both sources operating which is the standard mode for obtaining data. The important aspect of these data is that contrary to the results obtained previously (see Figure IV-11) where only one source was employed, no large increase in gain was obtained as approach to the cathode is made. In the previous case it was speculated that the large increase was due in part to UV-induced photoelectron emission from the solid cathode (the UV source was located behind a mesh anode). The additional electrons then causing localized avalanching near the cathode. An additional contributing factor as explained previously (see discussion following Figure IV-11) is the increased field strength in the region of low electron density near the cathode. The increased field strength then being sufficient to produce avalanching. In this case it is assumed that the electron density is established entirely by the UV source and subsequent photoionization of the seed gas (not by photoelectrons). The flux level, hence electron density, falls off when moving away from the anode toward the cathode. In order to maintain constant current across the gap, the field strength must then increase proportionally to this decrease in electron density. In the present situation this latter effect is absent entirely because there is a UV source located behind the

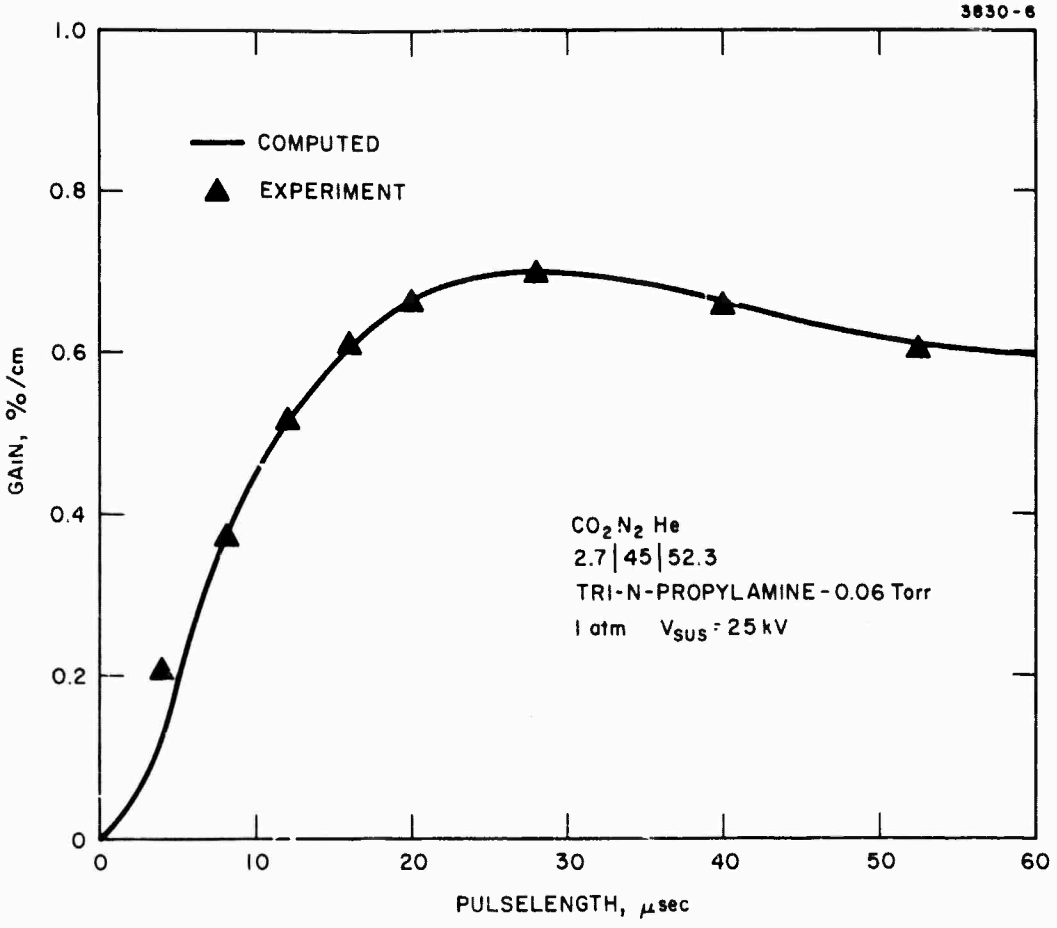

Figure VI-5. Small signal gain waveform, comparison of theory and experiment.

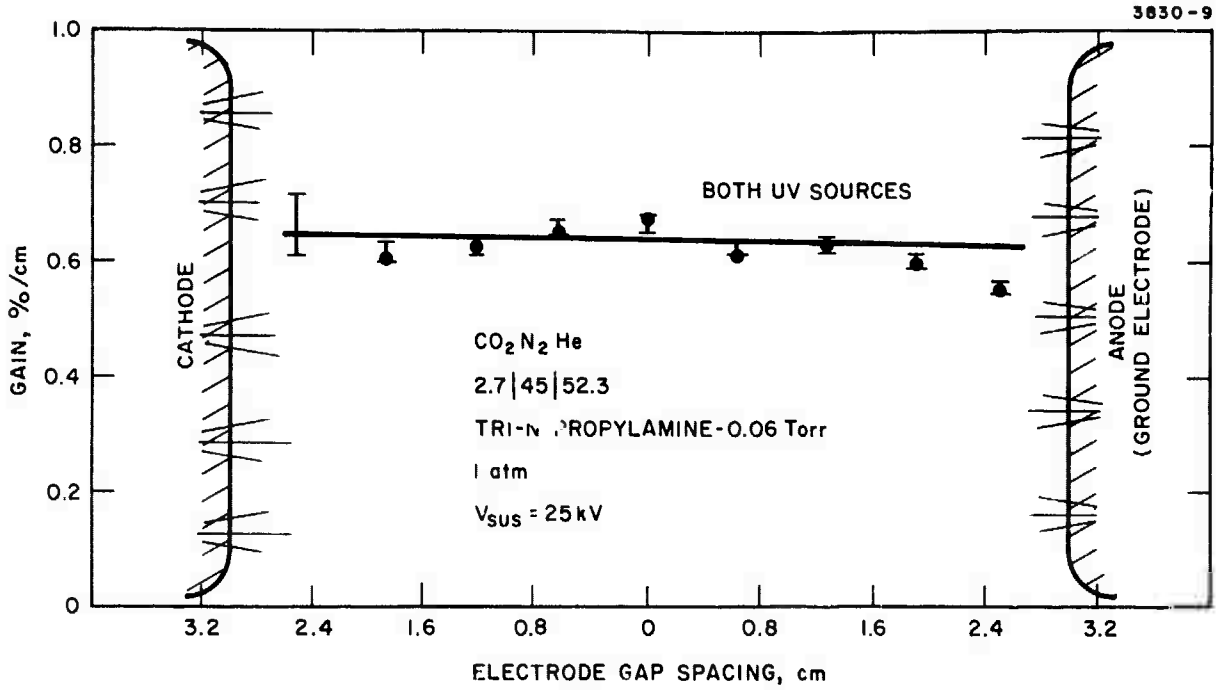

Figure VI-6. Small signal gain as a function of electrode gap spacing.

cathode also contributing a large electron density in that region. Consequently, the field strength does not increase and no avalanching is expected. Furthermore, since a mesh is used for the cathode (50% transmitting) the photoemission is reduced by a factor of two and its effect is greatly reduced. In spite of this, however, some avalanching is apparently occurring as evidenced by the waveform shown in Figure VI-4(b) and by the large error bar shown in Figure VI-6 for the data taken near the cathode. The overall uniformity is good, however, and should present no limitation to beam quality.

The gain distribution across the 20 cm discharge width dimension is shown in Figure VI-7. We find that the gain falls off uniformly toward either end with a maximum of 30% observed. The active UV source region spans the center 16 cm and hence the falloff obtained is to be expected.

C. Energy Extraction Results – Stable Cavity

Extensive energy extraction measurements have been obtained using a hole coupled stable cavity arrangement. The optical arrangement used for the stable cavity measurements is shown in Figure VI-8.

The output energy obtained with this optical arrangement for several gas mixtures as a function of sustainer voltage is shown in Figure VI-9. We find a maximum energy of 200 J for the particular mixture of 0.06 Torr tri-n-propylamine and a $CO_2/N_2/He$ mixture ratio of 2.7/45/52.3 (total pressure 1 atm). The near-field burn pattern for this case is shown in Figure VI-10. The burn pattern covers roughly a 6 x 13 cm^2 area. This represents the largest extraction area possible, taking into account the limiting apertures in the present optical arrangement, i.e., the right-hand side of the pattern is clipped by the external beam splitter required for energy measurements and the left-hand side by the 13 cm diameter hole coupled output mirror. The 6 cm dimension is apertured by the electrodes.

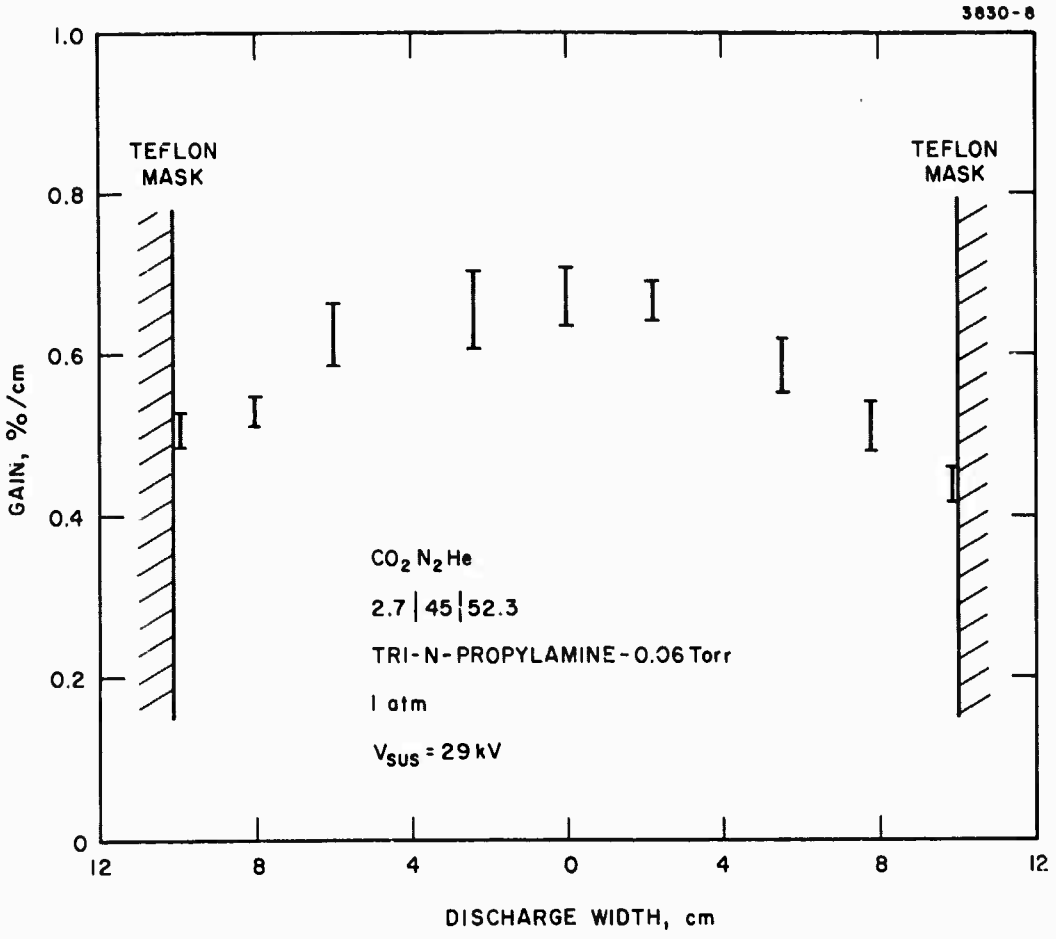

Figure VI-7. Small signal gain as a function of discharge width.

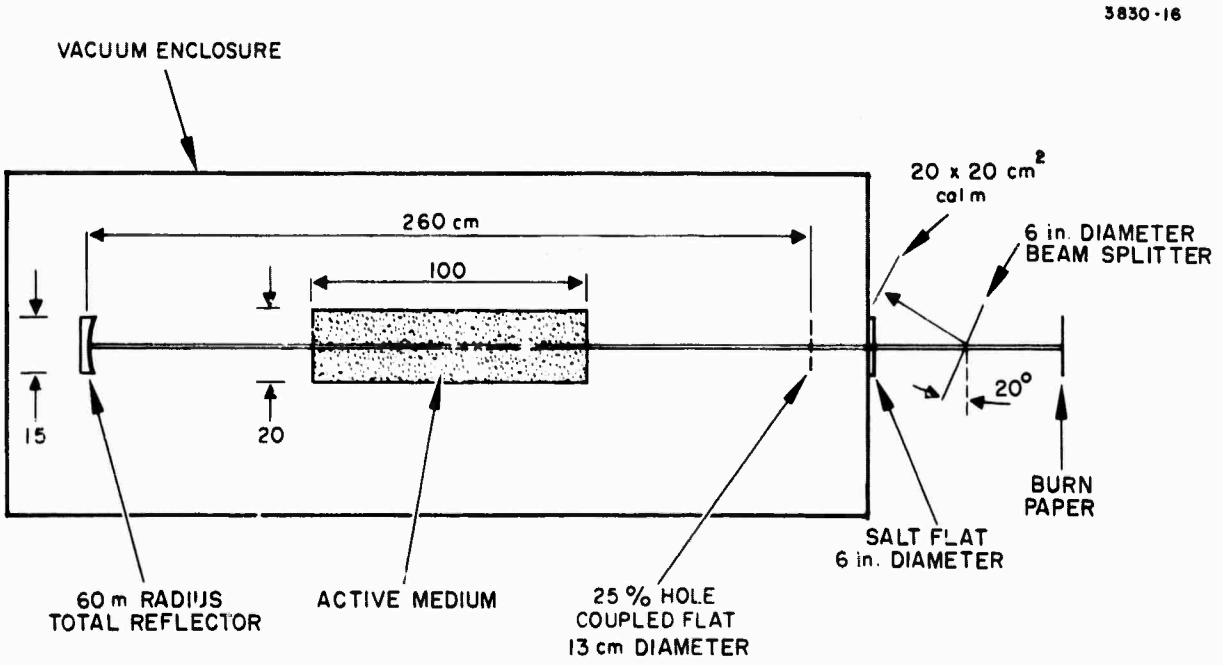

Figure VI-8. Optical arrangement for present energy extraction measurements.

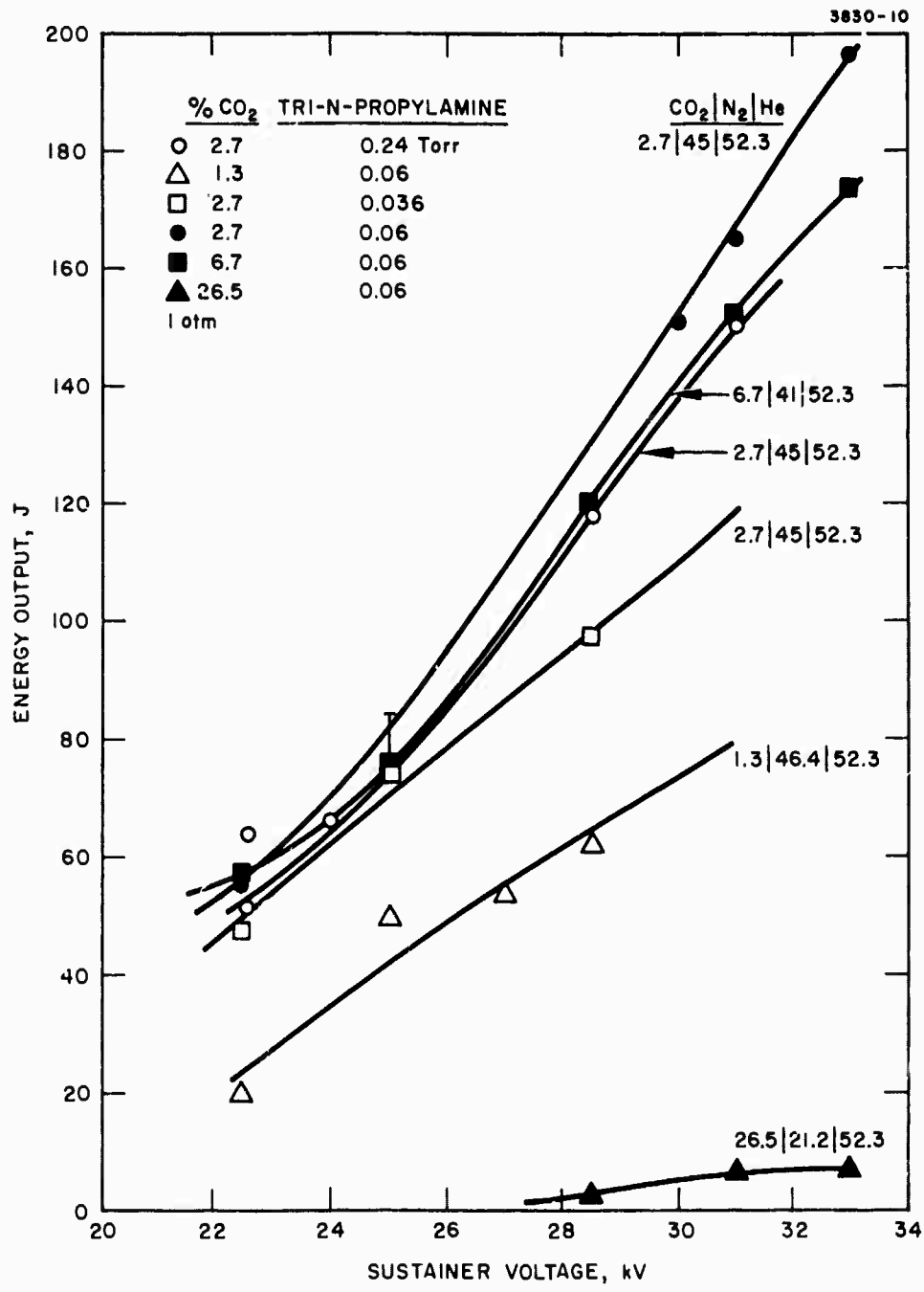

Figure VI-9. Laser output as a function of sustainer voltage.

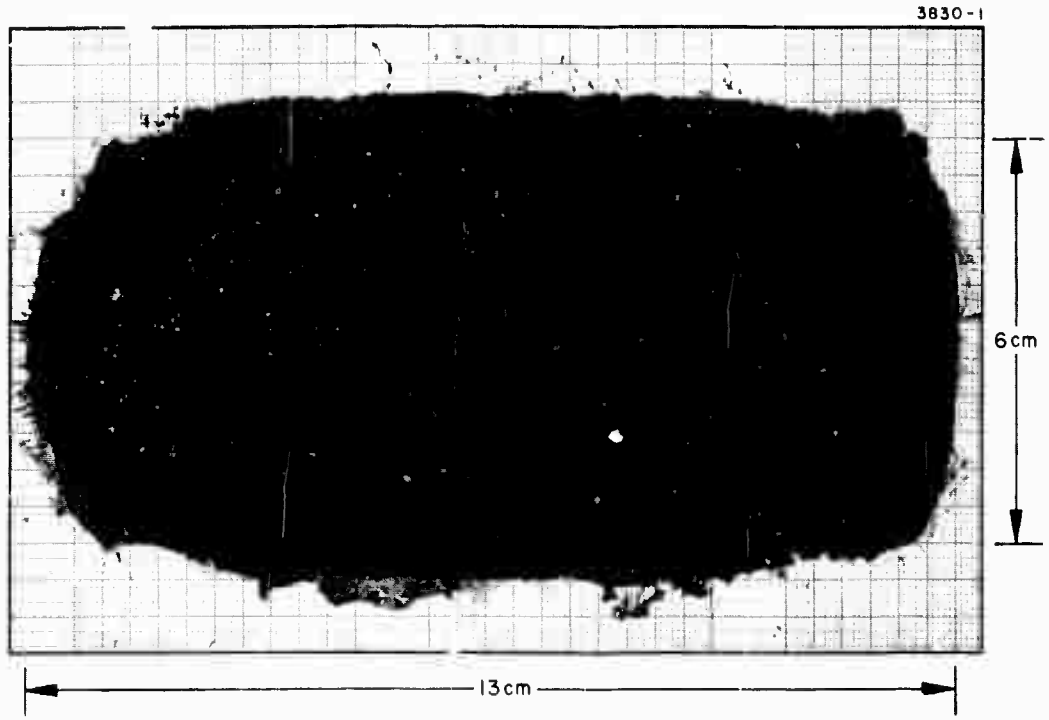

Figure VI-10. Near-field burn pattern.

Returning to Figure VI-9, we find that increasing the CO_2 concentration by a factor of 2.5 times only resulted in a 20% falloff in output energy. A similar falloff was observed when the tri-n-propylamine concentration was increased as much as four times the optimum value.

A typical laser pulse shape together with a sustainer current and UV current pulse shape is shown in Figure VI-11. We see that the laser output has a pulse length of about 35 μs and turns off simultaneously with the sustainer current pulse. It is also seen that the laser output amplitude remains nearly constant in time for a period longer than the sustainer current. This is caused by the large concentration of N_2 in the mixture which is transferring its stored energy to the CO_2 during the pulse duration. Calculation of the laser pulse shape was made using the kinetic code. The results of such a calculation, for a sustainer voltage of 28.5 kV, is given, together with that obtained experimentally, in Figure VI-12. We see that the agreement is very good, particularly in determining the turn-on time, turn-off time, and peak power density.

Having established the mode volume based on the burn pattern obtained, the output energy density can be determined. Using the best experimental results, the output energy density as a function of sustainer voltage, is given in Figure VI-13. We see that the maximum achieved is 28 J/l-atm. Using the input energy density for this case the laser efficiency is 15%. This result is below that achieved previously on the medium size device (see Figure IV-15) and below that achieved with the unstable resonator (see below). We believe the high loss in the hole coupled output mirror due to scattering from the holes is the major cause for these lower results. It is of interest to determine what level of loss is predicted for the system by the kinetic code which has now been established to be consistent with the measurements. In Figure VI-13 the calculated energy density for various losses of 2, 4, 6, and 8% per mirror is given. We see that the curve for the high loss case of 8% per mirror is in close agreement with that obtained experimentally. A further substantiation for this high loss comes from

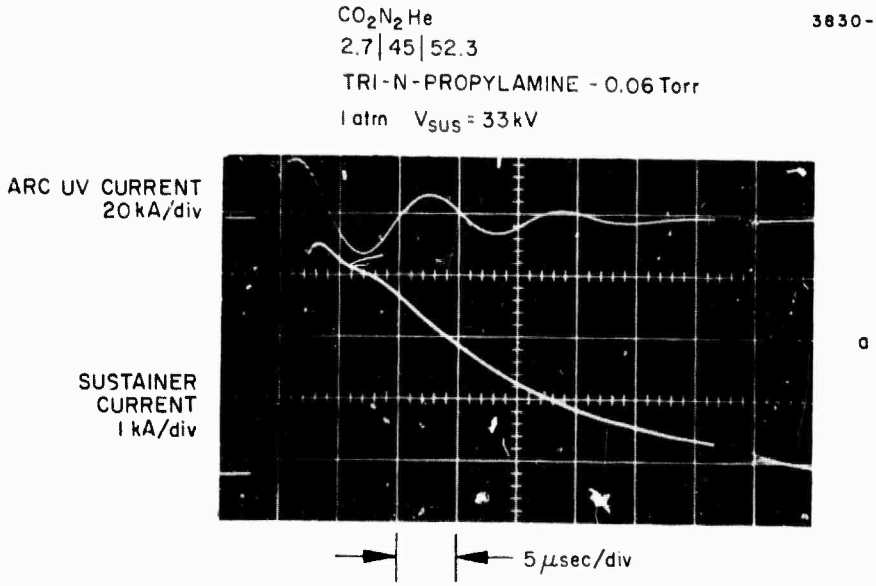

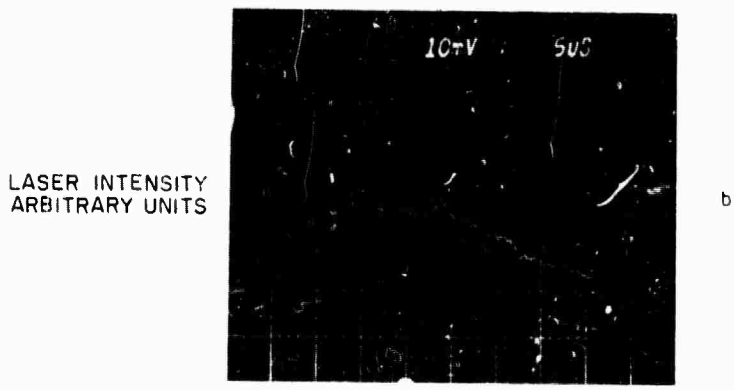

Figure VI-11. (a) Sustainer and UV arc current waveforms.
(b) Laser pulse shape.

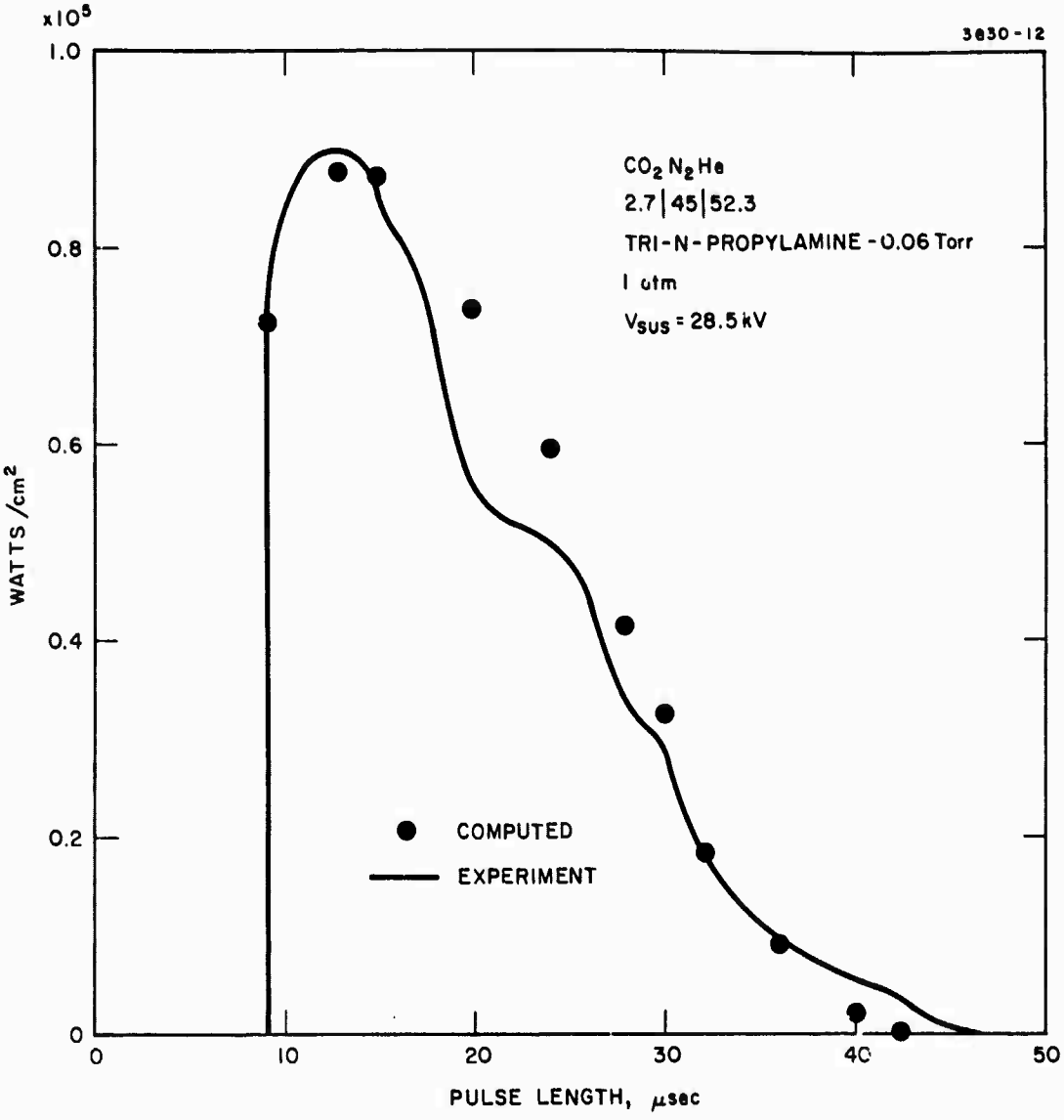

Figure VI-12. Laser pulse shape, comparison of theory and experiment.

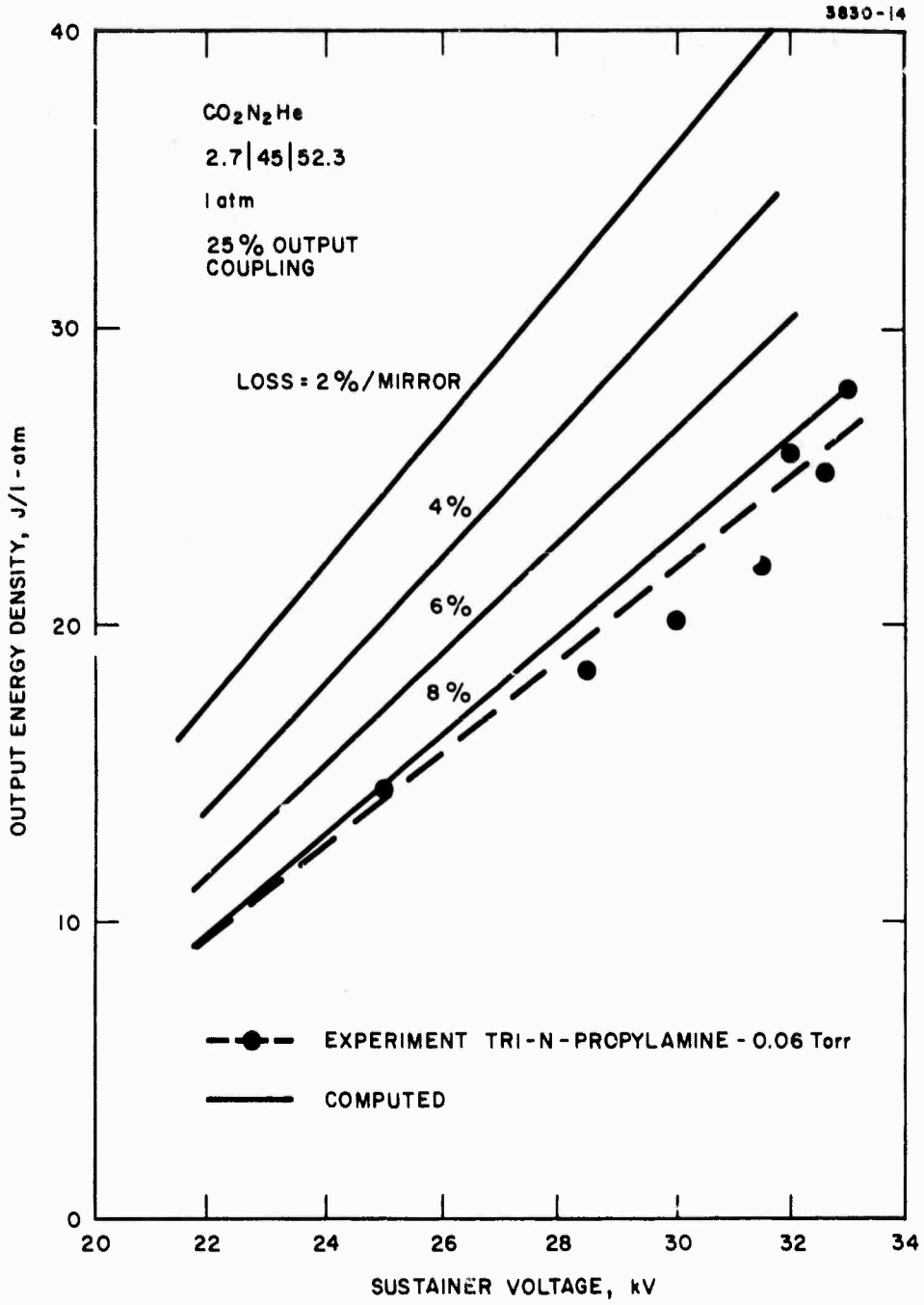

Figure VI-13. Output energy density as a function of sustainer voltage.

calculations of the laser turn-on time as a function of sustainer voltage. Such results are given in Figure VI-14 for a loss of 2% and 8% per mirror. It is clear that the experimental results, shown as the solid error bars, follow the 8% results closely and are distinctly different from the 2% case. One further comparison was the laser pulse shape discussed in Figure VI-12. Here the peak power density is a strong function of the losses. For the comparison given, the 8% per mirror value was used in the calculations.

D. Energy Extraction Results — Unstable Resonator

The unstable resonator employed is of rectangular dimensions. The electrode gap, fixed at either 6 or 8 cm, forms one aperture with the nominal discharge width of 20 cm forming the other. An output coupling of 30% is used. This coupling represented a reasonable compromise between having as low a coupling as possible for complete saturation of the medium and having a larger coupling for ease of alignment. The optical arrangement for these measurements is shown in Figure VI-15.

The demonstrated energy extraction at a 6 cm gap height is shown in Figure VI-16 as a function of sustainer voltage. A typical near burn field pattern is shown in Figure VI-17. The output energy is plotted as a function of sustainer voltage for the unstable resonator case (the previously obtained stable cavity results are also shown). It can be seen that approximately 370 J has been achieved at 34 kV. The increase in energy achieved with the unstable cavity is a consequence of the increased active volume size of the resonator. That is, the nominal discharge width is 20 cm but previously (stable cavity, see Figure VI-8) the optics limited the region of power extraction to 13 of the 20 cm. With the unstable resonator the full 20 cm is used to extract power.

In Figure VI-18 the demonstrated energy extraction at both 6 and 8 cm is presented as a function of the applied E/N. We see that for the 8 cm gap in excess of 400 J has been demonstrated. This output was achieved at an E/N $\sim 1.7 \times 10^{-16}$ V cm^2. This corresponds to ~130 J/l input energy density. For the 6 cm case a higher E/N and input energy

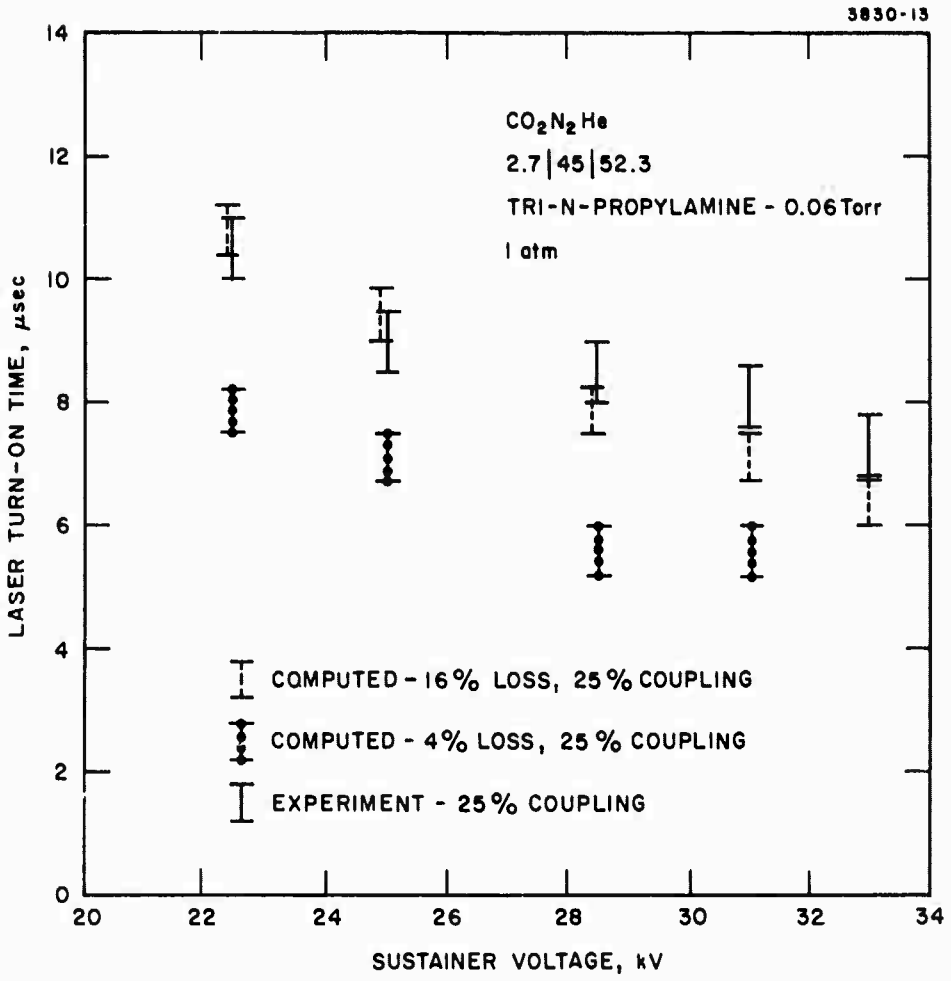

Figure VI-14. Laser turn-on time as a function of sustainer voltage for 4 and 16% loss.

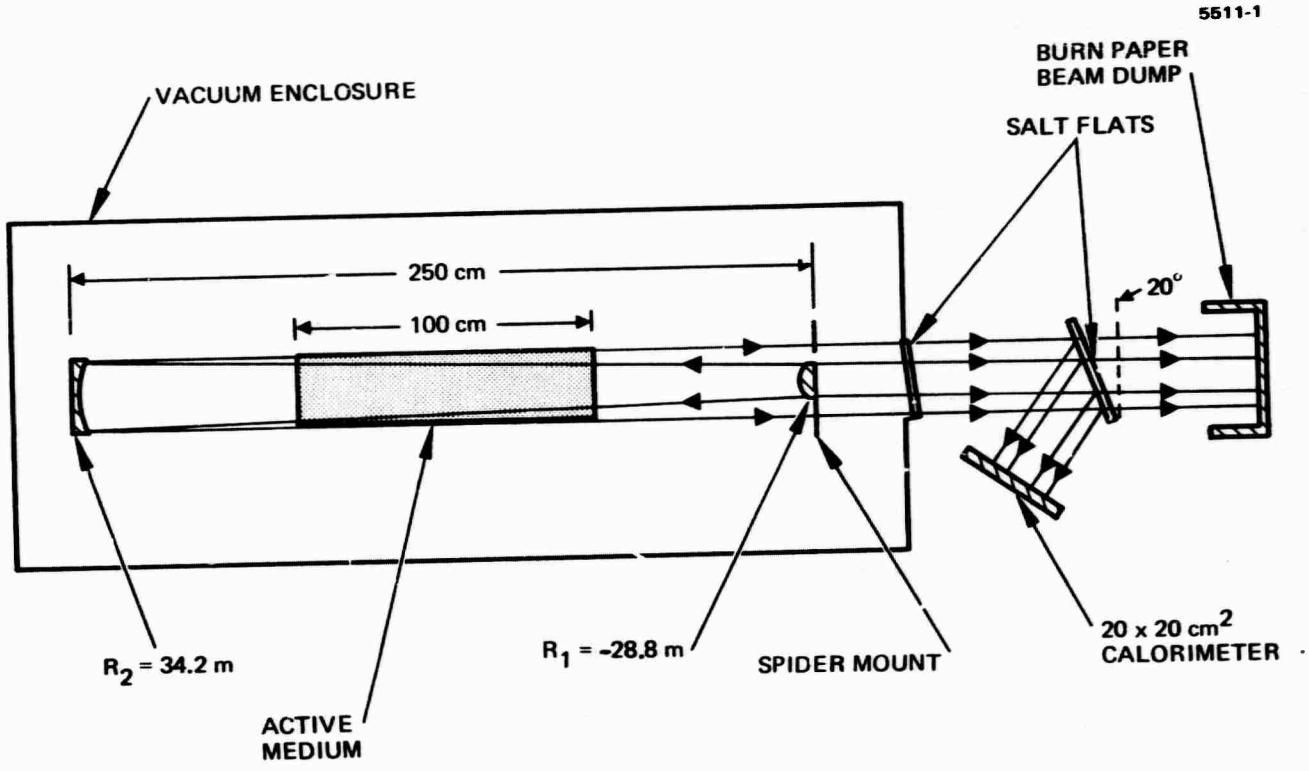

Figure VI-15. Optical arrangement for unstable resonator extraction measurements.

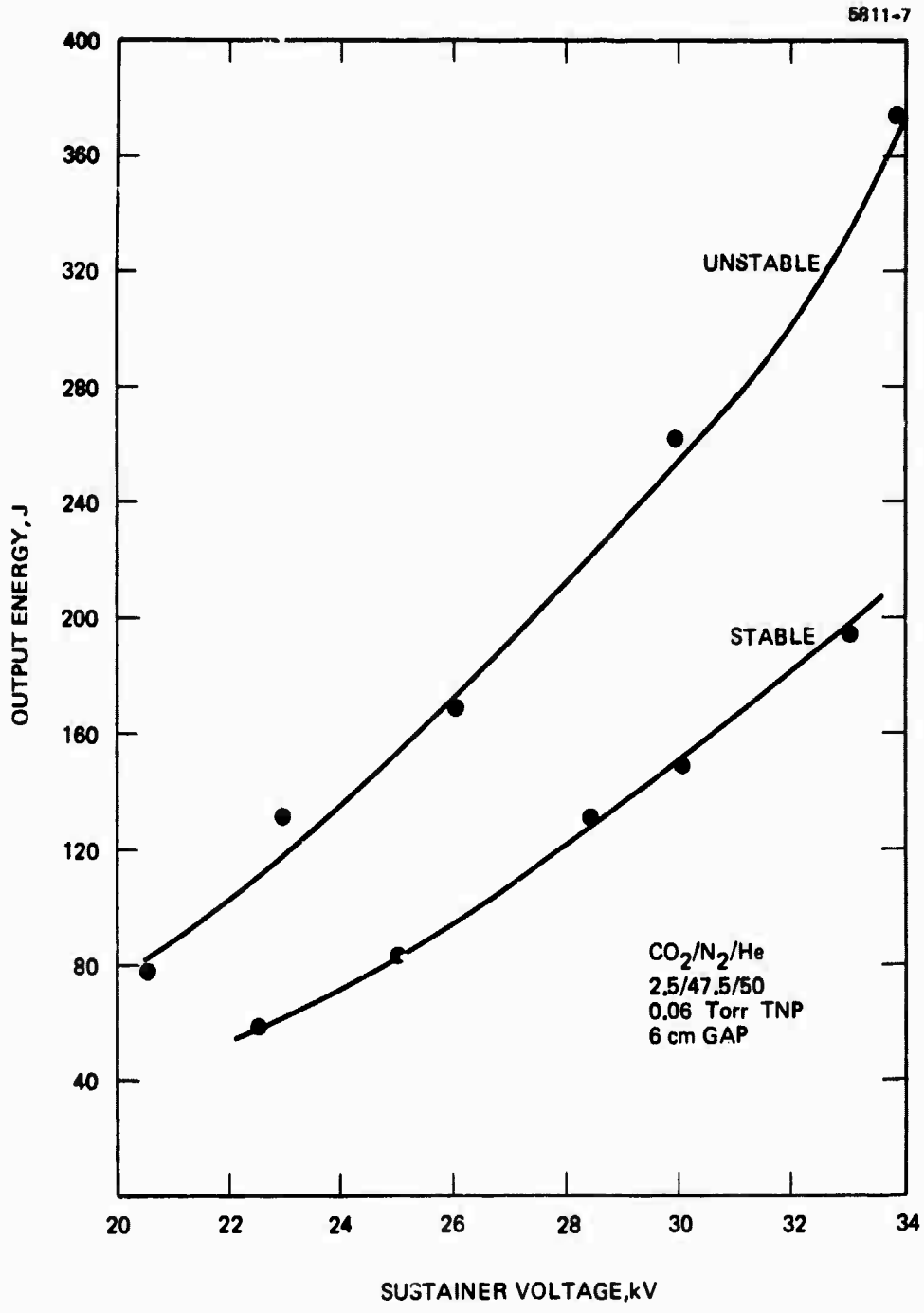

Figure VI-16. Output energy as a function of sustainer voltage for stable and unstable resonator.

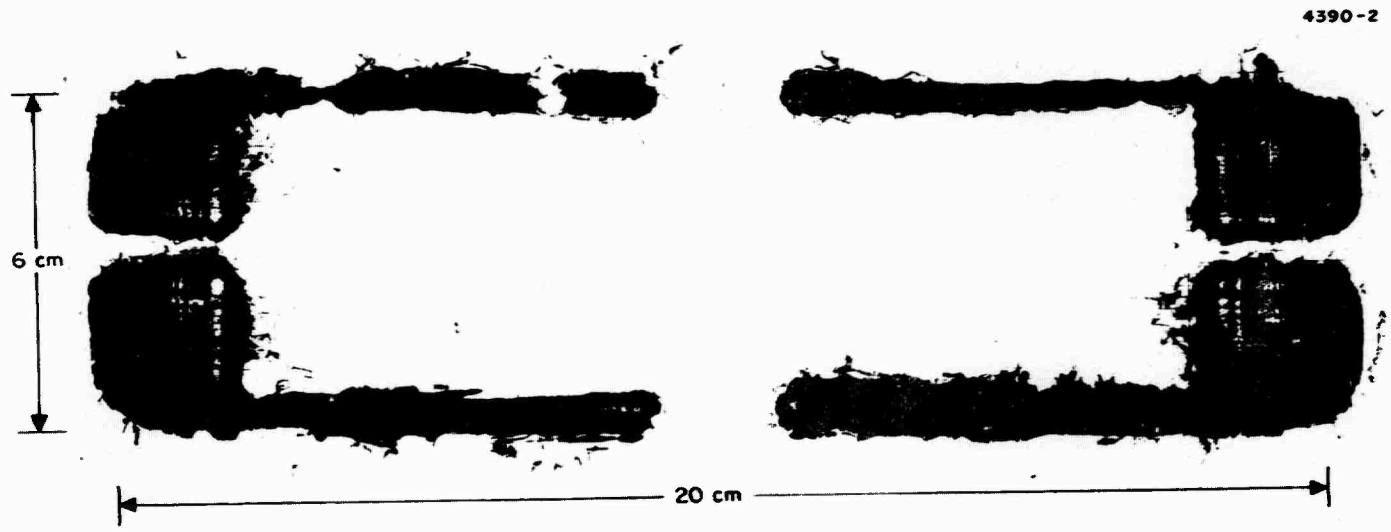

Figure VI-17. Near-field burn pattern.

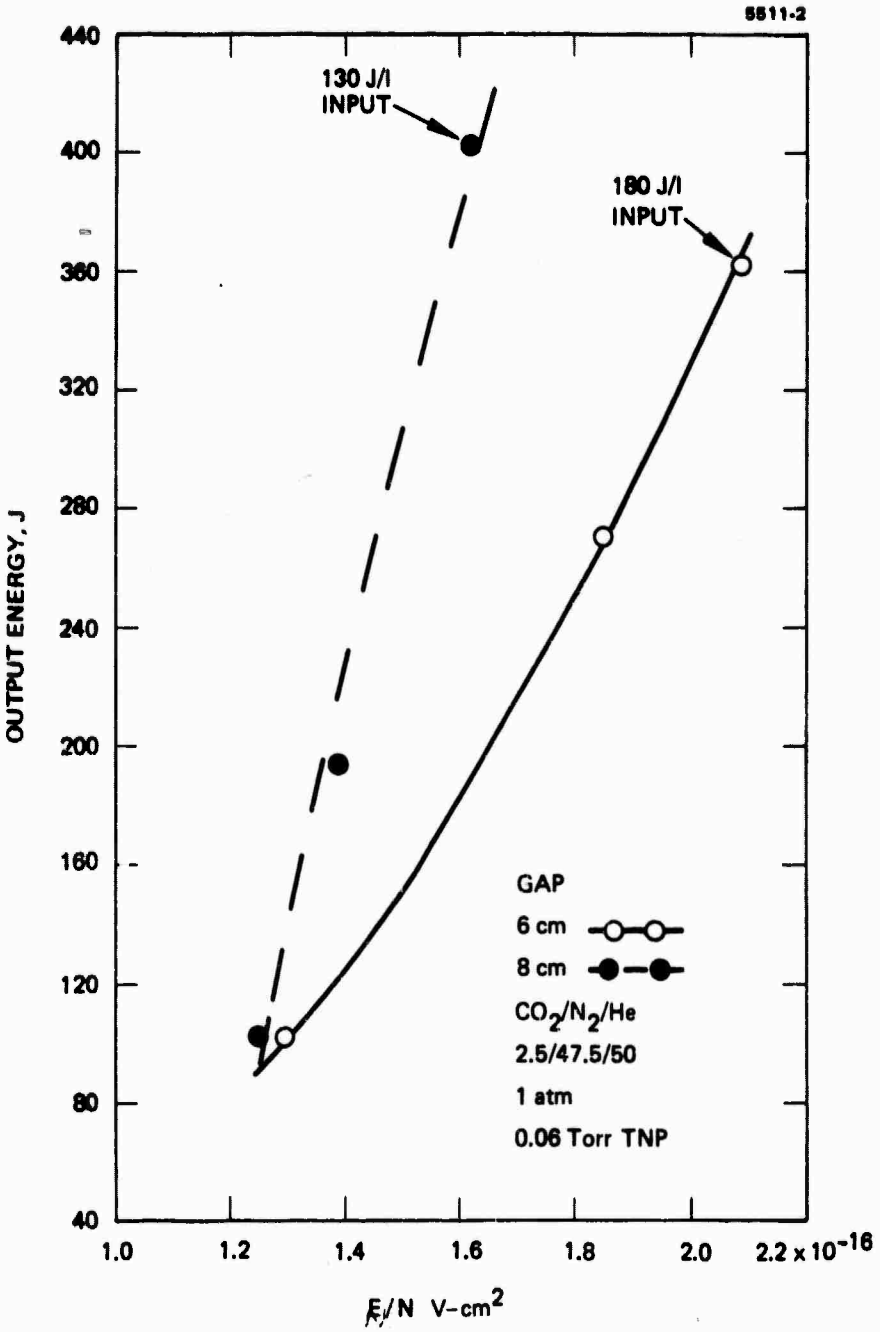

Figure VI-18. Output energy as a function of E/N for unstable resonator.

(180 J/l) was achieved with an output nearly equal to that of the 8 cm case. It is clear that with higher E/N data for the 8 cm case scaling to in excess of 500 J should be achieved. Unfortunately, the higher voltages needed at the larger gap height caused system problems with the arc sensor circuit and resulted in the inability to obtain the data before the contract ended.

To show that the measurements of energy extraction are consistent with the scaling model to be discussed in Section VII calculations for the large scale device were made. These calculations used an input energy density of 180 J/l. Figure VI-19 gives these results where output energy and overall efficiency from the device as a function of gap height is plotted. The experimentally measured values at 6 and 8 cm are also shown. The agreement at 6 cm is within the experimental errors. At 8 cm a greater difference is seen but this is due to the lower input energy result. If scaled by the input energy density ratio virtual agreement is achieved.

Even if we neglect this input energy scaling we see that the overall efficiency for the 8 cm case, which includes the UV sources, is approximately 12%. This value is competitive with e-beam sustained lasers, and substantially better than any UV preionized CO_2 laser systems.

E. Medium Quality Studies

Extensive medium homogeneity measurements were made using double-exposure pulsed holographic interferograms. For this technique, one of the exposures of the hologram (in our case it was always the second one) was taken with no discharge firing, and the other exposure at some specific time during the laser pulse. The double exposed film, after being properly developed, was then illuminated by a cw He-Ne laser and the resulting fringes recorded on polaroid film.

Figure VI-20 shows schematically the experimental arrangement used. The ruby laser was Q-switched by means of a Pockels cell and produced 25 ns output pulses with a peak power of 1 MW. The output beam was made to operate on a single transverse mode by using a 2 mm

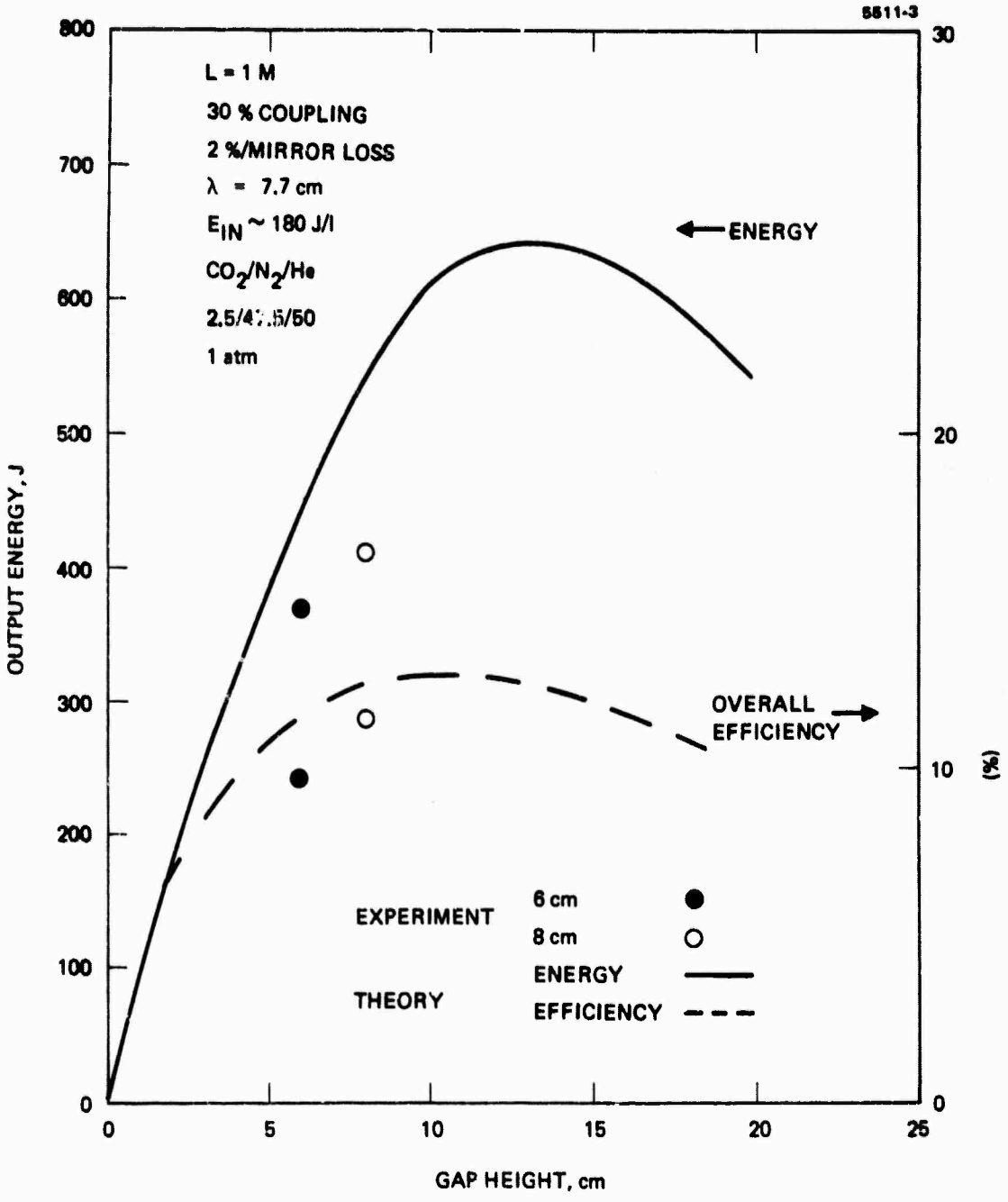

Figure VI-19. Output energy as a function of gap height.

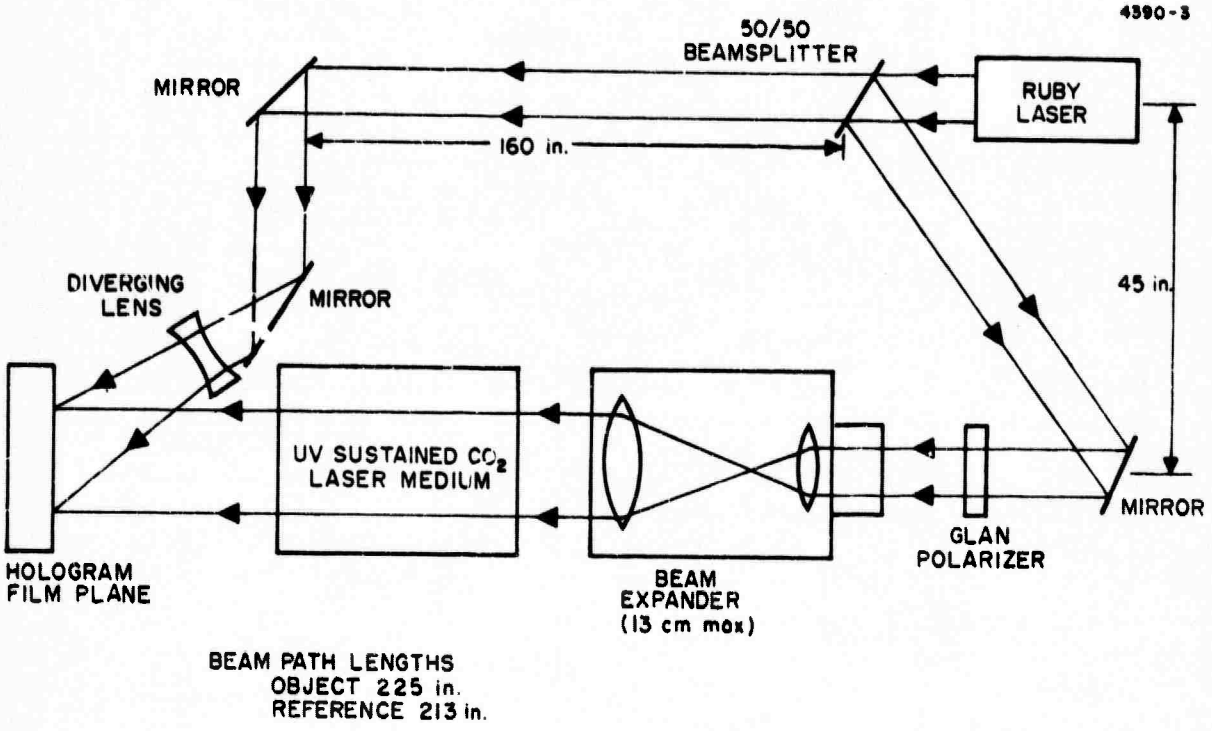

Figure VI-20. Holographic experimental setup.

diameter aperture located inside the optical cavity, and an etalon was used for single longitudinal mode selection.

A reference hologram, made with no discharge firing, but with a 1 atm laser mixture in the UV-sustained laser device is shown in Figure VI-21.

Complete sets of holograms were taken at two transverse locations in the discharge; one in the central 13 cm of the discharge and one in which the discharge edge was included (the beam expander optics limited the field of view to 13 cm). Holograms were taken for various sustainer voltages, UV energy levels, and times after the start of the UV pulse. Typical holograms obtained are shown in Figure VI-22. These holograms represent all of the essential features that occur with discharge firing. They were taken over the central 13 cm of the discharge with a sustainer voltage of 30 kV at 20 and 30 μs after the start of the UV pulse. The cathode is at the bottom in both photographs and the UV sources are located behind each electrode.

From these photographs the acoustic disturbances produced by the upper UV source and by the combined cathode and lower UV source are clearly shown. The distance traveled by the wave fronts in the time frame given in the photographs is consistent with the speed of sound in the mixture ($\sim 4.5 \times 10^4$ cm/sec). It is clear from the holograms that the medium does not suffer inhomogeneities in the region between the UV and cathode waves. This implies a medium quality of better than $\lambda/30$ at 10.6 μm. The fringe shifts obtained in the disturbed region show an initially compressed and heated regime followed by the expansion of this hot gas back through the mesh screens into the region occupied by the UV source. Accounting for all the fringe shifts in traversing the 6 cm gap we find that the medium quality is good to $\lambda/8$ at 10.6 μm. Figure VI-23 gives a hologram taken at the edge of the discharge for conditions identical to Figure VI-22(b). The essential features remain the same with the media quality unaffected by the edge waves. The results from these holograms imply that the far-field beam quality of a high energy UV-sustained laser should be near diffraction limited.

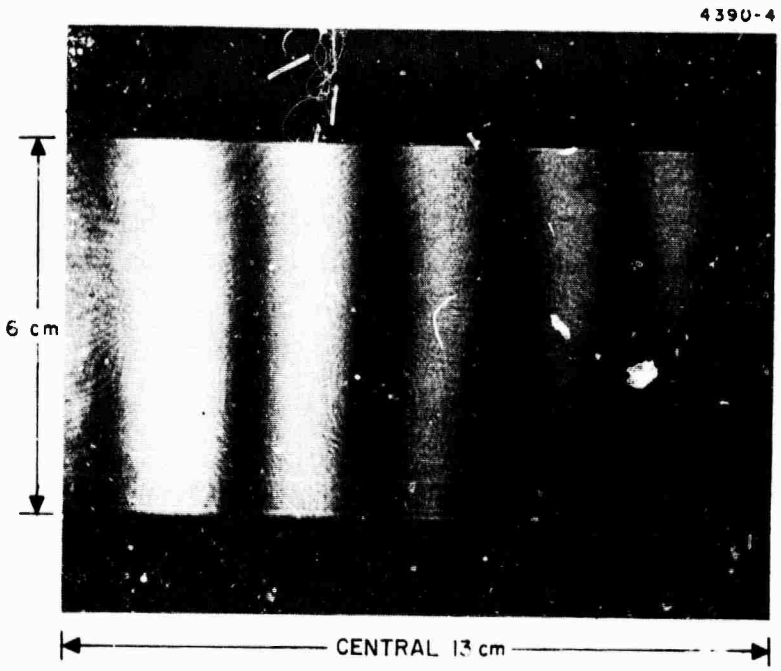

Figure VI-21. Reference hologram.

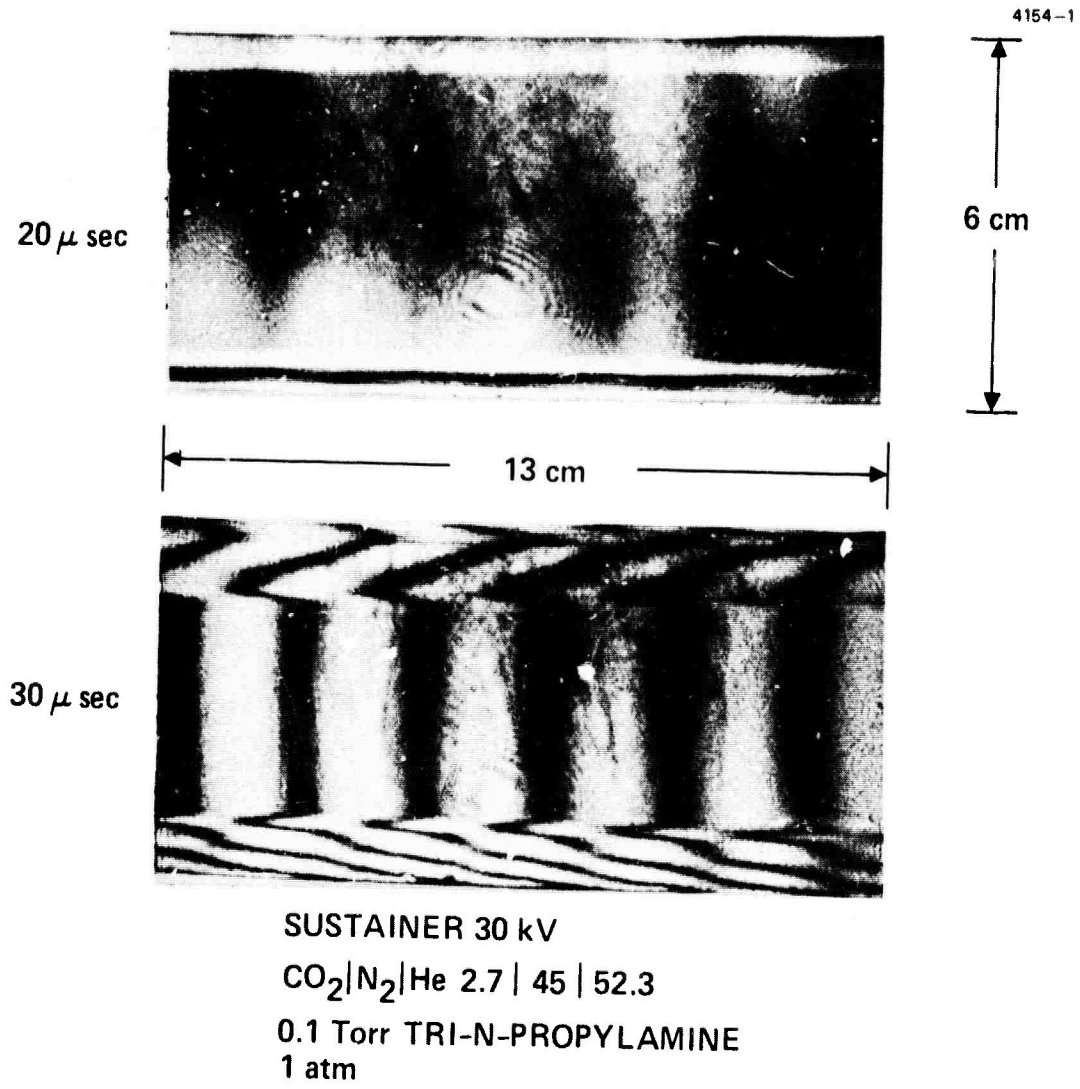

Figure VI-22. Media holograms. (a) 20 μs after start of UV pulse, (b) 30 μs after start of UV pulse.

3830-18

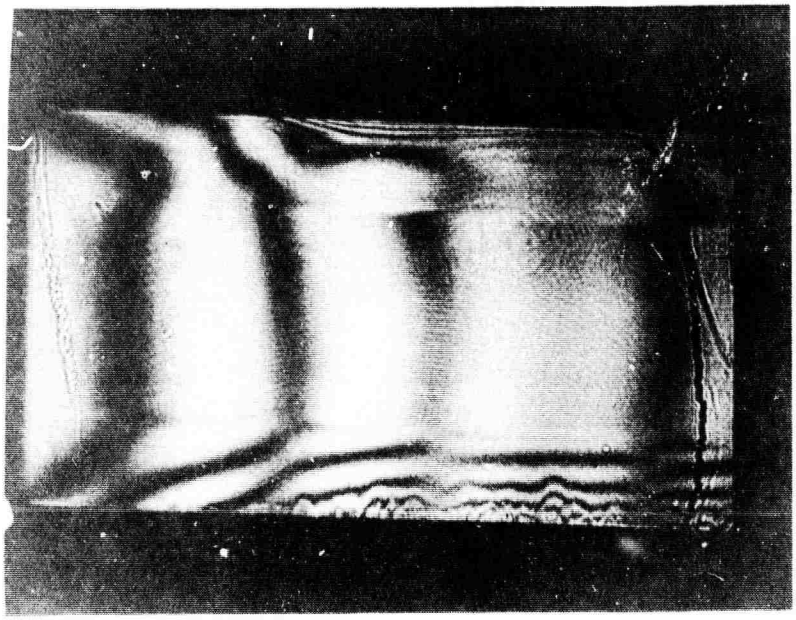

Figure VI-23. Media hologram, edge of discharge at 30 μs.

As an interesting sidelight, an additional hologram taken (Figure VI-24) shows a strong localized energy deposition in the upper UV source region. This implies that one or more of the rows of arcs traveling down the board did not traverse the complete board length (discharge width). Thus the remaining stored energy in those rows of capacitors was discharged in a small region (the circuit being completed through an arc to the mesh screen at the local ground potential). The energy deposition in the laser mixture was essentially unaffected by this but a post arc did occur. That is, about 1 ms after the pulse an arc occurred (the sustainer voltage is applied dc to the electrodes). It is possible that the post arc may have been triggered by this localized high electron density region in the discharge. While such an arc does not degrade the performance of the laser (it occurs after the pulse is over) it discharges the large (50 kJ) sustainer bank into the screen causing permanent damage requiring screen replacement.

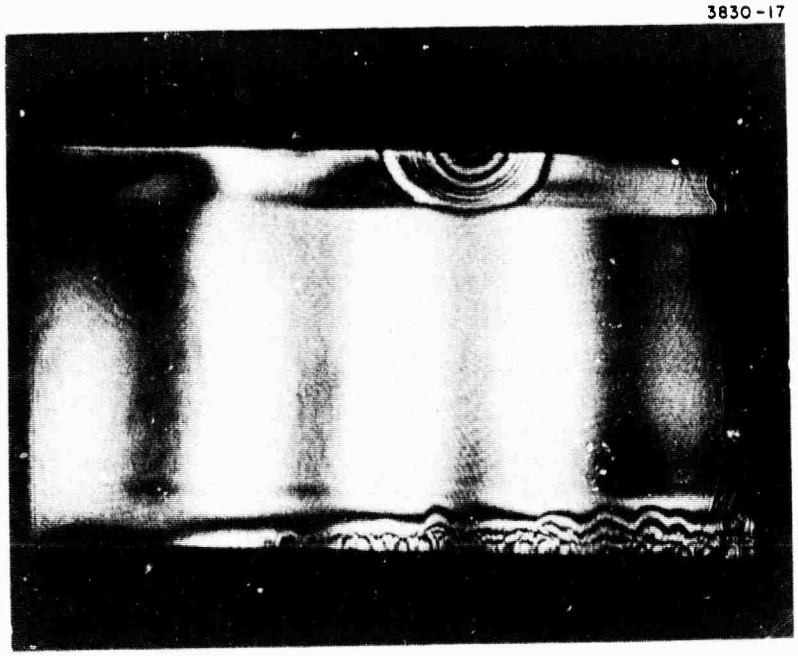

Figure VI-24. Media hologram, center of discharge at 20 μs.

VII. ULTRAVIOLET SUSTAINED LASER SCALABILITY

The purpose of this section is to present scaling relations for a UV-sustained CO_2 laser. These relations are determined from a scaling model that incorporates the important optical, electrical, and laser processes. Based on these relations the conceptual design of a high power UV-sustained laser is presented.

The primary conclusions of the model fall into two categories based upon efficiency and brightness of UV sources. First, using present UV sources scalability to gap heights of about 8 cm appear possible with extraction energy densities of ~50 J/l. To scale to larger gap heights requires improvements in the UV source. For example, a factor of two increase in brightness will allow scalability to greater than 20 cm with >50 J/l energy density at ~20% overall efficiency.

A. Scaling Model

For a nonavalanche discharge, the magnitude and spatial variation of the electron density is determined primarily by the source function. In the present case, the source function is the UV radiant intensity in the 1200 to 1700 Å region produced by a large number of arc discharges located behind each sustainer electrode (see Figure VII-1 for geometry). Because of the geometry and the finite absorption of the UV by the medium, the electron density will be a minimum at the center of the electrode gap. It is this spatial variation in electron density that leads to the fundamental scaling limitations of the UV-sustained technique.

To determine the important scaling parameters, a model has been developed. This model is described briefly below (see Appendix A for a description of the equations used).

The source function is first calculated as a function of gap height and UV absorption length. The source function in this case is a more realistic 2-D array source similar to that employed in the large scale device experiments. The electron density is then calculated

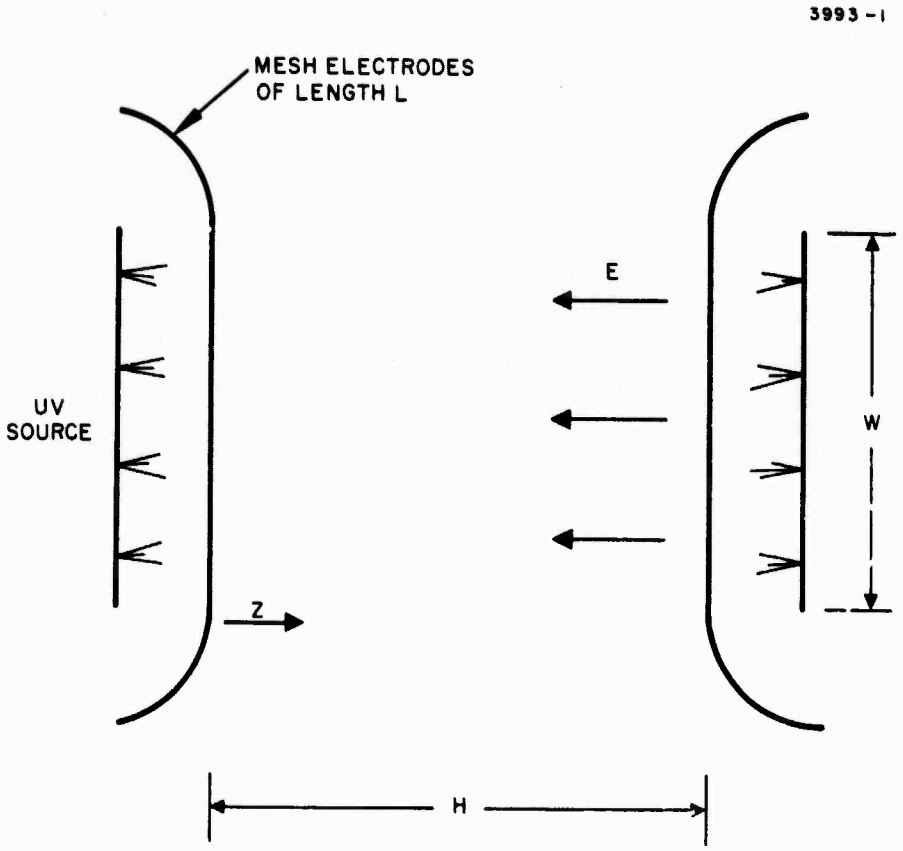

Figure VII-1. Model geometry.

assuming a recombination dominated plasma. Since the current density across the gap must be a constant, the electric field will vary in inverse proportion to the electron density. This electric field variation is then calculated. including the dependence of recombination on electric field. In principle, this adjustment by the electric field could compensate for the spatial nonuniformity in the electron density and scalability would be unlimited. However, as the electrode gap is increased the electric field in the center, where the electron density is a minimum, will eventually increase to a value at which avalanching begins and ultimately lead to an arc. Consequently, the maximum electric field must be limited so that the mean electric field across the gap will permit arc-free operation. The limiting electric field has been determined from experiments on the large scale device (Section VI) ($E_{max} \approx 5.5$ kV/cm-atm) and incorporated into the model. This limitation results in both a lowering of the current density and applied field as the gap spacing is increased. Figure VII-2 shows the calculated UV intensity distribution as a function of position in the gap (z) for two gap heights of 6 and 20 cm and a UV mean-free path of 7.7 cm. (The UV source is located 2 cm behind each electrode.) The 7.7 cm mean-free path was established by fitting theoretical energy input calculation to the input energy measurements on the large scale device. This procedure is discussed in Appendix A. In Figure VII-3 the resulting electric field and current density variation is given as a function of gap height. Since the input energy is a product of the electric field and current density, the input loading is reduced as the gap height is increased. This leads to decreased optical output and efficiency. While this limitation will always exist, it will be shown in the next section that by improving the UV source function, scaling can be extended to dimensions compatible with high energy requirements.

1. Scaling Calculations

The fundamental result of the physical processes discussed above is that the input energy loading will decrease as the gap height is increased. This result is shown in Figure VII-4. (Refer to

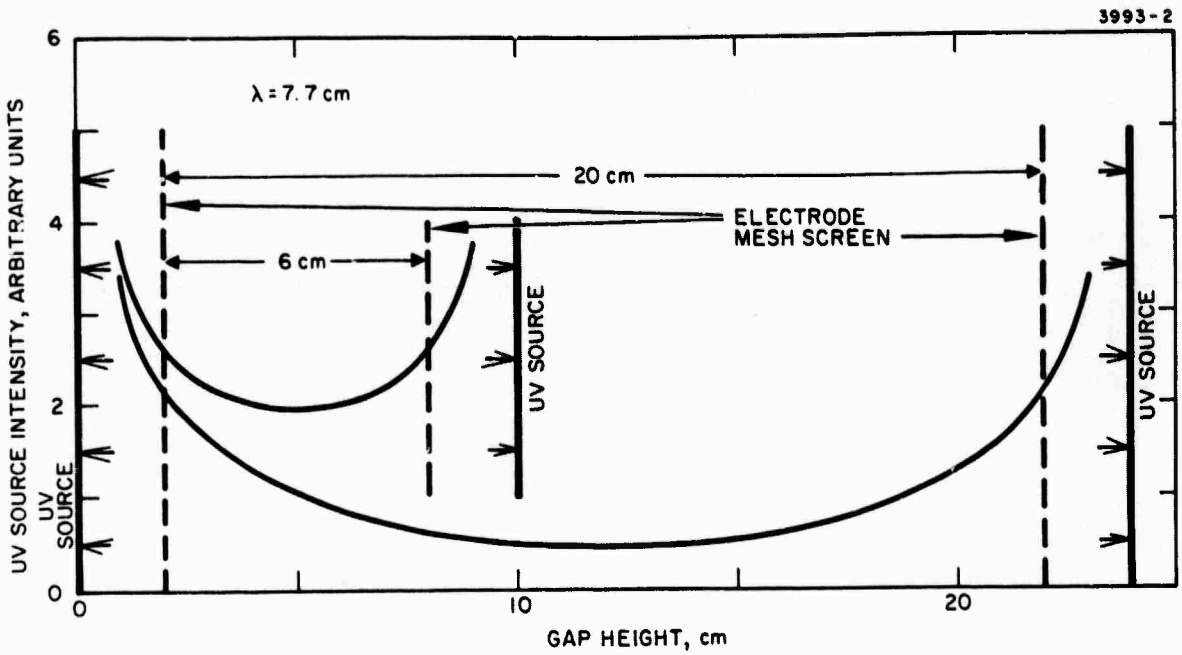

Figure VII-2. Ultraviolet intensity as a function of position (z).

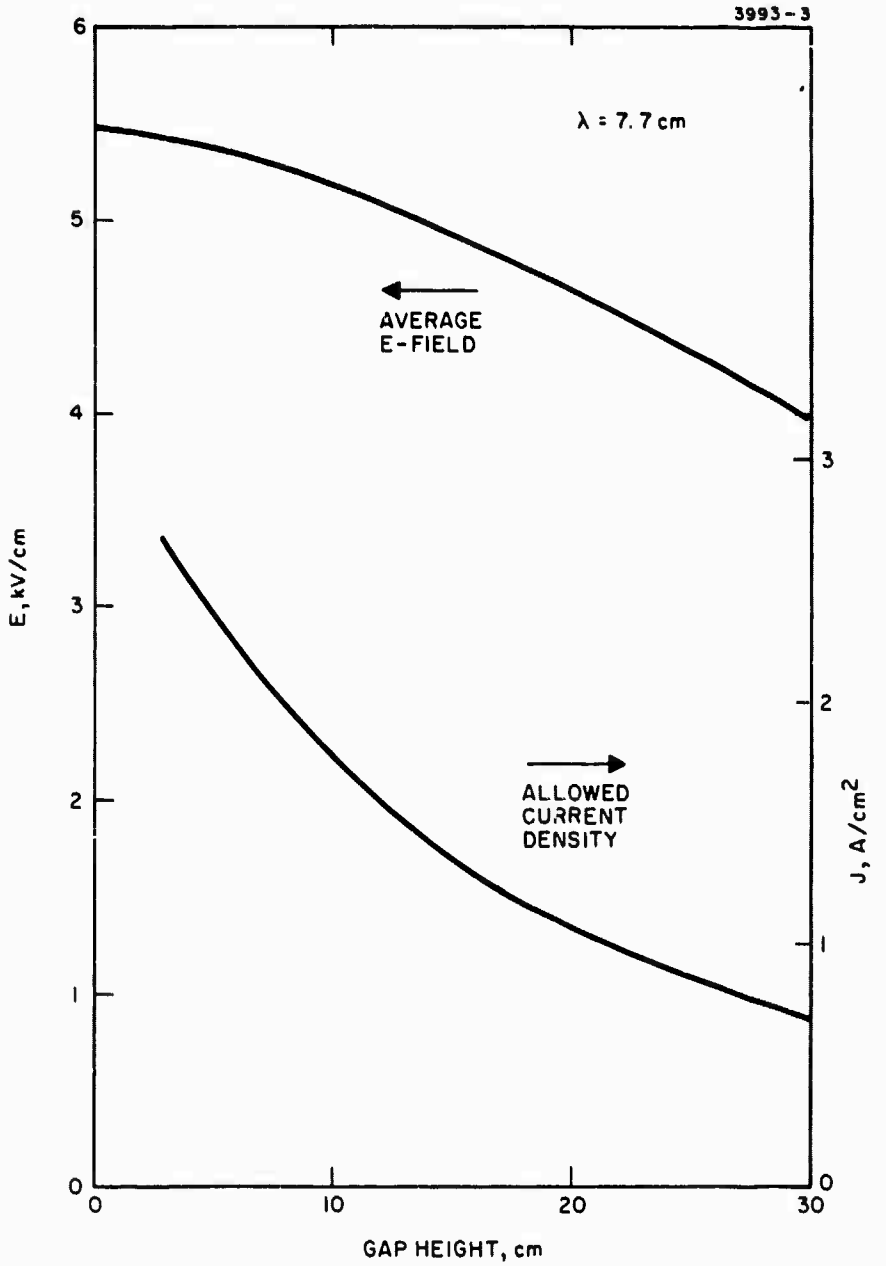

Figure VII-3. Electric field and current density as a function of gap height.

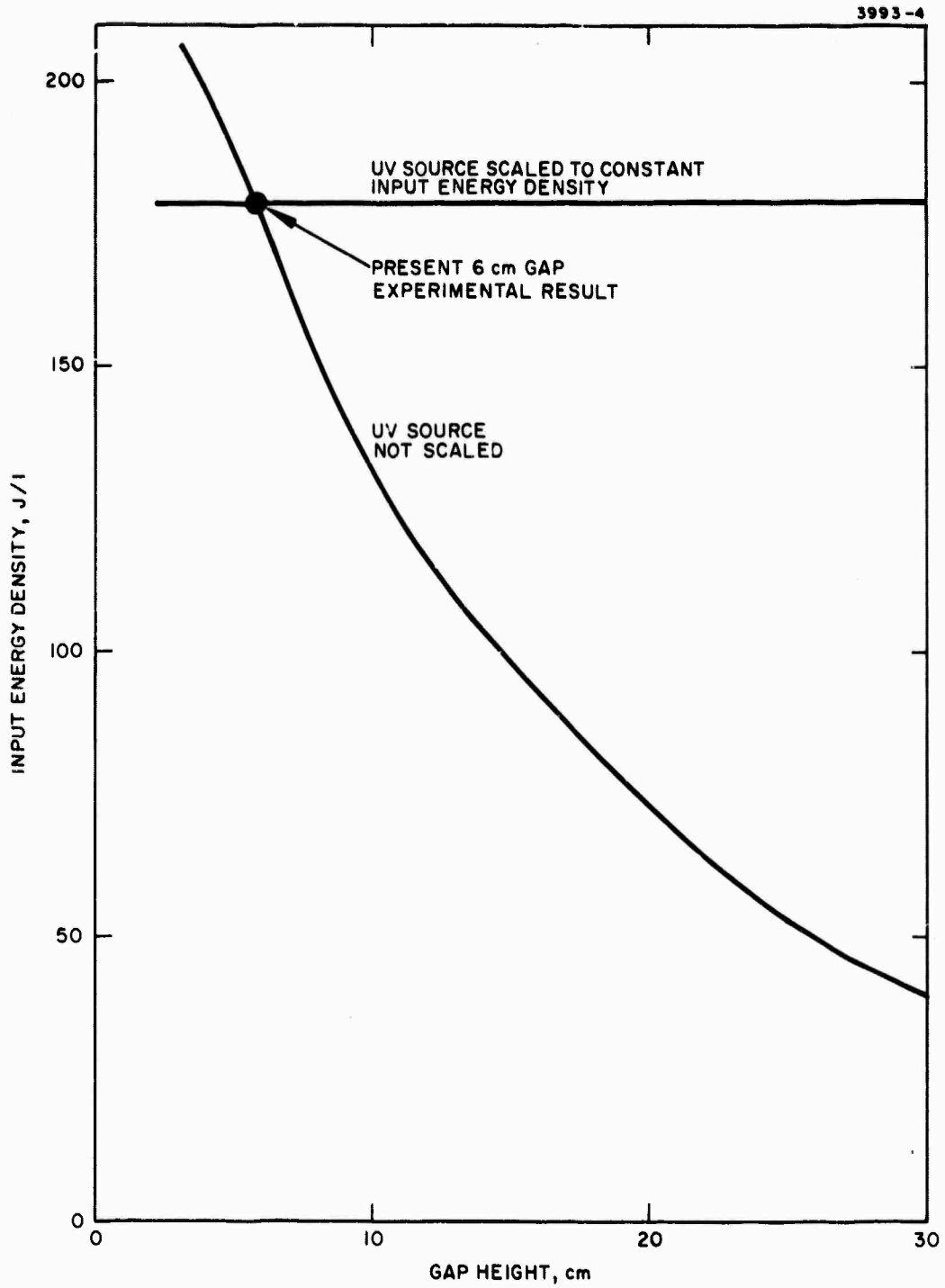

Figure VII-4. Input energy density as a function of gap height.

curve titled – "UV Source Not Scaled"). The input energy density scale shown is normalized to the measured input energy density from the large scale device (Section VI) experiments (measurements made with a gap height H of 6 cm). This normalization is necessary because the absolute magnitude of the UV intensity, in the photoionization wavelength range, is a quantity not amenable to calculation or direct measurement, and represents an adjustable parameter in the model. More explicitly, write the useful UV energy (that which contributes to photoionization) as a product of two efficiencies as follows

$$E_{\substack{\text{useful} \\ \text{UV}}} = \epsilon_{el} \cdot \epsilon_{UV} \cdot E_{stored}$$

where ϵ_{el} is the conversion efficiency of stored electrical to total radiated energy, ϵ_{UV} is the fraction of total radiated energy that is effective in photoionizing the seed gas, and E_{stored} is the electrical energy stored in the capacitors. The efficiency ϵ_{el} can be measured but ϵ_{UV} is more difficult to determine. This quantity is adjusted when normalizing the scaling model results to the large scale device experiments. For the calculations shown in Figure VII-4, the UV source intensity is that derived from the 6-cm gap height data and is fixed at this value for all gap height calculations presented. The calculated laser output energy density (averaged over the discharge volume) as a function of gap height is shown in Figure VII-5 (see curve labeled "UV source not scaled"). This output energy was calculated using the HRL CO_2 kinetic code with the electron-vibrational pumping rates obtained from the HRL electron Boltzmann equation code. The vertical scale is in units of kilojoules per centimeter of discharge width. These results were obtained for the particular length of 5 m, a value that is optimum for the UV-sustained laser (to be discussed later). We see from this curve that the output energy peaks at a gap height of about 10 cm. This gap height represents the scaling limit for the present UV source.

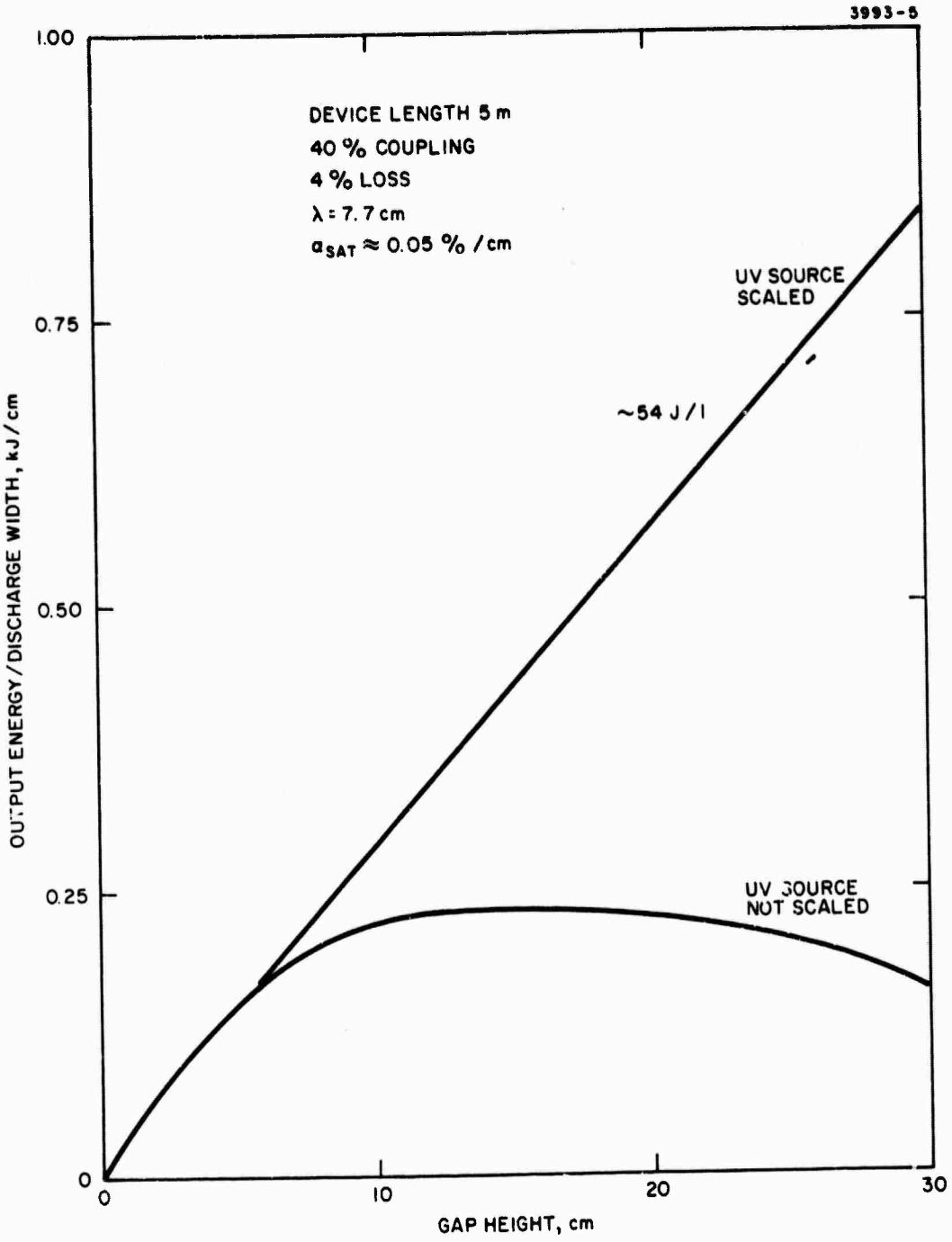

Figure VII-5. Output energy as a function of gap height.

Competitive laser energy and efficiency for electrode gaps greater than 10 cm can only be achieved by increasing the UV source intensity. The exact increase required can be calculated from our scaling model by adjusting the source intensity to obtain some fixed performance goal (i. e., output joules/liter, input joules/liter, or efficiency). Figure VII-6 is the result of such a calculation in which the UV source intensity has been adjusted at each gap height to produce a constant electrical input energy of 180 J/l (see Figure VII-4). The vertical scale shows the UV source intensity required relative to that obtained with the present large scale device source.

Assuming that the UV source can be scaled in the manner shown in Figure VII-6, we can repeat the earlier calculation of expected output energy versus gap height. This result is shown in Figure VII-5 by the curve labeled UV source scaled. The predicted output energy no longer reaches a maximum but continues to increase with gap height at a constant energy density of ~54 J/l (this is not surprising since the input energy density is being held constant).

The remainder of this section will consider the impact of the UV source improvements on laser performance, particularly on the overall electrical efficiency of the laser.

Qualitatively, it is obvious that improving the source efficiency will increase the overall laser efficiency, while increasing the source input energy will decrease the efficiency or at best leave it unchanged. To put this on a more quantitative basis, calculations of laser efficiency have been made for a hypothetical 5 m long device assuming 40% output coupling and an internal loss of 2% per mirror. The results are presented in Figure VII-7. The upper curve labeled "limiting laser efficiency" represents the efficiency that would be achieved if the UV source required no energy. This efficiency is somewhat higher than is predicted for conventional CO_2-N_2 laser due to the very low CO_2 concentration. The lower curve shows what happens when the UV source input energy is included in the efficiency calculation.

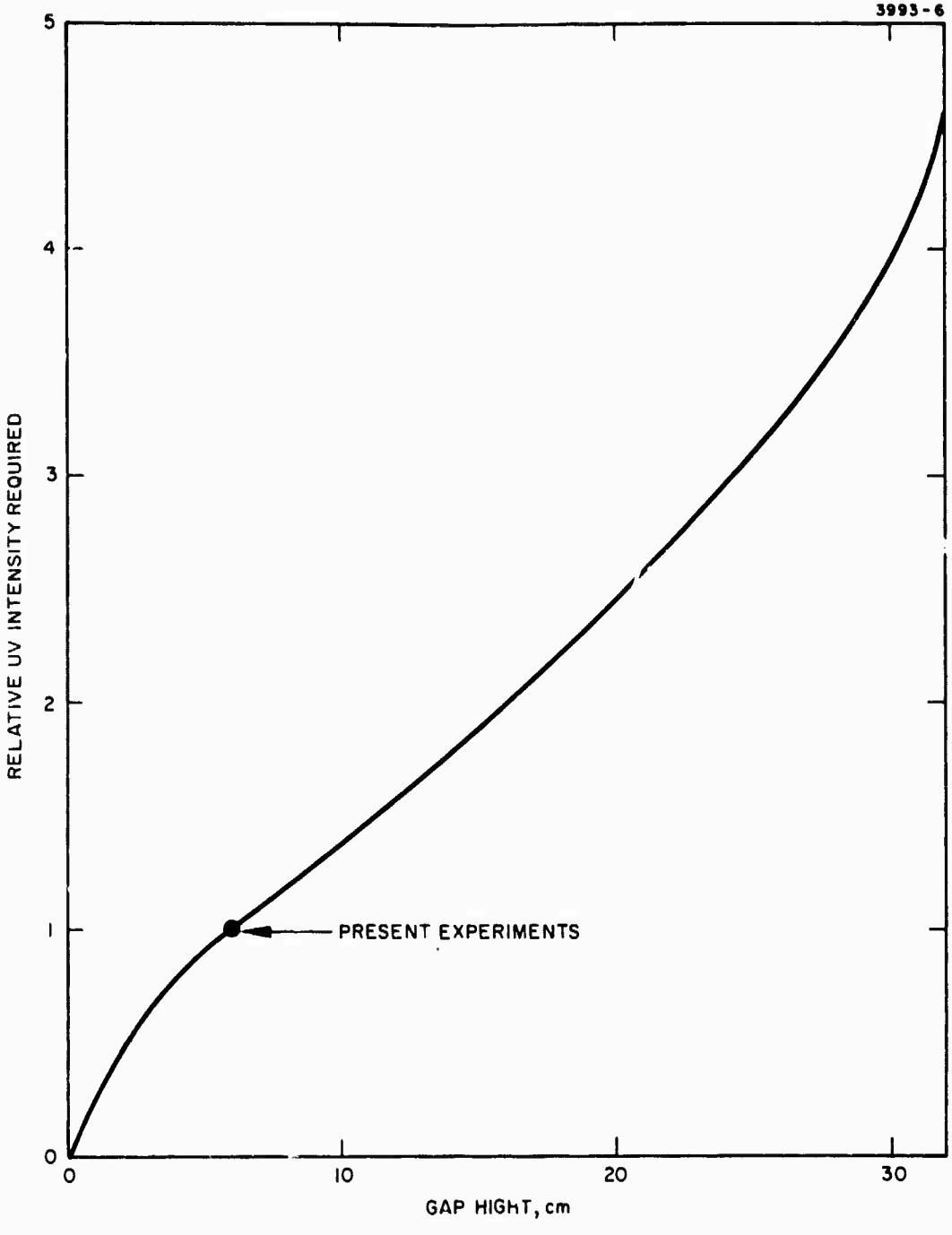

Figure VII-6. Relative UV intensity required as a function of gap height.

Competitive laser energy and efficiency for electrode gaps greater than 10 cm can only be achieved by increasing the UV source intensity. The exact increase required can be calculated from our scaling model by adjusting the source intensity to obtain some fixed performance goal (i.e., output joules/liter, input joules/liter, or efficiency). Figure VII-6 is the result of such a calculation in which the UV source intensity has been adjusted at each gap height to produce a constant electrical input energy of 180 J/l (see Figure VII-4). The vertical scale shows the UV source intensity required relative to that obtained with the present large scale device source.

Assuming that the UV source can be scaled in the manner shown in Figure VII-6, we can repeat the earlier calculation of expected output energy versus gap height. This result is shown in Figure VII-5 by the curve labeled UV source scaled. The predicted output energy no longer reaches a maximum but continues to increase with gap height at a constant energy density of ~54 J/l (this is not surprising since the input energy density is being held constant).

The remainder of this section will consider the impact of the UV source improvements on laser performance, particularly on the overall electrical efficiency of the laser.

Qualitatively, it is obvious that improving the source efficiency will increase the overall laser efficiency, while increasing the source input energy will decrease the efficiency or at best leave it unchanged. To put this on a more quantitative basis, calculations of laser efficiency have been made for a hypothetical 5 m long device assuming 40% output coupling and an internal loss of 2% per mirror. The results are presented in Figure VII-7. The upper curve labeled "limiting laser efficiency" represents the efficiency that would be achieved if the UV source required no energy. This efficiency is somewhat higher than is predicted for conventional CO_2-N_2 laser due to the very low CO_2 concentration. The lower curve shows what happens when the UV source input energy is included in the efficiency calculation.

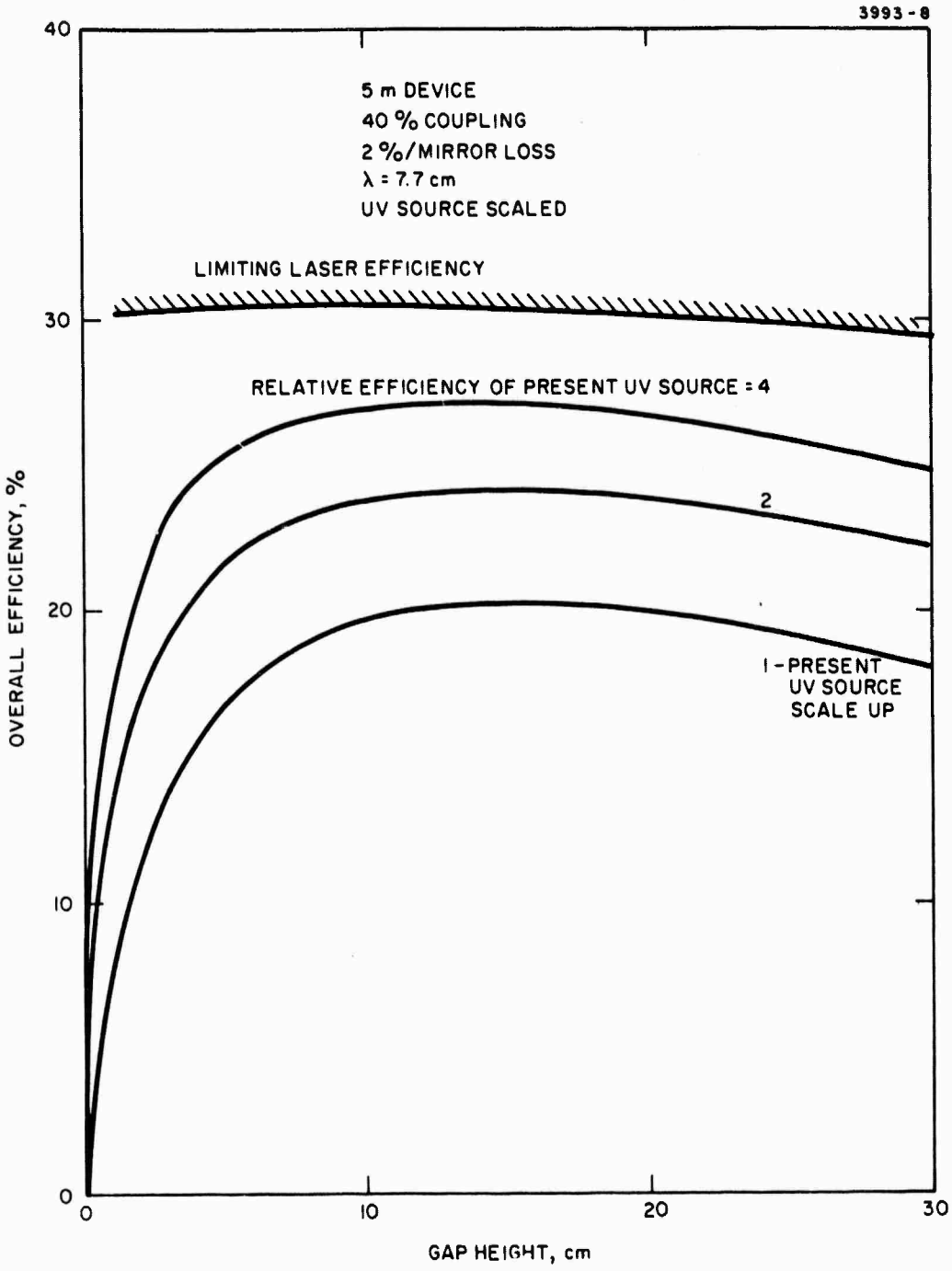

Figure VII-7. Overall efficiency as a function of gap height.

Each curve gives the calculated overall laser efficiency for a fixed UV source efficiency and with the source strength scaled with gap height as shown in Figure VII-6. As expected, the efficiency decreases at large gap heights, but not rapidly. In fact, the efficiency is almost constant out to 20 cm gap height. In this interval, the increased source energy required is offset by the increased energy output. Only for gap heights >25 cm does the exponentially increasing source input begin to dominate the linearly increasing laser output and cause the efficiency to decrease.

The curve labeled "1" shows the efficiency predicted for a source with the conversion efficiency of the present LSD source. The curve labeled "2" assumes the same source energy input increase given by Figure VII-6 and a two-fold increase in the electrical to UV conversion efficiency. Curve "4" is a four-fold increase. As expected, increasing the conversion efficiency causes a direct increase in the laser efficiency. With a UV source of the present type operating at 2.4 times the LSD input energy, a laser with a 20 cm high x 500 cm long cavity can be operated at 20% overall efficiency. At the same UV source input energy and a two times increase in conversion efficiency, the overall laser efficiency increased to ~24%.

2. Summary of Scaling Results

Based on the above calculations, the following general points can be made:

a. To maintain a reasonable device efficiency, the gap height should lie in the range $6 < H < 20$ cm.

b. It is feasible to achieve efficiencies of up to 20%.

c. A specific energy of 55 J/l is possible for large scale devices.

However, these results depend on having a UV source with performance superior to that presently demonstrated.

B. Implications for Scaled UV Sustained Laser

Assuming successful development of improved UV sources, we can establish, based on the above results, guidelines for the construction of a scaled UV-sustained laser.

To begin, an optimum length dimension must be determined. For the UV-sustained laser with its inherent low gain (~ 0.8%/cm), scaling in the length direction is important for fully saturating the medium. This can be seen in Figure VII-8, where output energy density as a function of output coupling for various lengths and losses is given. Choosing a 4% loss (2%/mirror) as representative of average laser mirrors, scaling from 1 m to 5 m increases the specific energy from 44 to 54 J/l at optimum output coupling. In addition, if operation with high output couplings is desired (for good mode discrimination), the 5 m output drops to only 50 J/l at 70% coupling. Clearly, lengths greater than 5 m would be even better, but we have taken 5 m as a limit based on considerations of overall system size and stability. We conclude from these arguments that

- The length should be as great as possible and at least 5 m
- The optimum output coupling is 40 to 50% but can be as high as 70 to 80% with a small sacrifice in specific energy
- Output energies of 50 J/l can be achieved.

The minimum electrode gap separation (H) and resulting efficiencies have been established previously and we find that

- For optimum efficiencies, H should be greater than 6 cm
- The overall efficiency is 20 to 24%.

To estimate the maximum gap separation we make an estimate of a factor of two expected improvement in UV source performance. Further increases in UV intensity are of marginal utility since gaps greater

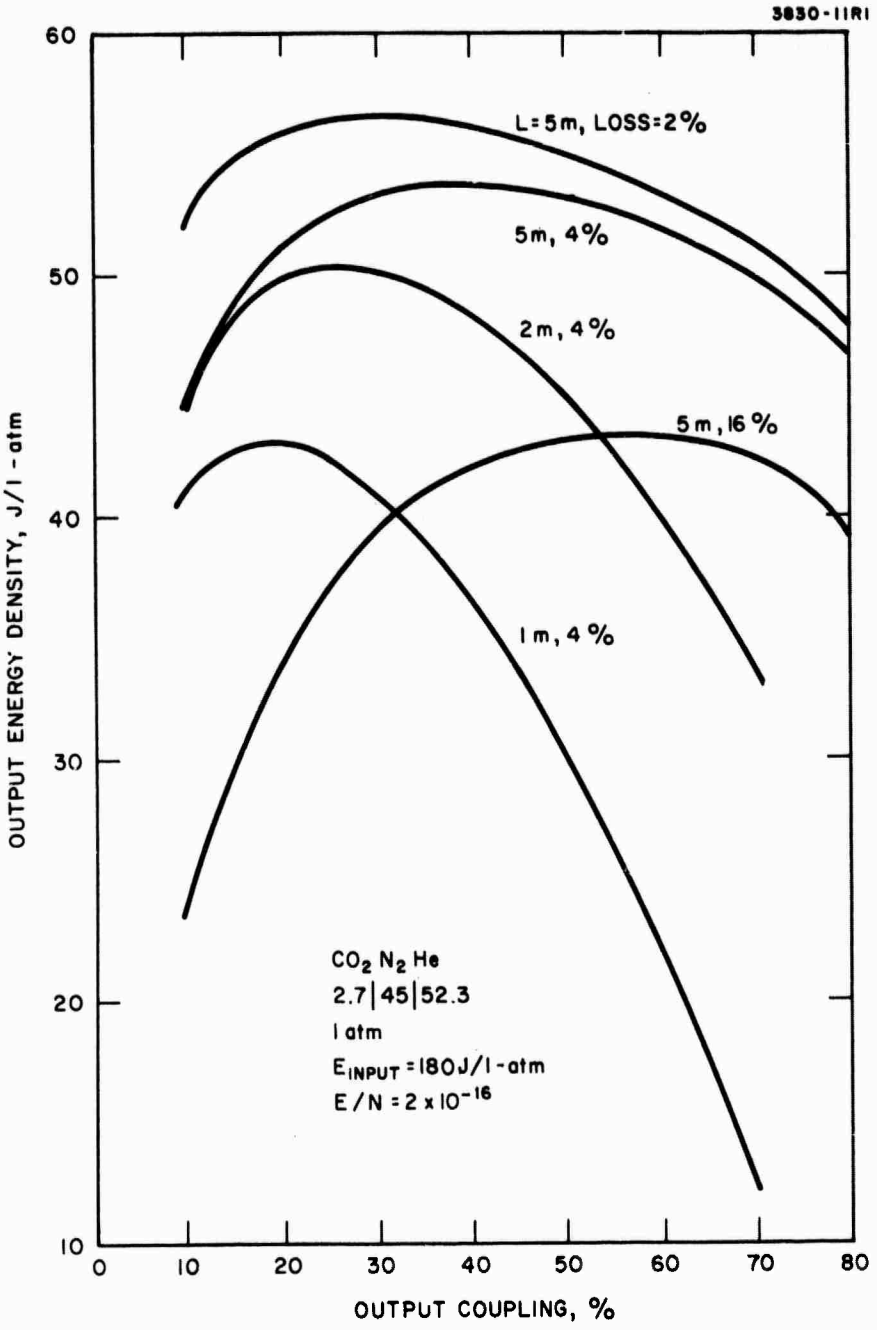

Figure VII-8. Output energy density as a function of output coupling.

than 20 to 25 cm require undesirably high sustainer voltages. Based on these considerations the height H should be

$$H \approx 20 \text{ cm} \quad .$$

In the width (W) direction, the UV source scaling sets no limit in contrast to the situation with e-beam ionization where annular geometries are required. The width W is not limited by UV source considerations. However, for a single pass oscillator device, in order to maintain efficient operation of an unstable resonator used to extract the laser output, the W/H ratio should not be excessive. A reasonable limit is probably W/H = 3.

VIII. PRELIMINARY ULTRAVIOLET SOURCE STUDIES

Based on the conclusions of the scaling model presented in Section VII an improvement in the performance of the UV source must be achieved if multi-kilojoule UV-sustained lasers are to be achieved. In this section we discuss some preliminary studies directed toward an understanding of the factors that control UV source performance and some initial experiments attempting to achieve improved performance.

A. Electron Density

The objective of the improved performance of the UV source is to achieve higher electron densities in the main discharge region. To obtain higher electron densities requires that the useful UV radiation energy, i.e., the energy delivered by the UV source in the wavelength range which produces photoionization of the seed gas, be increased. This wavelength range has been determined from previous experiments to be 1200 to 1700 Å. The useful UV energy can be written as

$$E_{UV} = \epsilon_{UV} \cdot \epsilon_{el} \cdot E_{stored} \quad .$$

There are three avenues by which the useful UV energy can be increased. We will discuss some of the approaches attempted below. It is important to understand that improvements in the UV source do not result in a change in the spatial distribution of the radiative intensity. This is, of course, fixed by the mean free path. They affect only the efficiency of generation of the radiation or the absolute level of the radiation throughout the spatial extent.

1. Electrical Efficiency, ϵ_{el}

The efficiency, ϵ_{el}, which represents the conversion efficiency of total stored energy to total radiated energy, is basically determined by circuit parameters, e.g., by inductance and resistance in the wires and elements employed.

Because the UV arcs employed have a low characteristic impedance, the driving circuit must be of low impedance for maximum power transfer.

2. Ultraviolet Radiation Efficiency, ϵ_{UV}

This efficiency represents the conversion of total radiated power (into all wavelengths) to radiation in the 1200 to 1700 Å bandwidth useful for photoionization. Assuming the source arcs radiate as black bodies then in the range 1200 to 1700 Å, the maximum efficiency possible is 25%. This occurs for a black body temperature of 20,000°K and a total radiative flux of 700 kW/cm^2.

This efficiency is essentially a reflection of the wavelength match between the emitting gas of the UV source and the photoionization cross section of the seed gas.

3. Stored Energy

This quantity indicates what amount of energy must be stored in the capacitor discharge circuits to give a certain electron density. It also indicates what density of arcs is needed.

B. Ultraviolet Source Circuit Discussion

The UV source configuration of a series of copper chips is essentially a low voltage, high current arc where the arc cascades the complete length of the chips. The UV source arcs may be represented to a first approximation by a constant voltage battery. The arcs are arranged in series to obtain a better voltage match to the pulser circuitry. The operating voltage of each arc is typically $V_{UV}^1 \sim 100$ V

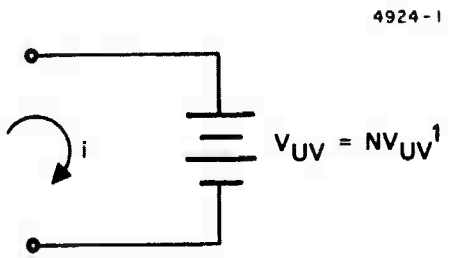

Thus in the large scale device, where the number of chips (or arcs) for each row is $N \sim 20$, we have the voltage of the battery of about $V_{UV} = 20\ V_{UV}^{1} = 2$ kV. The main design problem is matching this low battery voltage to the large voltage (approximately 20 kV) required to break the gaps down and cause the arc cascade to start. This can be seen from a simple analysis of the circuit of one row of arcs.

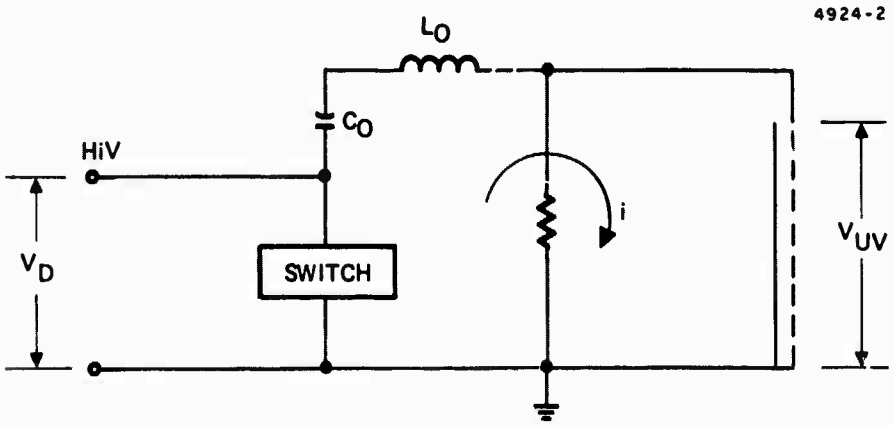

The expression for the current is

$$i = \omega_o C_o (V_o - V_{UV}) \sin \omega_o t \qquad (1)$$

where

$\omega_o = 1/\sqrt{L_o C_o}$

V_o = charging voltage

V_{UV} = voltage across UV row

and the charge on the capacitor C_o is given by

$$q_o = V_{UV}\ C_o + C_o (V_o - V_{UV}) \cos \omega_o t \quad . \qquad (2)$$

At the end of the first half-cycle the current has fallen to zero. This is the period over which you would like to deliver the stored energy to the arc boards. The optimum situation for delivering all the stored energy (e.g., $q_o = 0$ at some time) is when $V_o = 2\,V_{UV}$. That is, if $V_o = 2\,V_{UV}$, the final charge on the capacitor is zero and all the stored energy is delivered to the discharge.

Unfortunately, V_o in the present case is about 20 kV which, of course, is much larger than $2\,V_{UV} = 2(2\text{ kV}) \sim 4$ kV. Thus a voltage mismatch occurs, charge is still left on the capacitor at the end of the pulse, and the circuit "rings." If the resistance of the arc discharge were higher, V_{UV} would be larger and a better match would result. It is known empirically that the resistivity, ρ, of an arc discharge varies inversely proportional to the square root of the field strength

$$\rho \propto \sqrt{\frac{L}{V_{UV}^1}} \quad ,$$

where L is the gap separation of the arc electrodes and V_{UV}^1 is the voltage across the arc. It is also known that the radius r of the arc is proportional to the fourth root of the energy deposition per unit length,

$$r \propto \left(\frac{E}{L}\right)^{1/4}$$

where E is the total energy discharged. Thus the total arc resistance

$$R = \frac{\rho L}{\pi r^2} \propto L^2 \quad .$$

The arc resistance varies directly with the length of the arc (squared). Thus we see that to increase R we would like as long an arc as possible.

Now the energy deposited into the arc discharge can be found by multiplying eq. (1) by V_{UV} and integrating over the time interval (of one half sine wave). We find that

$$E_{arc} = 2 C_o (V_o - V_{UV}) V_{UV}$$

and that E_{arc} is maximum when $V_o = 2 V_{UV}$. The efficiency ϵ_{el} is then given by the ratio of E_{arc} to $E_{stored} = 1/2 (C_o V_c^2)$

$$\epsilon_{el} = 4 \frac{V_{UV}}{V_o} \left(1 - \frac{V_{UV}}{V_o}\right) .$$

For our situation

$$V_{UV} \sim 2 \text{ kV} \quad ; \quad V_o \sim 20 \text{ kV} ,$$

therefore,

$$\epsilon_{el} \cong 30\% .$$

The energy delivered into the arc, E_{arc}, has been measured and was found to be ~25% of the stored energy, in agreement with this simple analysis.

To summarize the results of these expressions we see that to increase the energy delivered to the arc we want (1) to increase the operating voltage of the arc V_{UV}, (2) to increase the resistance of the arc by increasing the arc length, and (3) to lower the charge voltage V_o.

All of these effects give a better voltage match between V_o and V_{UV}. In addition to maximizing ϵ_{el}, we also want E_{stored} as large as necessary to give the electron densities needed. To see how this varies with the circuit parameters we examine the current that flows through the circuit. For the present time we assume that V_{UV} is a constant

across the arcs; hence the light output will vary with the current. The maximum current given from eq. (1) is

$$i_{max} = \sqrt{\frac{C_o}{L_o}} (V_o - V_{UV}) \quad .$$

Since V_{UV} is $\ll V_o$

$$i_{max} \approx V_o \sqrt{\frac{C_o}{L_o}}$$

Thus we see that to maximize the current you want to decrease the inductance and increase the capacitance and the charge voltage. Note that i only varies as the square root of C_o but varies linearly with V_o.

C. Experimental Results

Experiments confined to examining what effects changes in C_o and L_o have upon the electron density production have been made. The medium-scale device (2.5 x 15 x 50 cm^3) has been used for all the measurements. The capacitor size was doubled and the electron density achieved increased as expected. It is important to note that the electron density varies as

$$n_e \propto \sqrt{E_{UV}}$$

$$n_e \propto \left(\frac{C_o}{L_o}\right)^{1/4}$$

Therefore, doubling the capacitor size produced only about a 15% increase in n_e. (Larger size capacitors were not studied because of the prohibitive costs involved.)

Next, the circuit inductance was decreased. This was accomplished by using coaxial cables to feed the capacitor energy to each row together with making all connections from a low inductance copper sheet. It was found that the improvement in electron density production was again small. The basic result can be summarized by noting that although an increase in the peak electron density occurred, the loss rate (controlled by electron recombination) also increased. Hence the total energy into the gas discharge which is the integral of the current pulse remains about the same as in the higher inductance case. There is the benefit that the overall efficiency is slightly higher.

D. Spectral Match Considerations

The remaining factor to consider is the efficiency of matching the UV source spectra to the seed gas photoionization cross section. In experiments described in Section III, it was found that removing the CO_2 from the source region and replacing it with N_2 resulted in a two-fold increase in electron density production. Upon examination of the spectral characteristics of N_2 it was found that many lines appear in 1200 to 1700 Å window useful for photoionization of tri-n-propylamine. Based on these considerations a N_2 purge system was constructed and tested on the small scale device ($2.5 \times 15 \times 50 cm^3$). This system consisted of several feed lines with small holes drilled in them. These feed lines were located directly above the arc board and below the mesh screen electrode. Just before the arc board is fired, a valve is actuated that blows N_2 across the boards and purges the region of CO_2. (The use of a window was not compatible with the device.)

Preliminary results with this system gave about a 15 to 20% increase in input energy density. It is believed that higher increases did not result because of possible alterations in gas composition. In particular the TNP concentration may have been reduced due to dilution with N_2 or by convection out of the region. It is clear that a window is required between the regions but the limited results do indicate the trend toward increased performance as expected.

REFERENCES

1. R. C. Lind and J. Y. Wada, "Investigation of Ultraviolet Photoionization Sustained Discharge for Gas Lasers," First Semiannual Technical Report, Contract N00014-73-C-0287, Hughes Research Laboratories, Malibu, California (1973).

2. R. C. Lind, W. M. Clark, and J. Y. Wada, "Investigation of Ultraviolet Photoionization Sustained Discharge for Gas Lasers," Second Semiannual Technical Report, Contract N00014-73-C-0287, Hughes Research Laboratories, Malibu, California, March 1974.

3. R. C. Lind, "Investigation of Ultraviolet Photoionization Sustained Discharge for Gas Lasers," Third Semiannual Technical Report, Contract N00014-73-C-0287, Hughes Research Laboratories, Malibu, California, August 1974.

4. R. C. Lind, "Investigation of Ultraviolet Photoionization Sustained Discharge for Gas Lasers," Fourth Semiannual Technical Report, January 1975.

5. R. C. Lind, "Investigation of Ultraviolet Photoionization Sustained Discharge for Gas Lasers," Fifth Semiannual Technical Report, January 1975.

6. R. C. Lind, "Investigation of Ultraviolet Photoionization Sustained Discharge for Gas Lasers," Sixth Semiannual Technical Report, March 1976.

APPENDIX A
SCALING MODEL

This appendix contains the basic equations employed in the scaling model discussed in Section VII.

To begin, the radiative intensity from the UV source configuration is determined. This flux distribution is calculated by the following expressions (see Figure A-1 for definition of coordinate system). For each arc,

$$B_{nm}(x, y) = \begin{cases} B_{nm} \dfrac{\text{watts}}{\text{cm}^2 \text{ - ster}} & x_n \le X \le x_n + \Delta \\ 0 & y_m \le y \le y_m + a \end{cases}$$

the intensity is then given by

$$I_{nm}(x_o, y_o, z_o) = \int_{x_n}^{x_n+\Delta} \int_{y_m}^{y_m+a} B_{nm} \frac{z_o}{r^3} e^{-\alpha r} \, dxdy \quad ,$$

which can be approximated as (for sources located at $z = 0$ and $z = H$)

$$I_{nm} = K\left(\frac{z_o e^{-R_o/\lambda}}{R_o^3} + \frac{(H - z_o)\, e^{-R_H/\lambda}}{R_H^3}\right) \qquad (1)$$

where

$$R_o^2 = (x_n - x_o)^2 + (y_m - y_o)^2 + z_o^2$$

$$R_H^2 = (x_n - x_o)^2 + (y_m - y_o)^2 + (z_o - H)^2$$

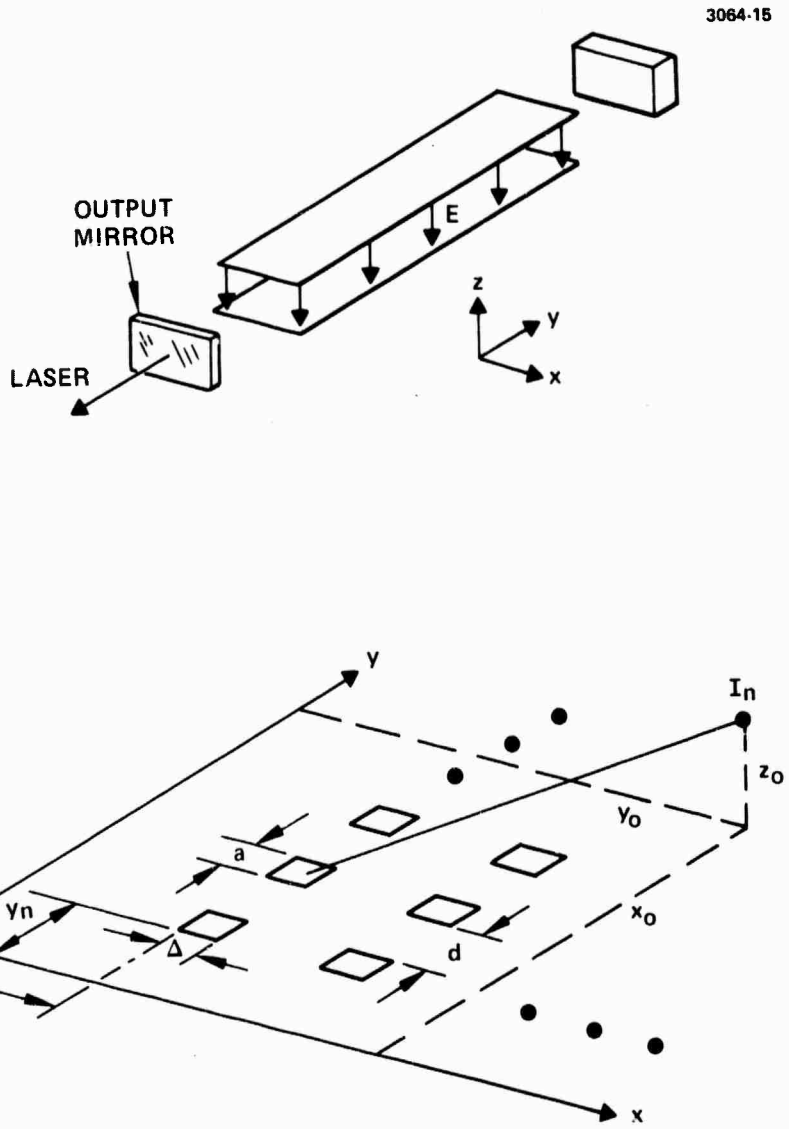

Figure A-1. Photon flux calculation coordinate system.

H is the electrode separation

λ is the mean free path of the radiation

K is a constant relating to the magnitude of the intensity from the emitters $= \Delta \cdot a/4\, B_{nm}$,

I is the specific intensity.

This expression is written for an nxm two-dimensional array of UV emitters. It must then be summed over all emitters to give

$$I = \sum_{n,m} I_{nm} \quad . \tag{2}$$

The source function appropriate to the case of single-step photoionization of an added seed gas is given by

$$S = \frac{1}{\lambda} \frac{1}{h\nu_{UV}} \tag{3}$$

where S is the source function, $h\nu_{UV}$ is the energy of the emitter UV radiation.

The electron density is determined from a solution of the electron rate equation, and for a recombination dominated plasma at steady state we have

$$n_e = \sqrt{\frac{S}{\alpha(E)}} \tag{4}$$

where $\alpha(E)$ is the field dependent recombination coefficient. We take the field dependence to be

$$\alpha = KE^{-p} \tag{5}$$

and assume that $P \simeq 2$. When these expressions are combined we obtain an equation relating n_e, E and I

$$n_e = f(E, I) \tag{6}$$

From conservation of charge across the gap we must have

$$J = en_e V_d = \text{const} \tag{7}$$

where V_d is the electron drift velocity in the laser mixture and is determined from the electron Boltzmann code to be

$$V_d = a + bE \tag{8}$$

in the operating E range of the UV sustained laser experiments. When this expression is substituted into (7) and then using (6) we have

$$J = g(E, I) = \text{const} \quad . \tag{9}$$

To determine the value of the constant we require that the maximum value of E, which occurs in the center of the discharge, be of such a magnitude that the mean value of E defined as

$$E_{mean} = \frac{1}{H} \int_{gap} Edz \tag{10}$$

is below the avalanche value for arc-free operation. This value of E_{mean} has been determined to have a value of ~5.5 kV/cm from the Large Scale Device experiments (see Section VI). Since the intensity is known in the middle, we can determine the constant in eq. (9). That is, we first assume a value for J, solve eq. (9) for E and then determine E_{mean} from (10). If E_{mean} satisfies the arc-free criteria, we have determined the correct value of the constant J. If not, we iterate until

satisfied. This constant is, of course, the current density. Since the value of I in the center decreases as the gap spacing is made larger (see Figure 9) since E is fixed in the middle, the value of J decreases. This decrease in J is the primary reason for the drop in input energy as discussed in the text.

With the value of J known and E_{mean} calculated, we then determine the input energy from

$$E_{input} = \int_{pulse} E_{mean} \cdot J \cdot dt \quad . \tag{11}$$

The laser output is determined from the CO_2 kinetic code using the input energy value determined above.

Finally, the overall efficiency is calculated from

$$\epsilon = \frac{E_{laser}}{E_{input} + E_{UV}} \quad . \tag{12}$$

As seen from eq. (1) the mean free path of the radiation in the CO_2 laser mixture must be known. For use in the model, it was determined by comparing the model predictions of input energy with experimentally determined values from the Large Scale Device experiments (Section VI). In particular, experiments were run at two different CO_2 concentrations, yielding two values for the input energy. The mean free path was then adjusted in the model until agreement with these two measured values was obtained. Such a procedure yielded a mean free path of 7.7 cm, a value in close agreement with that derived from other considerations (see Section III).